EXPERIMENTAL AND NUMERICAL STUDIES ON THE VISCOELASTIC BEHAVIOR OF LIVING CELLS

ZHOU ENHUA

NATIONAL UNIVERSITY OF SINGAPORE
2006

EXPERIMENTAL AND NUMERICAL STUDIES ON THE VISCOELASTIC BEHAVIOR OF LIVING CELLS

ZHOU ENHUA

(B.Eng., WUHEE & M.Eng., WHU)

A THESIS SUBMITTED
FOR THE DEGREE OF DOCTOR OF PHILOSOPHY
DEPARTMENT OF CIVIL ENGINEERING
NATIONAL UNIVERSITY OF SINGAPORE
2006

Acknowledgements

This thesis involves the collaborative efforts of many people, to which I am grateful. First and foremost, I would like to thank my thesis advisors Prof. QUEK Ser Tong and Associate Prof. LIM Chwee Teck. I appreciate Prof. Quek's relentless effort in helping me to improve scientific thinking and writing as well as his kindness in allowing me ample freedom in pursuing my research interest. Prof. Lim introduced me to the exciting field of bioengineering. I am particularly grateful to his encouragement, inspiration and humor, which make my PhD research full of fun and high spirits.

The experimental work in this thesis could not have been accomplished without the full support from the Nano Biomechanics Lab (Division of Bioengineering) led by Prof. Lim, which provided excellent facilities and financial resources. I would like to thank all the colleagues in the lab: VEDULA S.R.K., LI Ang, FU Hongxia, Gabriel LEE, Eunice TAN, HAIRUL N.B.R., Kelly LOW, ZHANG Jixuan, Gregory LEE, LIU Ying, QIE Lan, CHENG Tien-Ming (National Taiwan University), Ginu UNNIKRISHNAN (Texas A & M University), John MILLS (MIT), TAN Lee Ping, CHONG Ee Jay, LI Qingsen, JIAO Guyue, SHI Hui and NG Sin Yee for stimulating discussions, warm friendship and many other helps. I am grateful to Abel CHAN, Brian LIAU (Johns Hopkins University), Anthony LEE, NG Shi Mei, Ammar HASSANBHAI, Kelvin LIM and YONG Chee Kien for technical assistance in the experiments.

My sincere thank goes to the Department of Civil Engineering for providing a comfortable and vibrant research environment. I thank my colleagues in the department: DUAN Wenhui, TUA Puat Siong, LI Zhijun, MA Yongqian, VU Khac Kien, LUONG Van Hai, PHAM Duc Chuyen, SHAO Zhushan, CHEN Zhuo, SHEN Wei, Kathy YEO, Annie TAN and Mr. SIT Beng Chiat for interesting discussions and valuable support.

I would like to thank Prof. Jeffrey FREDBERG, Dr. Guillaume LENORMAND, Dr. DENG Linhong, and many other future colleagues at Harvard School of Public Health for sharing their knowledge on soft glassy rheology of cells. I am particularly thankful to Prof. Fredberg for sponsoring me to attend a workshop on cell mechanics at Harvard in 2005.

I want to thank my colleagues in Biochemistry Lab, Division of Bioengineering: Prof. Seeram RAMAKRISHNA, YANG Fang, XU Chengyu, HE Wei, Thomas YONG, Karen WANG, Satinderpal KAUR and many others for allowing me to use their facilities and helping me with cell culture and confocal microscopy. I would also like to thank Dr. CHAI Chou (Johns Hopkins Singapore) for helping me with cytoskeleton staining and TAY Bee Ling (Department of Biological Sciences) for helping me with the fabrication of glass micropipettes. I am indebted to Prof. KOH Chan Ghee, Prof. James GOH, Prof. Somsak SWADDIWUDHIPONG, Prof. Dietmar HUTMACHER and many other NUS lecturers for sharing their knowledge and enthusiasm in scientific research with me.

NUS generously provided me with research scholarship, to which I am indeed grateful. I am more than grateful to the unconditional love and persistent support from my parents, my wife and other family members. Thank you!

Table of Contents

Acknowledgements i

Table of Contents iii

Summary viii

List of Tables x

List of Figures xi

List of Symbols xiv

Chapter 1 Introduction 1

1.1 Structure of eukaryotic cells 2

1.2 Viscoelastic properties of cells 4

1.3 Finite element modeling of cell deformation 7

1.4 Objectives and scope of work 8

1.5 Organization 9

Chapter 2 Literature Review on Cell Mechanics 11

2.1 Experimental techniques in cell mechanics 13

2.2 Mechanical models for eukaryotic cells 16

2.2.1 Overview 16

2.2.2 Cortical shell-liquid core models 17

2.2.2.1 Newtonian liquid drop model 17

2.2.2.2 Shear thinning liquid drop model 21

2.2.2.3 Maxwell liquid drop model 25

2.2.3 Spring-dashpot smear models 27

2.2.3.1 Linear elastic solid model 28

2.2.3.2 Standard linear solid model 31

2.2.3.3 Standard linear solid-dashpot model 33

2.2.4 Power-law rheology model 35

2.2.5 Summary 40

Chapter 3 Experimental Setup and Procedures 42

3.1 Micropipette aspiration technique 42

3.1.1 Fabrication of glass micropipettes and chambers 42

3.1.2 Temperature control 43

3.1.3 Setup of the hydrostatic loading system 43

3.1.4 Testing procedures 45

3.1.5 Accuracy in the measurement of pressure and time 46

3.2 Cell culture 47

3.3 Drug treatments 47

3.4 Staining of actin filaments 48

Chapter 4 Micropipette Aspiration of Fibroblasts – Ramp Tests and Effects of Pipette Size 49

4.1 Introduction 49

4.2 Experimental results 51

4.2.1 Effect of pipette size on cell deformation 52

4.2.2 Apparent deformability measured with large pipettes 56

4.2.3 Stress-free projection length measured with large pipettes 59

4.2.4 Ramp-test results for 1/120 cmH_2O/s 61

4.3 Discussion 64

4.3.1 Blebbing and nonlinear deformation preferentially occur with smaller pipettes 64

4.3.2 Larger pipettes are more suitable for probing smeared mechanical properties of cells 65

4.3.3 Rate dependence of measured deformability 67

4.3.4 Calculation of deformed projection length 67

4.3.5 On approximate applicability of linear viscoelasticity to cells.........68

Chapter 5 Micropipette Aspiration of Fibroblasts – Creep Tests and Power-law Behavior...71

5.1 Introduction...71

5.2 Experimental results...73

5.2.1 Creep behavior of untreated fibroblasts...73

5.2.1.1 Interpretation and modeling of creep function.............................74

5.2.1.2 Statistical distribution of the power-law parameters.....................77

5.2.1.3 Effect of pipette size on creep function 79

5.2.2 Effect of drug treatments 80

5.3 Discussion..84

5.3.1 Power-law behavior of creep function and its dependence on pipette edge effect...84

5.3.2 Compatibility between creep tests and ramp tests...........................86

5.3.3 Mechanical properties of fibroblasts – a comparison with others' work 88

5.3.4 A general trend for power-law rheology of cells.............................90

5.3.5 High reproducibility and low variability of the current measurement..92

5.3.6 Effect of actin cytoskeleton disruption 95

5.3.7 Effect of microtubule cytoskeleton disruption.................................97

5.4 Conclusions..99

Chapter 6 Finite Element Simulation of Micropipette Aspiration Based on Power-law Rheology..101

6.1 Introduction...101

6.2 Material constitutive relations...103

6.2.1 Neo-Hookean elasticity..103

6.2.2 Power-law rheology approximated by Prony series expansion 104

6.3 Finite element model based on power-law rheology 106

6.3.1 Basic assumptions 106

6.3.2 Geometric description of micropipette aspiration..........................106

6.3.3 Boundary and loading conditions 107

6.3.4 Finite element mesh 108

6.4 Results..108

6.4.1 Elastic deformation 109

6.4.2 Creep deformation 112

6.4.2.1 Prony-series approximation of power-law rheology and simple shear test 112

6.4.2.2 Power-law behavior of simulated creep deformation 114

6.4.2.3 Effect of α on B_{FE} and β_{FE} 117

6.4.2.4 Effect of pipette geometry on B_{FE} and β_{FE}................................119

6.4.2.5 Comparison between experiments and simulation......................121

6.4.3 Ramp deformation 124

6.4.3.1 Effect of loading rate and α on C_{FE} 125

6.4.3.2 Effect of pipette geometry on C_{FE}...127

6.4.3.3 Comparison between experiments and simulation......................128

6.5 Discussion..130

6.5.1 Interpretation of $G(1)$ and α using FE simulation results...............131

6.5.2 Departure from linear viscoelasticity and correspondence principle 132

6.5.3 Comparison with others' work on FE simulation of micropipette aspiration using other rheological models 134

6.5.4 Potential application in studying mechanotransduction 135

Chapter 7 Conclusions and Future Work 138

7.1 Conclusions 138

7.2 Future work 140

References 142

Appendix A Reported Mechanical Properties of Cells Based on Three Models 155

Appendix B Linear Viscoelasticity 160

B.1 Linear viscoelasticity based on fractional derivatives 160

B.2 Derivation of the complex modulus 161

B.3 Derivation of power-law rheology model from the fractional derivative viscoelasticity 162

B.4 Power-law rheology model and the correlation between complex modulus, creep function and relaxation modulus 163

B.5 Elastic-viscoelastic correspondence principle 165

B.6 Derivation of ramp-test response in micropipette aspiration from power-law creep function 166

B.7 Power-law dependence of apparent deformability on loading rate in ramp tests 167

Appendix C Prony Series Approximation of Power-law Rheology 169

Appendix D Curriculum Vitae 170

Summary

Mechanical forces and deformation are among the key factors influencing the physiology of cells. How cells move, deform, and interact, as well as how they sense, generate, and respond to mechanical forces are dependent on their mechanical properties and these properties need to be studied and understood. Micropipette aspiration has been widely used to measure the viscoelasticity of cells in suspension, which has generally led to the development of spring-dashpot models. However, recent experiments performed on attached cells using other techniques strongly supported the power-law rheology model, which may potentially serve as a general model for cell rheology. Yet, this model has not been experimentally proven for suspended cells.

In this dissertation, the micropipette aspiration technique was used to investigate the rheology of suspended NIH 3T3 fibroblasts with the aim of investigating whether the power-law rheology model also applies to cells in suspension. In the *ramp tests*, cells were subjected to linearly increasing suction pressure using pipettes of different diameters. The pipette diameter was found to have a significant effect on cell deformation, where for diameters smaller than ~ 5 μm, nonlinear and inconsistent deformations were observed but for diameters larger than ~ 7 μm, deformation of the cells was found linear and consistent. Therefore, larger pipettes are more applicable than smaller ones for measuring the smeared rheology of NIH 3T3 fibroblasts.

In the *creep tests*, cells were subjected to a step pressure applied using large pipettes. The power-law rheology model was found to accurately fit the creep functions of suspended fibroblasts, providing new support to this model for suspended cells. Effect of cytoskeleton disruption on rheological properties was investigated. Disruption of actin filaments with cytochalasin D caused cells to appear softer but more elastic. In contrast, disruption of microtubules with high dosage of colchicine caused activation and stiffening of cells.

Finite element method is an established and versatile engineering tool, particularly suited for the continuum mechanical analysis of cell deformation. However, a finite element model that incorporates the power-law rheology of cells was not available. Here, a finite element model incorporating the power-law rheology of cells was proposed. The initial-boundary-value problem of micropipette aspiration was solved numerically. Using consistent rheological properties, this model could predict the experimental observations obtained using both creep and ramp tests for suspended NIH 3T3 fibroblasts. The finite element simulation revealed departure from the half-space solution as a result of (i) finite cell radius with respect to pipette radius, (ii) large deformation and (iii) slippage. Approximate formulae were proposed based on simulation results, which allow direct interpretation of rheological properties of cells in micropipette aspiration.

It is hoped that the experimental methodology and theoretical model proposed in this thesis will contribute to a more accurate evaluation of the viscoelastic properties of healthy and diseased cells and better understanding of the biological response of cells to mechanical stimuli.

List of Tables

4.1 Measured mechanical properties of cells with ramp tests 67

6.1 B_{FE} for $\alpha = 0 \sim 0.4$, $e^* = 0.06$ and $R_p^* = 0.25 \sim 0.6$ 120

6.2 Summary of FE simulation results 130

A.1 Reported mechanical properties for Newtonian liquid drop model 155

A.2 Reported mechanical properties for standard linear solid model 156

A.3 Reported mechanical properties for power-law rheology model 157

C.1 Prony-series coefficients for fitting power-law rheology model 169

List of Figures

1.1 The structure of a eukaryotic cell 3

2.1 Experimental techniques for cell mechanics 14

2.2 The first experimental setup of micropipette aspiration....15

2.3 An overview of mechanical models for living cells....16

2.4 Deformation of a cell in micropipette aspiration 18

2.5 The Newtonian liquid drop model 18

2.6 Modeling the micropipette aspiration of neutrophils with CSLC models 20

2.7 The shear thinning liquid drop model 23

2.8 The Maxwell liquid drop model....25

2.9 The homogeneous standard linear solid (SLS) model....32

2.10 The SLS-D model....34

2.11 Modeling oscillatory twisting cytometry of human airway smooth muscle cells 38

3.1 Glass chamber for containing cell sample....42

3.2 Experimental setup for micropipette aspiration 44

3.3 Measurement of pipette diameter and cell deformation in micropipette aspiration....45

4.1 Deformation of cells during ramp tests with micropipette aspiration....53

4.2 Effect of pipette size on ramp-test results 54

4.3 Dependence of measured deformability on pipette size....57

4.4 Fitting ramp-test data with half-space model and elastic FE model 58

4.5 Dependence of measured stress free projection length on pipette diameter 60

4.6 Determination of pipette entrance location 61

4.7 Effect of pipette size on ramp-test results at 1/120 cmH_2O/s 62

4.8 Dependence of measured deformability on pipette size at 1/120 cmH$_2$O/s 63

5.1 Creep deformation of fibroblasts measured by micropipette aspiration 74

5.2 Average creep function of suspended fibroblasts plotted in log-log scale......75

5.3 Fitting average creep function of suspended fibroblasts by three models 76

5.4 Statistical distribution of the power-law rheology (PLR) parameters............78

5.5 Effect of pipette size on the measured creep function....................................80

5.6 Effect of drug treatments on cell deformation during creep experiments.......81

5.7 Power-law behavior of average creep functions after drug treatments...........82

5.8 Effect of drug treatments on power-law coefficients 83

5.9 Fitting the L_p^G-based creep function with PLR and SLS-D models...............86

5.10 Predicting the ramp-test deformation based on the creep-test results 87

5.11 Difference in actin cytoskeleton for attached and suspended fibroblasts 90

5.12 Comparison of the PLR parameters reported with different experimental techniques 91

5.13 Effect of cytoD on the rheological properties and actin cytoskeleton of NIH 3T3 fibroblasts 96

6.1 Schematic of micropipette aspiration of a cell 106

6.2 An axisymmetric finite element (FE) model for a spherical cell 108

6.3 Geometric comparison of the FE model with the half-space model 109

6.4 Effect of pipette radius on elastic force-deformation relationship 110

6.5 Dependence of $C_{FE}^{\alpha=0}$ on R_p^* for elastic FE analysis ($\alpha = 0$)..........................111

6.6 Fitting power-law relaxation modulus with 5-term Prony series expansion...113

6.7 Comparison of FE-computed creep functions at different stress levels with analytical prediction for $\alpha = 0.3$..114

6.8 Evolution of L_p/R_p with time for different power-law exponents (α) 115

6.9 Fitting simulated creep deformation with power-law function 116

6.10 Effect of α on β_{FE} and B_{FE} 118

6.11 Effect of pipette radius on B_{FE} and β_{FE} 120

6.12 Effect of fillet radius on B_{FE} and β_{FE}....................121

6.13 Comparison of deformed cell shapes between simulation and experiments for a creep test at ΔP = 100 Pa....................122

6.14 Comparison between experiments and simulation for creep tests 123

6.15 Typical pressure-deformation relationship in a simulated ramp test 124

6.16 Effect of loading rate on C_{FE} for different α....................126

6.17 Effect of α on C_{FE}, as modulated by the loading rate 127

6.18 Effect of pipette radius and fillet radius on C_{FE}, as modulated by α for $v_{\Delta P}$ = 10/3 Pa/s 128

6.19 Comparison of deformed cell shapes between simulation and experiments for a ramp test with $v_{\Delta P}$ = 10/3 Pa/s....................129

6.20 Comparison of apparent deformability between experiments and simulation for ramp tests at two loading rates: 10/3 Pa/s and 5/6 Pa/s....................129

6.21 Three-level hierarchical approach to investigating mechanotransduction of single cells....................137

B.1 The correlation between complex modulus, creep function and relaxation modulus for the power-law rheology model 165

List of Symbols

A_G	Magnitude of complex modulus at $\omega = 1$ rad/s for the PLR model
A_J	Creep compliance corresponding to $t = 1$ s for the PLR model
b	Power for shear thinning fluid
$\mathbf{B}$	Left Cauchy-Green strain tensor
B, β	Power-law scaling factor and exponent for experimentally measured creep deformation
$B_{H\text{-}S}$, $\beta_{H\text{-}S}$	Power-law scaling factor and exponent for creep deformation, based on the half-space solution
B_{FE}, β_{FE}	Power-law scaling factor and exponent for creep deformation, based on the FE simulation
C_{FE}	Average slope of L_p/R_p against $\Delta P/G(1)$ derived from FE simulation of power-law rheology model
$C_{FE}^{\alpha=0}$	Average slope of L_p/R_p against $\Delta P/G(1)$ derived from FE simulation of elastic model
d	Lateral bead translation in MTC
e	Fillet radius of pipette
e^*	Fillet radius scaled by cell radius
E	Young's modulus
f	Frequency (in Hz)
F	Force of indentation
F_0, A_F	Average force and amplitude of oscillatory AFM indentation
$\mathbf{F}$	Deformation gradient
G	Elastic shear modulus
$G(t)$	Relaxation shear modulus
$G^*(\omega)$	Complex shear modulus

G', G''	Dynamic storage and loss shear moduli
G_0, ω_0	Scaling factors for stiffness and frequency for PLR model
$H(t)$	Heaviside function
$\mathbf{I}$	Unit tensor
I_1	Deviatoric strain invariant
$J(t)$	Creep function
$J_{FE}(t)$	FE-computed creep function
J_0, t_0	Scaling factors for creep compliance and time for PLR model
k	Elastic constant for Maxwell model
k_1, k_2	Elastic constants for SLS and SLS-D models
L_p	Deformed projection length of a cell
L_p^T	Total projection length measured for a cell
L_p^{SF}	Stress-free projection length of a cell measured with ramp tests
L_p^G	Stress-free projection length of a cell estimated from geometry
P_{cr}	Critical suction pressure
R	Radius of the bead in MTC
R_c	Radius of a cell
R_I	Radius of a plane-ended cylindrical indenter
R_p	Inner radius of a pipette
R_p^*	Pipette radius scaled by cell radius
R^2	Pearson product moment correlation coefficient
S	Slope of the ΔP-L_p^T relation measured in a ramp test
t	Time
T	Specific mechanical torque applied per unit bead volume in MTC
T_0	Static cortical tension

U	Neo-Hookean strain energy density function
$\mathbf{u}$	Displacement field tensor
$\mathbf{v}$	Velocity field tensor
$v_{\Delta P}$	Loading rate in a ramp test
$v_{\Delta P}^{*}$	Loading rate for which C_{FE} is independent of β'_{FE}
$\mathbf{x}$, $\mathbf{X}$	Tensors for current and initial configurations in elastic deformation
$\mathbf{x}(t)$	Tensor for the configuration at time t in viscoelastic deformation
α	Exponent of the power-law rheology model
α_{MMTC}	Geometric coefficient for magnetic MTC
α_{OMTC}	Geometric coefficient for optical MTC
β'_{FE}	Magnitude of the average slope of $\log_{10} C_{FE}$ versus $\log_{10} v_{\Delta P}$ at a given α
γ	Engineering shear strain in simple shear
$\dot{\gamma}_c$	Characteristic shear rate for shear thinning fluid
$\dot{\gamma}_m$	Mean shear rate for shear thinning fluid
$\dot{\gamma}_p$	Instantaneous shear rate at a point for shear thinning fluid
$\boldsymbol{\gamma}$	Engineering strain tensor
$\dot{\boldsymbol{\gamma}}$	Strain rate tensor
$\Gamma(\cdot)$	Gamma function
δ	Depth of indentation
δ_0, A_δ	Average depth and amplitude of oscillatory AFM indentation
ε	Difference between L_p^{SF} and L_p^{G}
ΔP	Total suction pressure
ΔP^{*}	Dimensionless suction pressure, $\Delta P/G(1)$
η	Apparent viscosity for shear thinning fluid

η_c	Characteristic viscosity for shear thinning fluid
θ	Inclination angle of a pyramid-shaped indenter
κ	Shape factor for bead geometry in MTC
λ_1, λ_2, λ_3	Principal stretches at x, y and z directions
μ	Shear viscosity for Newtonian fluid or viscous constant for spring-dashpot models
μ_0	Viscous constant for SLS-D model
ν	Poisson's ratio
$\boldsymbol{\sigma}$	Total Cauchy stress tensor
τ	Engineering shear stress in simple shear
$\boldsymbol{\tau}$	Deviatoric part of Cauchy stress tensor
ϕ	Angle of bead rotation in MTC
Φ_P	Geometric constant for the half-space model
ψ	Phase lag in an oscillatory test
ω	Angular frequency (in rad/s)

Chapter 1 Introduction

All living organisms are under the influence of forces. Scientific investigation on the response of biological tissues to mechanical forces has began since as early as in the 17th century, when Galileo Galilei (1564-1642) examined the strength of bones and Robert Hooke (1635-1703) investigated the elasticity of a number of biological materials. It was only in the mid 1960's that modern biomechanics began to evolve with the development of continuum mechanics, computing technologies and systematic testing of biological tissues ranging from hard tissues such as bones to soft tissues such as blood vessels (Fung 1993; Humphrey 2003).

A major thrust of biomechanics research is to promote better understanding of physiology and pathophysiology, as pointed out by Fung (1993). To this end, study on single cells is important because they are the basic units of life (Alberts *et al.* 2002). Cells generate forces to migrate, contract, divide and perform phagocytosis, blood cells are subject to deformation during circulation and neural cells respond to mechanical stimuli in hearing and touch. Also mechanical forces are known to regulate cell shape, migration, gene expression and even apoptosis. Therefore, cell mechanics investigates "how cells move, deform, and interact, as well as how they sense, generate, and respond to mechanical forces" (Zhu *et al.* 2000).

Cell mechanics was first pioneered by the experimental works of Crick and Hughes (1950), who probed the cytoplasm of fibroblasts with magnetic beads, and Mitchison and Swann (1954), who tested sea-urchin eggs with micropipette aspiration. Early attempts before 1980's were comparatively sparse and mainly focused on structurally simple cells, such as sea urchin eggs and red blood cells (RBCs). Thereafter, more systematic investigation were made on cell mechanics, exemplified by the burgeoning of various innovative experimental techniques on different types of cells and the development of a series of important theoretical works and mechanical models (Zhu *et al.* 2000; Kamm 2002; Bao and Suresh 2003; Lim *et al.* 2006).

1.1 Structure of eukaryotic cells

Typical eukaryotic animal cells are made of 70 ~ 85% of water and 10 ~ 20% of proteins, with the rest being lipids, polysaccharides, RNA, DNA and small metabolites (Alberts *et al.* 2002). The major functional units of a cell are compartmentalized into various membrane-enclosed organelles, including the nucleus (Fig. 1.1). These organelles are dispersed in the cytoplasm, which is spanned by a system of protein filaments collectively called the cytoskeleton. The cytoskeleton provides a three-dimensional (3D) scaffold for the spatial organization of the organelles (Pangarkar *et al.* 2005; Dinh *et al.* 2006). There are mainly three types of cytoskeletal filaments: actin filaments, microtubules and intermediate filaments. The actin filaments (also called microfilaments) are two-stranded helical polymers with a diameter of 8 nm, mainly distributed close to the cell cortex. The microtubules, hollow cylinders with a diameter of 25 nm, irradiate from the center of the cell into the cytoplasm. The intermediate filaments are ropelike fibers with a diameter of around 10 nm, found throughout the cytoplasm and also within the nuclear envelop. The various cytoskeletal elements are crosslinked into a network by various accessory proteins. However, the cytoskeleton is not a static structure. It undergoes constant remodeling and is capable of moving and contracting due to the action of motor proteins and the dynamic assembly and disassembly of the cytoskeletal polymers.

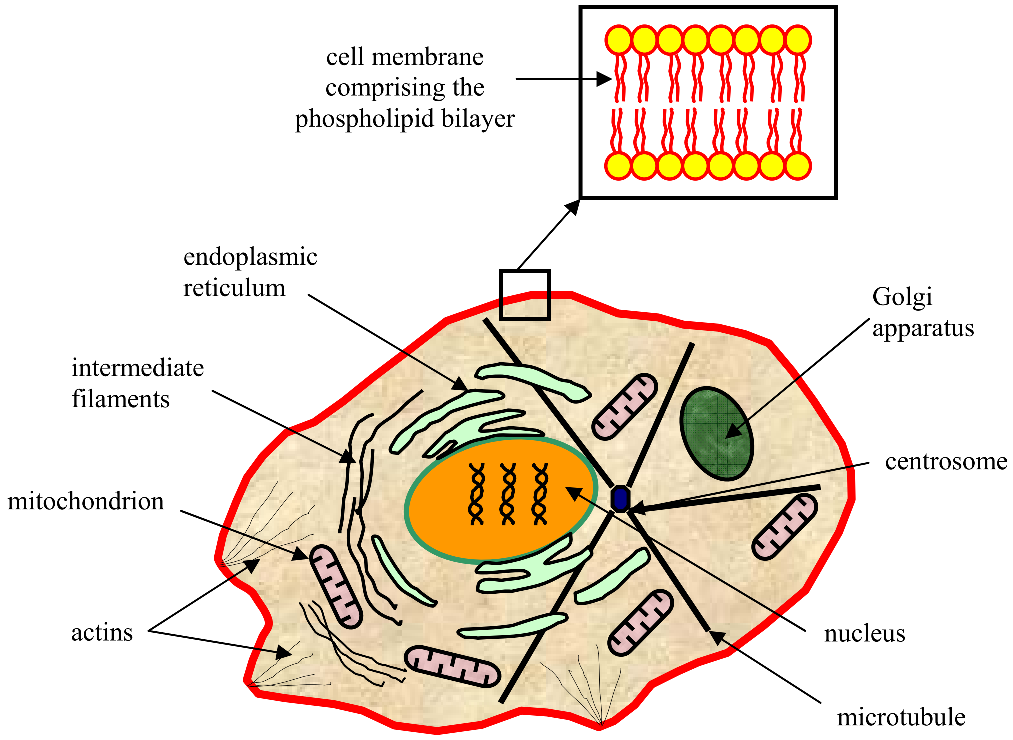
cell membrane
comprising the
phospholipid bilayer
endoplasmic
reticulum
Golgi
apparatus
intermediate
filaments
centrosome
mitochondrion
actins
nucleus
microtubule

Fig. 1.1. The eukaryotic cell is composed of a cell membrane, a cytoplasm (which includes the cytosol, cytoskeleton and various suspended organelles) and a nucleus (which houses the genetic materials) (Lim *et al.* 2006).

The cytoskeleton serves a wide range of functions, one of the most important of which is to provide mechanical strength to the cells. In fact, the mechanical properties of the cells are predominantly determined by the cytoskeleton. This was demonstrated firstly by the fact that cytoskeletal networks reconstituted in vitro can approximately replicate mechanical properties of cells (Janmey *et al.* 1994; Gardel *et al.* 2006) and secondly, by the observation that disrupting the cytoskeletal elements such as actin filaments will reduce the stiffness of cells (Petersen *et al.* 1982; Wakatsuki *et al.* 2001). Therefore, cytoskeletal abnormalities in the molecular level may be manifested as changes in the mechanical properties of cells (Elson 1988). Probing the mechanical properties of the cells might contribute to better understanding, diagnosis, and treatment of relevant diseases such as cancer, malaria, arthritis and some skin diseases (Nash *et al.* 1989; Ward *et al.* 1991; Fuchs and Cleveland 1998; Trickey *et al.* 2000; Guck *et al.* 2005; Suresh *et al.* 2005).

1.2 Viscoelastic properties of cells

Quantification of the mechanical properties of cells has been intensely pursued in the past few decades (Bao and Suresh 2003; Lim *et al.* 2006). Based on the concept of continuum mechanics, the properties of cells are widely expressed in mechanical terms such as the Young's modulus, viscosity, storage modulus and loss modulus. Various experimental techniques and mechanical models have been developed to measure these properties and will be reviewed in detail in Chapter 2. Unlike some common engineering materials, the cells are neither fluid-like or solid-like, but exhibit strong viscoelastic behavior. If a constant force is imposed, the cells will creep whereas if a constant deformation is applied, the resisting force of the cells will relax over time. Therefore, the mechanical properties of cells can only be accurately described when the viscoelasticity of cells is taken into account properly.

The cytoskeleton is a highly conserved structure (Mitchison 1995) and is qualitatively similar across different nucleated animal cell types (Alberts *et al.* 2002). Thus, one would expect the cytoskeleton of different nucleated animal cell types to have qualitatively similar passive viscoelastic behaviors. Furthermore, the generic behavior of the cytoskeleton deformation should not depend on the measuring techniques. Therefore, it would be desirable to have a general viscoelastic model which can cover as many cell types as possible and as many experimental techniques as possible. Such a general model will potentially identify common features of cytoskeleton deformation and reveal the physical state of the cytoskeleton (e.g. as soft glass or as gel) (Fabry *et al.* 2001a; Bursac *et al.* 2005). In addition, having a general model will standardize the interpretation of mechanical properties and will allow the comparison of mechanical moduli across different cell types and across different experimental techniques.

Micropipette aspiration had been widely used to perform creep tests on neutrophils, chondrocytes, endothelial cells and fibroblasts in suspension (Schmid-Schonbein *et al.* 1981; Evans and Kukan 1984; Evans and Yeung 1989; Sato *et al.* 1990; Ward *et al.* 1991; Tsai *et al.* 1993; Sato *et al.* 1996; Thoumine and Ott 1997a; Jones *et al.* 1999b; Thoumine *et al.* 1999; Trickey *et al.* 2000; Trickey *et al.* 2004). Most of the spring-dashpot viscoelastic models were proposed in the context of this technique and had widely been used for many other types of experiments (Lim *et al.* 2006). However, several recent experiments performed over a wide range of cell types and organelles strongly supported the power-law rheology model (Fabry *et al.* 2001a; Alcaraz *et al.* 2003; Lenormand *et al.* 2004; Yanai *et al.* 2004; Balland *et al.* 2005; Dahl *et al.* 2005; Desprat *et al.* 2005). These latest experiments generally involved improved resolution in terms of time, frequency, and deformation measurement. Thus, the power-law rheology model could be a promising candidate for a general model of cell rheology. Yet, this model has not been confirmed with micropipette aspiration for single cells, which is the basis for other competing models based on the spring-dashpot concept.

In addition, most of the experiments that supported the power-law rheology model were performed on cells adherent to the substrate (or glass microplates in the case of microplate manipulation (Desprat *et al.* 2005)), with the exception of micropipette aspiration of the nuclei (Dahl *et al.* 2005). The power-law rheology model has not been proven for suspended eukaryotic cells. The rheology of cells in suspension becomes interesting especially when one considers the transport and trapping of white blood cells or metastatic cancer cells in the capillaries (Worthen *et al.* 1989; Yamauchi *et al.* 2005). If proven valid, the power-law rheology model will provide a common platform for comparing the rheological properties of both adhered and suspended eukaryotic animal cells.

Lastly, probing adherent cells in suspension may lead to more consistent measurement of the passive mechanics of the cells. It is well known that most anchorage-dependent cells develop stress fibers and contractile stress (or prestress) while adherent to a substrate. The stiffness of the substrate influence the prestress (Discher *et al.* 2005; Saez *et al.* 2005), which in turn will modulate the stiffness and rheology of the cells (Wang *et al.* 2002; Stamenovic *et al.* 2004). For the purpose of measuring the passive rheological behavior of the cell, detaching and suspending the cells will result in less internal active prestress and potentially allow more consistent measurement of the passive mechanics of the cells, as shown by the optical stretcher experiments (Guck *et al.* 2005; Wottawah *et al.* 2005).

As such, the rheology of suspended eukaryotic cells is worthy of study and the power-law rheology hypothesis for single cells needs to be tested with regards to micropipette aspiration.

1.3 Finite element modeling of cell deformation

Interpretation of the viscoelastic properties of cells has widely relied on linear viscoelasticity and analytical solutions (Lim *et al.* 2006). For example, the small deformation of an elastic sphere in micropipette aspiration had been solved analytically, while the viscoelastic properties were then derived using the elastic-viscoelastic correspondence principle (Schmid-Schonbein *et al.* 1981; Theret *et al.* 1988; Sato *et al.* 1990). These analytical solutions are limited to small deformation and cannot correctly account for the slippage between the cell and the pipette wall. However, many mechanical investigations involved large deformation of cells (Van Vliet *et al.* 2003). More importantly, cells frequently experience large deformation in its daily life, which may lead to certain biochemical responses through the process of mechanotransduction (Wang *et al.* 1993; Vogel and Sheetz 2006). As such, mechanical modeling of cells should take into consideration the large deformation induced.

Finite element method solves initial-boundary-value problems numerically and can overcome some of the simplifying assumptions made by analytical methods (Bathe 1996). It has increasingly been applied to the mechanical modeling of cells (e.g. Dong and Skalak 1992; Drury and Dembo 1999; Drury and Dembo 2001; Mijailovich *et al.* 2002; Baaijens *et al.* 2005; Zhou *et al.* 2005a). Thus, the finite element simulation of the viscoelastic deformation of cells under micropipette aspiration may lead to more accurate determination of the rheological properties. In addition, a large-strain viscoelastic finite element model with experimental verification may contribute towards the study of mechanotransduction by predicting the distribution of stress and strain within cells (Guilak et al. 1999; Humphrey 2001; Charras and Horton 2002a; Charras and Horton 2002b; Charras et al. 2004; Lim et al. 2006). However, a finite element model for describing the power-law rheology of the cells is still not available.

1.4 Objectives and scope of work

In view of the above, as the power-law rheology model has not been proven for suspended cells or for micropipette aspiration of cells, the main objectives of this research are:

a. To experimentally investigate the rheology of suspended eukaryotic animal cells using the micropipette aspiration technique and to test the power-law rheology hypothesis in this context.

b. To develop a large-deformation finite element model of cells based on the power-law rheology and to verify it with the experiments performed in (a).

It is hoped that the experimental methodology and theoretical model put forward in this thesis will contribute to a more accurate evaluation of the viscoelastic properties of cells and better understanding of the biological response of cells to mechanical stimuli.

To fulfill the objectives, the scope of this study will include the following:

1. A systematical review of the published mechanical models of cells. The review will examine the strength and limitations of each model as well as the impact of improved experimental techniques on the evolution of mechanical models.
2. NIH 3T3 fibroblasts are chosen as a model system. The cells, while in suspension, will be subjected to linearly increasing suction pressure with micropipette aspiration (ramp tests). The main intention of ramp tests is to optimize the pipette size for producing linear and reproducible deformation of cells, which is the prerequisite for obtaining accurate creep function in creep experiments. The ramp tests will also provide approximate calibration for deformation measurement in micropipette aspiration.
3. Creep tests will be carried out next on suspended fibroblasts using suitable-sized pipettes. Based on creep deformation, creep function is interpreted and used to evaluate the accuracy of the power-law rheology model, in comparison with spring-dashpot ones. In addition, the effect of drug treatments on the mechanical properties of cells will be investigated to understand the relative contribution of two major cytoskeletal filaments.
4. A finite-strain viscoelastic model will be proposed for eukaryotic cells based on the power-law rheology. Finite element simulation is carried out to simulate the micropipette aspiration experiments, including both ramp tests and creep tests. Validation of the model is carried out by comparing the simulation results with those of experiments.

1.5 Organization

The organization of the remainder of this thesis is as follows:

Chapter 2 is the literature review on experimental techniques and mechanical models for studying cell mechanics.

Chapter 3 describes the experimental materials and methods for studying fibroblasts.

Chapters 4 and 5 present the rheology of NIH 3T3 fibroblasts studied with micropipette aspiration. In Chapter 4, the results for ramp tests are reported. The results for creep tests will be presented in Chapter 5.

Chapter 6 presents the finite element simulation of micropipette aspiration of the suspended cells.

The last chapter concludes the thesis by summarizing the major contributions and points out potential future directions.

Chapter 2 Literature Review on Cell Mechanics

Throughout life, living cells in the human body are constantly subject to mechanical stimulations, which may arise from both the external environmental and internal physiological conditions. Depending on the direction, magnitude and distribution of these mechanical stimuli, cells can respond in a variety of ways. For example, fluid shear in the blood vessels can regulate the gene expression of endothelial cells (Chien 2003). The dynamic compression of cartilage are known to modulate the proteoglycan synthesis of chondrocytes (Buschmann *et al.* 1995). Bone cells respond to mechanical stimuli by regulating the bone homeostasis and structural strain adaptation (Cowin 2002). Studies have also shown that many biological processes, such as growth, differentiation, migration, and even apoptosis are influenced by changes in cell shape and micromechanical environment (Chen *et al.* 1997; Boudreau and Bissell 1998; Huang and Ingber 1999; Schwartz and Ginsberg 2002). Therefore, mechanics plays an important role in regulating the physiology of a wide range of cells and thus, the study of cell mechanics may benefit human health by contributing to cellular and tissue engineering and other healthcare applications (Mow *et al.* 1994; Guilak *et al.* 2003).

Studies have also revealed that correlations exist between the diseased state and the aberrant mechanical properties of cells (Suresh *et al.* 2005). Two most prominent cases are malaria and cancer, where deviations in the cellular mechanical properties are directly related to their pathology. For example, healthy human RBCs are flexible and can pass through blood vessels to supply oxygen to the tissues and organs. Unfortunately, these cells are also coveted by the protozoan *Plasmodium falciparum*, the single-cell parasites that cause malaria. Invasion of the parasites causes gross changes in mechanical properties of the RBCs (Nash *et al.* 1989; Cooke *et al.* 2001; Glenister *et al.* 2002; Zhou *et al.* 2004a; Zhou *et al.* 2004b; Zhou *et al.* 2005b), which lead to impairment of blood flow, possibly resulting in coma and even death (Miller *et al.* 2002; Dondorp *et al.* 2004). In the case of cancer, genetic mutations not only cause uncontrolled division of cells but also increase their ability to invade other tissues. The cytoskeleton of cancer cells was generally found to be more compliant than their normal counterparts (Thoumine and Ott 1997a; Guck *et al.* 2005), which has been suggested to facilitate cancer cell metastasis (Ward *et al.* 1991; Beil *et al.* 2003). In addition, alterations in mechanical properties of cells have also been implicated in other types of diseases such as sickle cell anemia (Kaul and Fabry 2004) and arthritis (Jones *et al.* 1999b). Therefore, the mechanical properties of certain types of cells can indicate their diseased state. Mechanical testing of cells may potentially find applications in clinical diagnostics.

Finally, many drugs are known to increase or decrease the mechanical properties of living cells. For example, the chemotactic agent f-Met-Leu-Phe (fMLP) can increase the stiffness of neutrophils (Worthen *et al.* 1989; Zahalak *et al.* 1990); cytochalasin D and latrunculin B can disrupt the actin filament cytoskeleton and adversely affect the stiffness of cells (Sato *et al.* 1990; Wakatsuki *et al.* 2001; Nagayama *et al.* 2006); and colchicines can disrupt the microtubules in the cytoskeleton of neutrophils although this will not significantly affect the mechanical properties as actin filaments are still the primary structural elements (Tsai *et al.*

1998). Therefore, if a disease is caused by mechanical abnormalities of cells (e.g. in the case of malaria), drugs might be administered to intervene with them and this may lead to more effective therapy.

In view of the above, cell mechanics is an important subject of study and mechanical properties of cells are of fundamental and practical interest. The works more closely relevant to the current study will be examined next.

2.1 Experimental techniques in cell mechanics

For the purpose of studying the mechanical properties of cells, various experimental techniques have been employed (Fig. 2.1) (Van Vliet *et al.* 2003). Micropipette aspiration (Mitchison and Swann 1954) applies a hydrostatic suction pressure to the cell surface via a micropipette (Fig. 2.1(a)). Atomic force microscope (AFM) (Fig. 2.1(f)) (Hoh and Schoenenberger 1994), cell indenter (Petersen *et al.* 1982), microplate manipulation (Fig. 2.1(c)) (Thoumine and Ott 1997b) and tensile tester (Miyazaki *et al.* 2000) utilize the application of a pushing or pulling force on the cell surface. Magnetic tweezers (Crick and Hughes 1950; Bausch *et al.* 1998) and magnetic twisting cytometry (MTC) (Wang *et al.* 1993; Maksym *et al.* 2000) impose a torque or force to magnetic beads coupled to the cell surface or internalized into the cytoplasm (Fig. 2.1(e)). Optical tweezers (Henon *et al.* 1999; Lim *et al.* 2004) traps and moves organelles or microbeads coupled to or internalized by the cell (Fig. 2.1(b)). Optical stretcher (Guck *et al.* 2001) deforms the whole cell by applying optical force to the cell surface (Fig. 2.1(d)). Microrheology of the cytoplasm can be non-invasively inferred from intracellular particle tracking

(Yamada *et al.* 2000; Tseng *et al.* 2002). These techniques generally probe different aspects of the mechanical behaviors of the cells. Because of the heterogeneity and viscoelasticity of cells, the measured mechanical properties are very dependent on the techniques. For example, the reported elastic modulus for eukaryotic cells spans several orders of magnitude, varying from a few of Pa to thousands of Pa (Stamenovic and Coughlin 1999; Lim *et al.* 2006). Therefore, multiple factors need to be considered for obtaining consistent and reproducible results with the mechanics of cells.

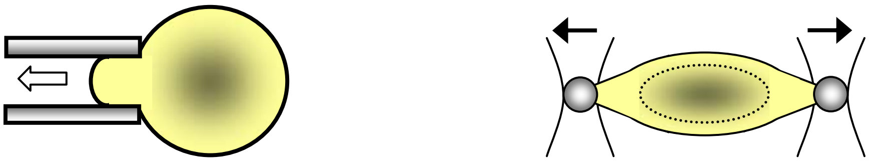

(a) Micropipette aspiration (b) Optical tweezers

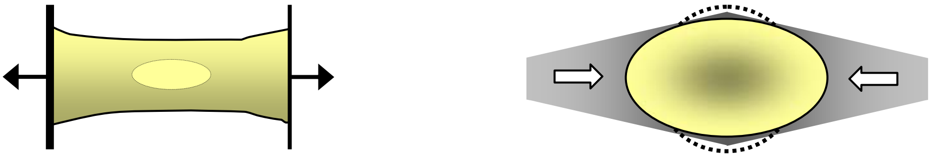

(c) Microplate manipulation (d) Optical stretcher

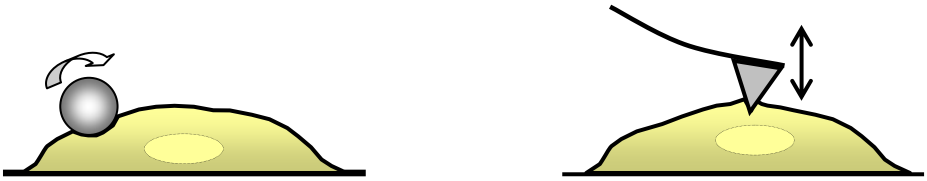

(e) MTC (f) AFM indentation

Fig. 2.1. Experimental techniques for measuring mechanical properties of living cells (Lim *et al.* 2006).

The research performed herein is based on the micropipette aspiration method. Mitchison and Swann (1954) first developed the micropipette aspiration method based on the principle of hydrostatic pressure transmission. The system composes of two main parts, a glass micropipette that directly sucks the cell and a hydrostatic system that controls the suction pressure in the pipette (Fig. 2.2).

Significant progress has since been made in micropipette production, pressure control and calibration, automation and computers, and cell imaging, but the working mechanism remains essentially the same (Hochmuth 2000).

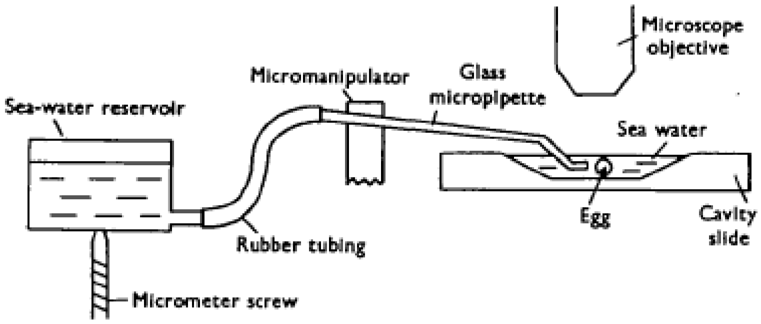

Fig. 2.2. The first experimental setup of micropipette aspiration (Mitchison and Swann 1954).

Micropipette aspiration has played a key role in clarifying the mechanical properties of cells. Mitchison and Swann (1954) performed micropipette aspiration on sea-urchin eggs (~ 100 μm in diameter). Subsequently, this technique has been adapted to measure the mechanical properties of the much smaller red blood cells (Band and Burton 1964; Evans 1973) and white blood cells (Schmid-Schonbein *et al.* 1981; Evans and Kukan 1984). More recently, the micropipette aspiration technique has been applied to study the rheology of anchorage-dependent eukaryotic cells, including endothelial cells, fibroblasts and chondrocytes (Sato *et al.* 1987b; Jones *et al.* 1999b; Thoumine *et al.* 1999).

Micropipette aspiration is therefore very suitable for evaluating the rheological properties of cells and will also be adopted for the current study. One approach to derive the mechanical moduli of cells from the experimental results is through mechanical models, which will be systematically reviewed in the next section.

2.2 Mechanical models for eukaryotic cells

2.2.1 Overview

An overview of the mechanical models developed in the past few decades is shown in Fig. 2.3.

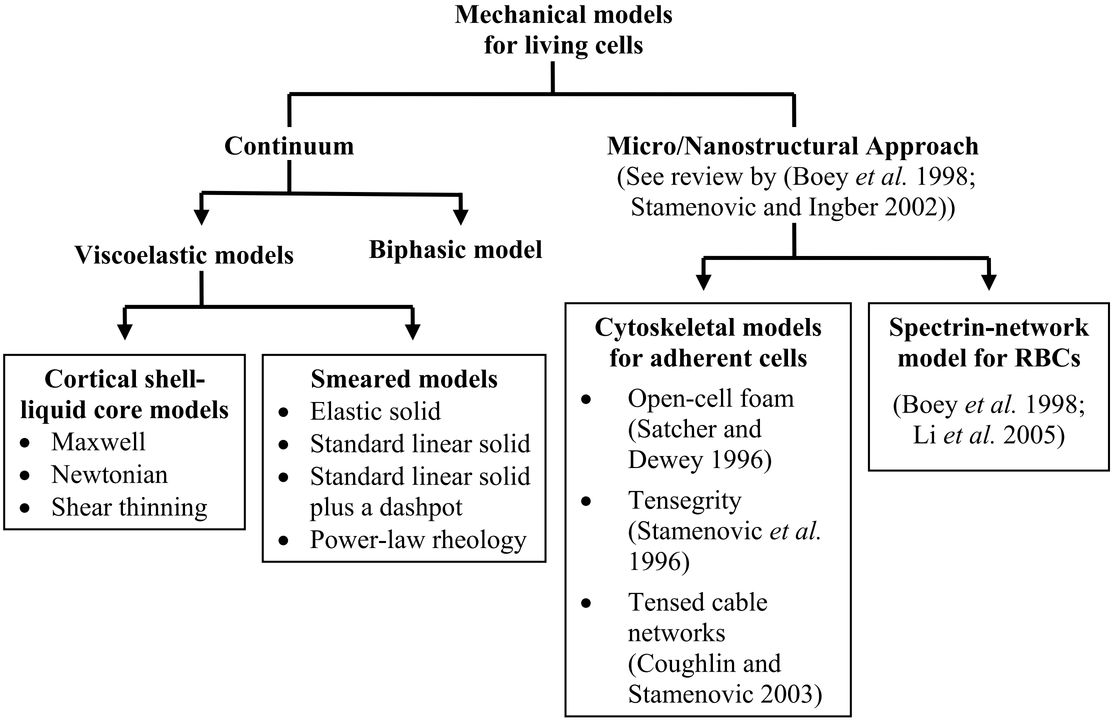
Mechanical models for living cells
Continuum
Micro/Nanostructural Approach
(See review by (Boey et al. 1998; Stamenovic and Ingber 2002))
Viscoelastic models
Biphasic model
Cortical shell-liquid core models
• Maxwell
• Newtonian
• Shear thinning
Smeared models
• Elastic solid
• Standard linear solid
• Standard linear solid plus a dashpot
• Power-law rheology
Cytoskeletal models for adherent cells
• Open-cell foam (Satcher and Dewey 1996)
• Tensegrity (Stamenovic et al. 1996)
• Tensed cable networks (Coughlin and Stamenovic 2003)
Spectrin-network model for RBCs
(Boey et al. 1998; Li et al. 2005)

Fig. 2.3. An overview of mechanical models for living cells (Lim *et al.* 2006).

Generally, these models are derived using either the microstructural approach or the continuum approach. The former deems the cytoskeleton as the main structural component and is especially developed for investigating cytoskeletal mechanics in adherent cells (Satcher and Dewey 1996; Stamenovic *et al.* 1996; Boey *et al.* 1998; Boal 2002; Stamenovic and Ingber 2002; Coughlin and Stamenovic 2003). For suspended cells such as erythrocytes, the microscopic spectrin-network model (Boey *et al.* 1998; Li *et al.* 2005) was developed to investigate the contribution of the cell membrane and spectrin network to the large deformation of red cells.

On the other hand, the continuum modeling approach treats the cell as a continuum material with certain mechanical properties (Humphrey 2003; Lim *et al.* 2006). From experimental observations, the appropriate constitutive material models and the associated parameters are then derived. Although providing less insight into the detailed molecular mechanical events, the continuum approach is easier and more straightforward to use in computing the mechanical properties of the cells if the biomechanical response at the cell level is all that is needed. This approach has been adopted in this thesis and the continuum models will be reviewed next, with emphasis on the constitutive modeling of the viscoelastic behavior of cells.

2.2.2 Cortical shell-liquid core models

The cortical shell-liquid core (CSLC) models were first developed mainly to account for the rheology of neutrophils in micropipette aspiration. The Newtonian liquid drop model, the shear thinning liquid drop model and the Maxwell liquid drop model fall under this category.

2.2.2.1 Newtonian liquid drop model

Leukocytes behave like a liquid drop and adopt a spherical shape when suspended. They can deform continuously into a micropipette with a smaller diameter when the pressure difference exceeds a certain threshold (Fig. 2.4(a)) and can recover its initial spherical shape upon release (Evans and Kukan 1984) (Fig. 2.4(b) – (d)).

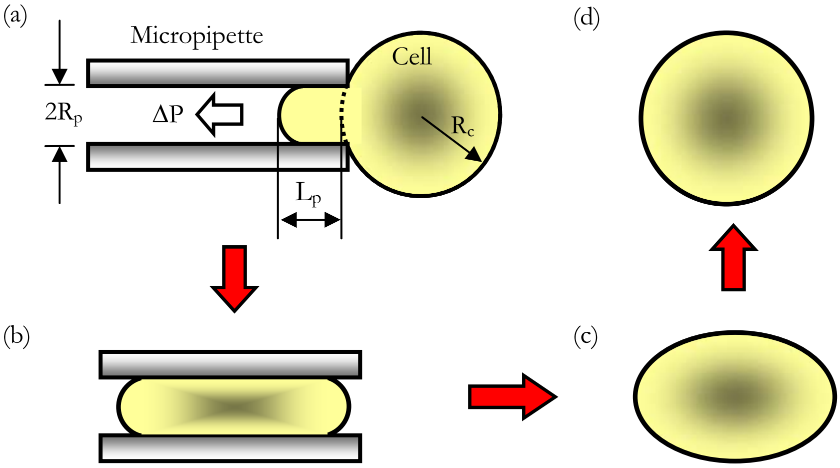

Fig. 2.4. Deformation of a cell in micropipette aspiration. (a) Partial aspiration of a cell at a fixed pressure (ΔP). (b) – (d) A cell is completely aspirated into a pipette, held for a certain period of time and then expelled from the pipette to observe its recovery process.

The Newtonian liquid drop model was thus developed by Yeung and Evans (1989) in an attempt to simulate the flow of such liquid-like cells into the micropipette. In this model, the cell interior was assumed to be a homogeneous Newtonian viscous liquid and the cell cortex was taken as a fluid layer with constant surface tension (Fig. 2.5(a)). In a simple shear test where a Newtonian fluid with viscosity, μ, is subjected to a shear stress, $\tau\,(\tau = 2\mu)$, the change of the shear strain, γ, with time (t) is shown in Fig. 2.5(b).

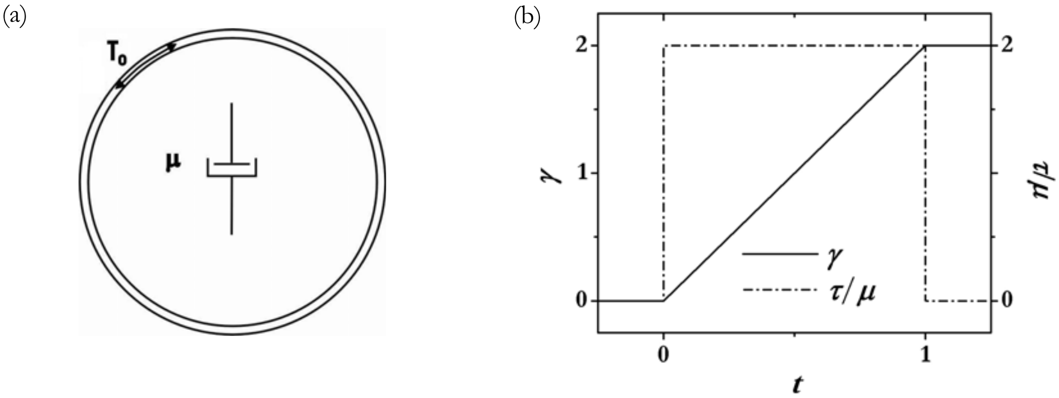

Fig. 2.5. The Newtonian liquid drop model: (a) The cell is modeled as a Newtonian liquid droplet enclosed by a cortical layer with constant tension, T_o. (b) This plot shows the creep response of a Newtonian liquid with viscosity, μ when subjected to a stress, $\tau\,(\tau = 2\mu)$.

The constitutive relations of the Newtonian fluid used by Yeung and Evans (1989) are described by

$$\begin{gathered}\boldsymbol{\tau} = \mu\dot{\boldsymbol{\gamma}} \\ \boldsymbol{\gamma} = \nabla\mathbf{u} + \nabla\mathbf{u}^T \qquad \dot{\boldsymbol{\gamma}} = \nabla\mathbf{v} + \nabla\mathbf{v}^T \qquad \boldsymbol{\tau} = \boldsymbol{\sigma} + p\mathbf{I}\end{gathered} \tag{2.1}$$

where $\boldsymbol{\sigma}$ and $\boldsymbol{\tau}$ are the total and deviatoric stress tensors, respectively; $\boldsymbol{\gamma}$ is the engineering strain tensor same as defined by Ferry (1980) and are equal to the deviatoric strain tensor due to assumed incompressibility; $\dot{\boldsymbol{\gamma}}$ is the strain rate; μ is the shear viscosity; $\mathbf{I}$ is the unit tensor; $\mathbf{u}$ is the displacement field, and $\mathbf{v}$ is the velocity field. Note that the creep response of Newtonian fluid involves no sudden change in strain and the strain is not recoverable upon unloading (Fig. 2.5(b)).

In micropipette aspiration experiment, the critical suction pressure (P_{cr}) is defined as when a static hemispherical projection of the cell body is formed inside the pipette. An excess pressure beyond this threshold will cause the cell to flow into the pipette continuously (provided there is enough excess membrane area to accommodate the incompressible cytoplasm (Evans and Yeung 1989)). The static cortical tension can thus be inferred from P_{cr} according to the law of Laplace

$$T_0 = \frac{P_{cr}}{2\left(1/R_p - 1/R_c\right)} \tag{2.2}$$

where R_p is the radius of the pipette and R_c the radius of the cell body outside the pipette (Fig. 2.4(a)).

Solution to the time-dependent inflow of this model after the formation of a static hemispherical cap was derived by Yeung and Evans (1989) using a variational approach. However, this solution is not in its explicit form. Needham and Hochmuth (1990) simplified it as

$$\frac{\left(\Delta P - P_{cr}\right)}{\mu\left(\dot{L}_p / R_p\right)} = 6\left(1 - \frac{R_p}{R_c}\right) \quad \text{for } 0.5 \le R_p / R_c \le 1.0 \tag{2.3}$$

where ΔP is the total suction pressure, L_p is the deformed projection length of the cell inside the pipette (cf. Fig. 2.4(a)), $\dot{L}_p$ is the rate of change for L_p, R_c is the radius of the cell body outside the pipette corresponding to the point when $\dot{L}_p$ is measured. The above equation can be integrated to yield the theoretical deformation process, i.e. L_p versus time, given the value of μ and the initial and final values of L_p (Needham and Hochmuth 1990). The theoretical deformation process appeared to match the middle portion of the entry process reasonably well (Fig. 2.6). However, the Newtonian model is not able to account for the rapid initial entry into the pipette.

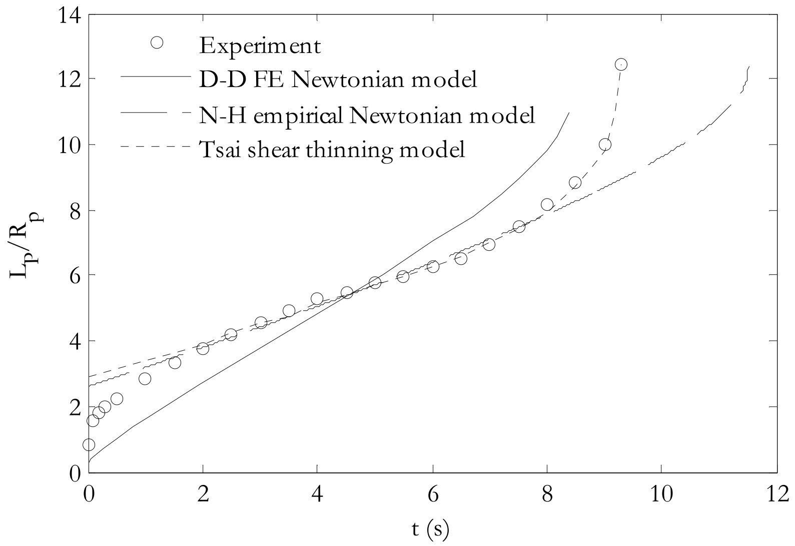

Fig. 2.6. Modeling the micropipette aspiration of neutrophils with CSLC models. Here, R_p = 2 μm and ΔP = 490 Pa. The experimental data (Tsai *et al.* 1993) was fitted by (i) the finite element simulation using the Newtonian model with μ = 92.5 Pa•s, $T_0 = 0.035 \times 10^{-3}$ N/m (Drury and Dembo 1999); (ii) the empirical solution for the Newtonian model (Eq. (2.3)) with an assumed arbitrary initial jump and μ = 280 Pa•s (Needham and Hochmuth 1990); and (iii) the numerical prediction using the shear thinning model with η_c = 55 Pa•s and b = 0.73 (Tsai *et al.* 1993).

Insights can also be gained from the recovery analysis after deformation. The cells were first aspirated into a micropipette to form an elongated sausage shape, held for a period of time, and then expelled out of the pipette (see Fig. 2.4). Tran-Son-Tay *et al.* (1991) found that the recovery process of neutrophils after undergoing large deformation could be fitted by using the Newtonian liquid drop model and derived the ratio between the cortical tension and the cytoplasmic viscosity (T_0/μ) from the recovery experiments. For cells held within a micropipette for a period longer than 5s, the theory agreed well with experiments and the predicted ratio T_0/μ was very close to those predicted by others (Evans and Yeung 1989; Needham and Hochmuth 1990) using the aspiration method thus giving support to the Newtonian liquid drop model. However, if held for less than 5s, the cells would exhibit a fast elastic recoil, analogous to the initial rapid entry in the aspiration test (Evans and Yeung 1989; Needham and Hochmuth 1990), which could not be explained by the Newtonian model.

The Newtonian model has been subjected to further tests for the case of granulocytes flowing down tapered pipettes under certain driving pressures (Bagge *et al.* 1977). The simulation results compare favorably with that of experiments, with the core viscosities very similar to those found by others using the same model (Tran-Son-Tay *et al.* 1994a). Some of the reported mechanical parameters of the Newtonian liquid drop model are listed in Table A.1.

2.2.2.2 Shear thinning liquid drop model

Tsai *et al.* (1993) studied the dependence of the apparent cytoplasmic viscosity on shear rate at large deformation. A large number of human neutrophils were aspirated into pipettes of diameters ranging from 4 to 5 μm and suction pressures between 98 and 882 Pa. Subsequently, the apparent viscosities under different aspiration pressures were computed using the Newtonian liquid drop model (Yeung and Evans 1989). Tsai *et al.* (1993) found that the apparent viscosity of the cytoplasm decreased with increasing aspiration pressure, or the mean shear rate, by a power law relationship:

$$\eta = \eta_c \left(\dot{\gamma}_m / \dot{\gamma}_c \right)^{-b} \tag{2.4}$$

where $\eta_c = 1300 \pm 230 \text{Pa s}$; $\dot{\gamma}_m = 0.14 \sim 7.3 \text{s}^{-1}$; $\dot{\gamma}_c = 1 \text{s}^{-1}$; $b = 0.52 \pm 0.09$. Here, η_c is the characteristic viscosity at characteristic shear rate $\dot{\gamma}_c$, b is the power, and $\dot{\gamma}_m$ is the mean shear rate averaged over the whole process and domain. The instantaneous shear rate $\dot{\gamma}_p$ at a certain point is defined as

$$\dot{\gamma}_p = \sqrt{\frac{1}{2} \boldsymbol{\gamma} : \boldsymbol{\gamma}} \tag{2.5}$$

Substitution of Eq. (2.4) into Eq. (2.1) results in

$$\boldsymbol{\tau} = \eta_c \left(\dot{\gamma}_m \right)^{-b} \dot{\boldsymbol{\gamma}} \tag{2.6}$$

which further simplifies to $\tau = \eta_c \left(\dot{\gamma} \right)^{1-b}$ in the case of simple shear with a constant shear rate. The creep and recovery response of shear thinning fluid is similar to that of Newtonian liquid, but the apparent viscosity $\tau / \dot{\gamma}$ will decrease as the shear stress increases (Fig. 2.7(b)).

Using the Newtonian liquid model, Tsai *et al.* (1993) predicted the speed of aspiration to be almost constant throughout the duration while under constant aspiration pressure. However, this was inconsistent with the observed acceleration at the end of aspiration, immediately before the whole cell was sucked in. In order to better fit this course of aspiration, the power-law constitutive relation was incorporated into the CSLC model (Tsai *et al.* 1993) (Fig. 2.7(a)). The instantaneous apparent viscosity takes the form of a power-law function for the instantaneous mean shear rate. Thus, a positive feedback is established such that an increase in shear rate will lead to decrease in viscosity and this will in turn, lead to a further increase in shear rate, and so on. It was shown that this preliminary shear-thinning model can simulate the experiment better than the Newtonian liquid drop model (Fig. 2.6).

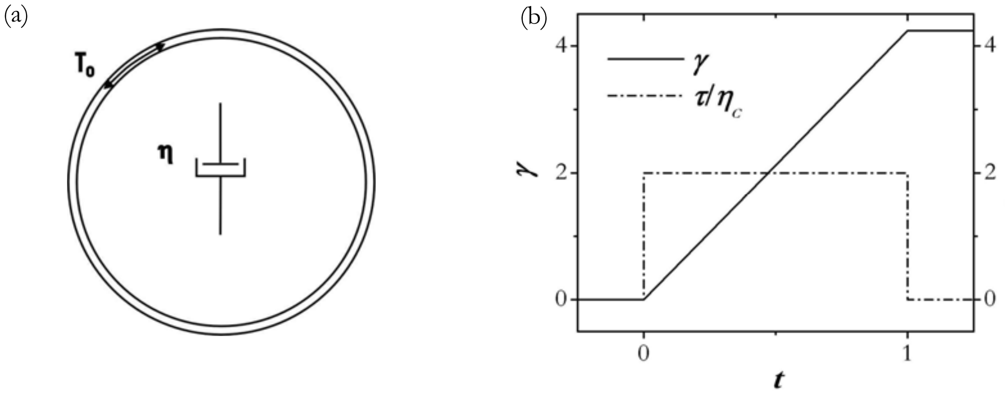

Fig. 2.7. The shear thinning liquid drop model: (a) The cortex of the cell is modeled as a layer with constant tension T_0 and the cytoplasm is modeled as a shear thinning liquid droplet. (b) The plot shows the simple shear creep response of a power law fluid with a characteristic viscosity η_c and $b = 0.52$, subject to shear stress $\tau = 2\eta_c$ (cf. Eq. (2.6)).

The shear thinning liquid drop model is also consistent with some of the *in vitro* rheological studies conducted on polymer solutions. The cytoplasm is rich in polymeric cytoskeletal structures, i.e. actin filaments, microtubules and intermediate filaments. Studies of the polymer solutions of these cytoskeletal components provide insights to the cytoplasm rheology. It is well known that many polymeric fluids show shear thinning behavior, where the viscosity η is related to the shear rate $\dot{\gamma}$ by the power law (Buxbaum *et al.* 1987)

$$\eta = A\dot{\gamma}^{-b} \tag{2.7}$$

where A is a constant and b the power of shear thinning. The power number for macromolecular fluids generally lies between 0.4 and 0.85 at high shear rates ($\dot{\gamma} > 1s^{-1}$) and approaches zero at low shear rates ($\dot{\gamma} < 10^{-2}s^{-1}$) (Bird *et al.* 1987) which is in contrast to the constant viscosity in Newtonian fluids. For cytoskeleton polymer solutions, Buxbaum *et al.* (1987) reported that F-actin (2 ~ 6 mg/ml) and microtubule suspensions (12 mg/ml) behaved as indeterminate fluids with the power $b \approx 1$ at shear rate less than 1 s^{-1} (which means the shear stress is almost invariant with the shear rate: $\tau = \eta\dot{\gamma} \equiv A$). Zaner and Stossel (1982) reported b = 0.69 ~ 0.79 for F-actin (1 ~ 2 mg/ml) at shear rate less than 1 s^{-1}.

Because of the complex geometry, sliding boundary condition and the nonlinear constitutive relations, solving the large deformation problem without discretization of the computational domain can be very challenging. The finite element (FE) method provides a promising alternative solution. Drury and Dembo (1999; 2001) used this method to study the rheology of the micropipette aspiration and the comparison with the Newtonian model and experiment is shown in Fig. 2.6. They performed eight experiments using different pipette radii and suction pressures on neutrophils. Six types of models were compared. The parameters of each model were adjusted to achieve the most desirable match with all the eight experiments. This approach is worth mentioning because an ideal model should perform well under different experimental conditions. According to their study, a model with shear thinning, cortical dissipation and strong membrane-cytoplasmic coupling appears to be the optimal model to use, although there is still considerable discrepancy observed under different experimental conditions. However, the initial rapid entry phase still cannot be accounted for.

It is also of interest to note that small strain dynamic measurements of living cells (including neutrophils) using oscillatory magnetic twisting cytometry (Fabry *et al.* 2003) reveals no evidence of shear thinning. The complex moduli were found to depend only on frequency but not on the shear rate. Therefore, the shear thinning model is probably more suited for modeling large deformation rather than small deformation behavior in cells.

2.2.2.3 Maxwell liquid drop model

While the large deformation regime could be satisfactorily represented by the Newtonian or Newtonian-like models, the small deformation of cells exhibit strong viscoelastic behavior, such as the initial rapid elastic-like entry. Dong *et al.* (1988) applied the Maxwell liquid drop model to study the small deformation and recovery behavior of leukocytes in micropipette aspiration. Their model for a passive leukocyte consisted of a prestressed cortical shell containing a Maxwell fluid (Fig. 2.8(a)).

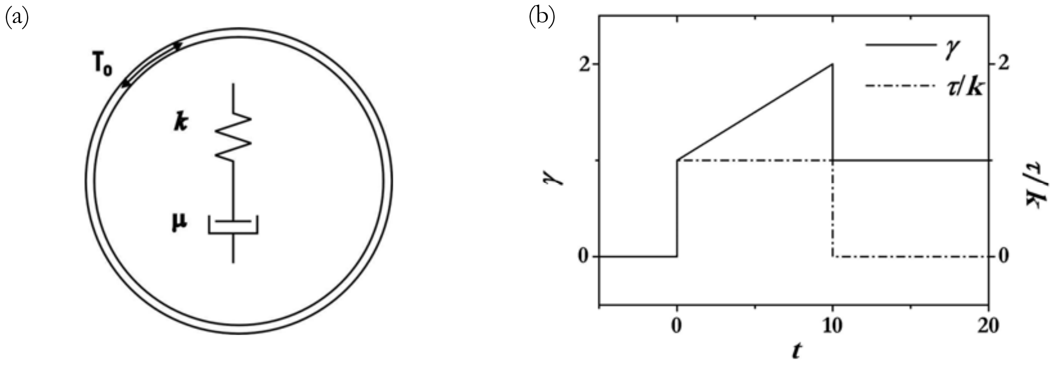

Fig. 2.8. The Maxwell liquid drop model: (a) The cell is modeled as a Maxwell liquid droplet bounded by a constant tension, T_o. (b) This plot shows the creep response (γ) of a Maxwell liquid ($\mu = 10k$) when subjected to a stress τ ($\tau = k$).

The Maxwell constitutive equation used by Dong *et al.* (1988) is given by

$$\boldsymbol{\tau} + \frac{\mu}{k}\boldsymbol{\tau} = \mu\boldsymbol{\gamma} \tag{2.8}$$

where k is an elastic constant and μ a viscous constant, represented as a dashpot and a spring in series. The creep and recovery response of the Maxwell model is shown in Fig. 2.8(b). It is noted that the creep deformation involves an initial jump and can be broken down into a viscous and an elastic component. The elastic part allows for recovery upon unloading.

Series solutions were derived for micropipette aspiration and recovery, assuming spherical initial shape and small deformation. The theoretical results could fit both the initial rapid entry (within several seconds) and the recovery after small deformation with a same set of mechanical parameters (μ = 30 Pa·s, k = 28.5 Pa and T_0 = 0.031 · 10^{-3} N/m). A FE model was also developed to simulate aspiration and the solution was very close to the series solution (Dong *et al.* 1988).

The small deformation FE analysis was later extended to a large deformation FE analysis (Dong *et al.* 1991; Dong and Skalak 1992). It was shown that the Maxwell liquid model could not fit the experimental data unless the values for the viscosity and elasticity of the cytoplasm were allowed to increase continuously as the cell was sucked into the pipette. The elastic modulus was increased from 20 to 260 Pa and the viscosity was increased from 5 to 60 Pa·s, as the sucked-in length increased from 0 to $3R_p$.

This suggests that the small deformation behavior may be fundamentally different from that of large deformation flow. As one may observe from Eq. (2.8), the Maxwell fluid will degenerate into the Newtonian fluid as k approaches infinity. Thus, the cytoplasm seems to undergo a transition from the Maxwell to the

Newtonian behavior while being aspirated into the micropipette with increasing viscosity and elastic modulus.

The recovery study also provides some support to the Maxwell liquid drop model. The sausage-shape deformed cells were found to exhibit a rapid initial elastic recovery if the holding time was very short (less than 5-7 s). However, if the cell was held longer, the recovery was slower and behaved more like a Newtonian liquid (Tran-Son-Tay *et al.* 1991; Hochmuth *et al.* 1993). This phenomenon can be partially explained by the fading elastic memory of a Maxwell liquid.

At this point, a brief summary can be made on the cortical shell liquid core models. First of all, the Newtonian or the shear thinning liquid drop model can account for the large deformation flow and recovery of white blood cells in a consistent manner but cannot explain the viscoelastic aspect of cell deformation. On the other hand, the Maxwell liquid drop model, while being able to model certain viscoelastic behaviors, encounters difficulties in explaining the large deformation behavior in a consistent manner. Indeed, studies of polymeric liquid rheology indicate that the cytoplasm is unlikely to be a simple Newtonian or Maxwell liquid. More complex viscoelastic models might be needed to explain the general viscoelastic behaviors of cells, as will be presented in the following section.

2.2.3 Spring-dashpot smear models

During cell deformation, the resistance arises from different sources, including at least 1) the viscoelasticity of the cortex, cytoplasm and the nucleus, and 2) static surface tension and the active forces of the cytoskeleton. Determination of the relative contribution of these agents is very challenging and difficult to accurately achieve with a single type of experiment at the whole cell level. Therefore, smeared models have been widely adopted to phenomenologically describe the viscoelasticity of cells and to evaluate the mechanical properties of cells, not only for anchorage-dependent cells but also for neutrophils (e.g. Schmid-Schonbein *et al.* 1981; Sato *et al.* 1990; Thoumine and Ott 1997b; Jones *et al.* 1999b; Fabry *et al.* 2001a; Desprat *et al.* 2005; Rosenbluth *et al.* 2006). The smeared models assume the cell to be homogeneous, which reduces the number of mechanical parameters and greatly simplifies the experimental data analysis.

Despite the fact that large deformation is often encountered in mechanical tests, linear viscoelasticity has been widely applied for modeling cells. This is partially justifiable if the relation between force and deformation is approximately linear, which has been shown by experiments for a few cell types (Theret *et al.* 1988; Thoumine and Ott 1997b; Jones *et al.* 1999b; Miyazaki *et al.* 2000).

As the basis of viscoelastic models, the linear elastic model and the relevant analyses will be introduced first. Then, the widely-used standard linear solid model will be discussed. This is followed by a more general model, which is a serial combination of a standard linear solid body with a dashpot.

2.2.3.1 Linear elastic solid model

The elastic model is a simplification of the viscoelastic model where the time factor has been neglected. A linear elastic material is described by

$$\boldsymbol{\tau} = G\boldsymbol{\gamma} \tag{2.9}$$

where G is the shear modulus and is related to the Young's modulus E by $E = 2(1 + v)G$ with v being the Poisson's ratio. Unfortunately, the linear elastic model is generally inadequate for describing the mechanics of cells, because the apparent elasticity of a viscoelastic material will depend on both the loading rate and loading history. However, the linear elastic solution serves as a basis for viscoelastic solution according to the elastic-viscoelastic correspondence principle (Fung 1965). Here, we will discuss elastic solid models that have been derived from experiments conducted on cells using the micropipette aspiration, AFM indentation, cytoindenter and MTC.

In micropipette aspiration, when the pipette radius is very small compared to the local radius of the cell surface, the cell can be approximated as an incompressible elastic half-space (Theret *et al.* 1988). The projection length is predicted to be proportional to the aspiration pressure ΔP and inversely proportional to the elastic modulus as (Theret *et al.* 1988)

$$\frac{L_p}{R_P} = \frac{\Phi_P \Delta P}{2\pi G} \tag{2.10}$$

where L_p is the projection length, R_P the pipette radius, G the shear modulus, and Φ_P is a function of the ratio of the pipette wall thickness to the pipette radius, $\Phi_P = 2.0 \sim 2.1$ when the ratio is equal to 0.2 to 1.0.

For AFM indentation of adherent cells, the force-indentation relationship for a regular square pyramid punch indenting an elastic half-space (Bilodeau 1992) is given as

$$F = \frac{1.4906G}{(1-\nu)\tan\theta}\delta^2 \tag{2.11}$$

with F being the force of indentation, δ the depth of indentation and θ the inclination angle of the triangular faces.

Indentation of adherent cells has also been performed using a cell poker or cytoindenter (Petersen *et al.* 1982; Shin and Athanasiou 1999), where the punch is a plane-ended cylinder. When the punch diameter is relatively small compared to the surface curvature and thickness of the cell, the cell can be idealized as a half-space. The linear elastic solution to this punch problem (Harding and Sneddon 1945) is

$$F = \frac{4R_I G}{1-\nu}\delta \tag{2.12}$$

where R_I is the radius of the indenter, all the other parameters being the same as defined earlier.

Finally, for the MTC experiment, a three dimensional finite element model was constructed to solve the problem (Mijailovich *et al.* 2002). The cell was first modeled as a uniform height slab with a lateral extent of 50 times the bead diameter. The cell material is assumed to be homogeneous, linear elastic and incompressible. Also, the spherical magnetic bead is assumed to be fully adhered to the cell surface. Finally, both the bead and the substrate are assumed to be rigid. The following relationships were obtained (Mijailovich *et al.* 2002)

$$\begin{aligned} \frac{T}{\phi} &= \kappa\alpha_{MMTC}G \\ \frac{T}{d} &= \frac{\kappa\alpha_{OMTC}}{R}G \end{aligned} \tag{2.13}$$

for magnetic MTC (Maksym *et al.* 2000) and for optical MTC (Fabry *et al.* 2001a), respectively. T (Pa) is the applied specific mechanical torque per unit bead volume, κ is a shape factor ($\kappa = 6$ for spherical beads), ϕ is the measured bead rotation, d is the measured lateral bead translation, R is the radius of the bead and α_{MMTC} and α_{OMTC} are geometric coefficients depending on the degree of bead embedding and cell height for magnetic and optical MTC, respectively ($\alpha_{\mathrm{MMTC}} \approx 0.05$ and $\alpha_{\mathrm{OMTC}} \approx 0.055$ for 10% bead diameter embedding, when $2R = 4.5$ μm and the cell height is larger than the bead diameter).

2.2.3.2 Standard linear solid model

The experimental basis for the viscoelastic solid models is that equilibrium can usually be achieved after certain amount of loading. Unlike neutrophils, endothelial cells and chondrocytes were unable to flow into the pipette even when the suction pressure greatly exceeded the critical suction pressure, exhibiting a solid-like behavior (Theret *et al.* 1988; Jones *et al.* 1999b). Furthermore, endothelial cells exposed to fluid shear stress are known to retain an elongated configuration even after detachment. Theret *et al.* (1988) attributed this nonspherical shape to the reassembly of the cytoskeleton elements in response to the shear stress and pointed out that the cytoplasm behaves more like a solid than fluid in this case.

The standard linear solid (SLS) model (Fig. 2.9) was first proposed by Schmid-Schonbein *et al.* (1981), which takes the form

$$\boldsymbol{\tau} + \frac{\mu}{k_2}\dot{\boldsymbol{\tau}} = k_1\boldsymbol{\gamma} + \mu\left(1 + \frac{k_1}{k_2}\right)\dot{\boldsymbol{\gamma}} \tag{2.14}$$

where k_1 and k_2 are two elastic constants and μ is a viscous constant, represented by two springs and one dashpot as shown in (Fig. 2.9(a)). However it is noted that because $\boldsymbol{\gamma}$ is defined as engineering strain (cf. Eq. (2.1)), the parameters k_1, k_2 and μ used in this equation are only half of those in the original SLS model (Schmid-Schonbein *et al.* 1981; Sato *et al.* 1990). Such a modification is beneficial because it will not only make the parameters for the SLS model comparable to those in the other models, but it will also render the elastic and viscous constants analogous to shear moduli and viscosity, respectively.

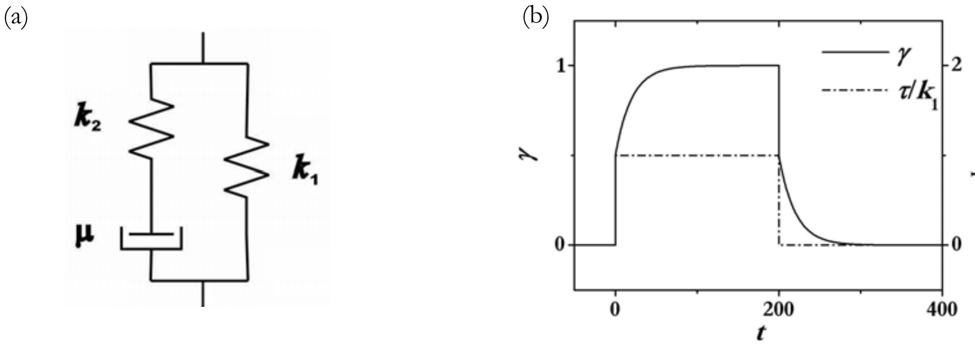

Fig. 2.9. The homogeneous standard linear solid model. (a) The whole cell is modeled as a homogeneous viscoelastic standard linear solid (SLS). (b) The plot shows the creep response (γ) of a standard linear viscoelastic solid ($k_1 = k_2$ and $\mu = 10k_1$) when subjected to a stress τ ($\tau = k_1$).

The creep function of the SLS model is given by

$$J(t) = \frac{1}{k_1}\left[1 - \frac{k_2}{k_1 + k_2} e^{-t/\tau_C}\right] H(t) \tag{2.15}$$

where $\tau_C = \mu(k_1 + k_2)/(k_1 k_2)$ is the characteristic creep time and $H(t)$ is the Heaviside function. The creep and recovery behavior of this model is shown in Fig. 2.9(b). The micropipette aspiration of the SLS viscoelastic half-space can be derived from the solution of the analogous elastic problem (Eq. (2.10)) according to the elastic-viscoelastic correspondence principle (see Appendix B.4) (Sato *et al.* 1990)

$$\frac{L_p(t)}{R_P} = \frac{\Phi_P \Delta P}{2\pi} \frac{1}{k_1}\left[1 - \frac{k_2}{k_1 + k_2} e^{-t/\tau_C}\right] H(t) \tag{2.16}$$

where Φ_P is defined as that in the elastic solution (see Eq. (2.10)). Similar to the micropipette aspiration problem, viscoelastic creep solutions can also be derived for other types of experiments, e.g. flat-punch indentation, AFM indentation and MTC, for which the corresponding elastic solutions exist.

Although the SLS model was originally proposed for modeling leukocytes, the leukocytes had been more widely modeled with the liquid drop models (cf. Section 2.2.2). On the other hand, several types of anchorage-dependent cells including endothelial cells, osteoblasts, chondrocytes, and the cell nuclei have been suggested to exhibit the SLS material behavior (Theret *et al.* 1988; Jones *et al.* 1999b; Guilak *et al.* 2000; Koay *et al.* 2003). Some of the mechanical parameters obtained by various researchers using the SLS model are presented in Table A.2.

It is noted that interpretation of the cell deformation in micropipette aspiration has been based on the half-space model. In reality, a cell has a finite radius and thus is far from being a half-space. Therefore, the effect of pipette geometry on the cell deformation and the accuracy of the half-space model is worthy of being further evaluated.

2.2.3.3 Standard linear solid-dashpot model

In order to account for the displacement of magnetic beads bounded to cell surface or phagocytized into the cytoplasm in response to a step magnetic force, a more complex spring-dashpot model was used by Bausch *et al.* (1998; 1999). The model is a serial combination of an SLS body with a dashpot (SLS-D), which has a creep function of

$$J(t)=\frac{1}{k_1}\left[1+\left(\frac{k_1}{k_1+k_2}-1\right)e^{-t/\tau_c}\right]H(t)+\frac{t}{\mu_0}H(t) \qquad (2.17)$$

where μ_0 is the additional viscous constant. Both the creep and recovery processes could be fitted by the SLS-D model. Fig. 2.10(a) shows the mechanical analog and Fig. 2.10(b) shows the creep and relaxation behavior of this model.

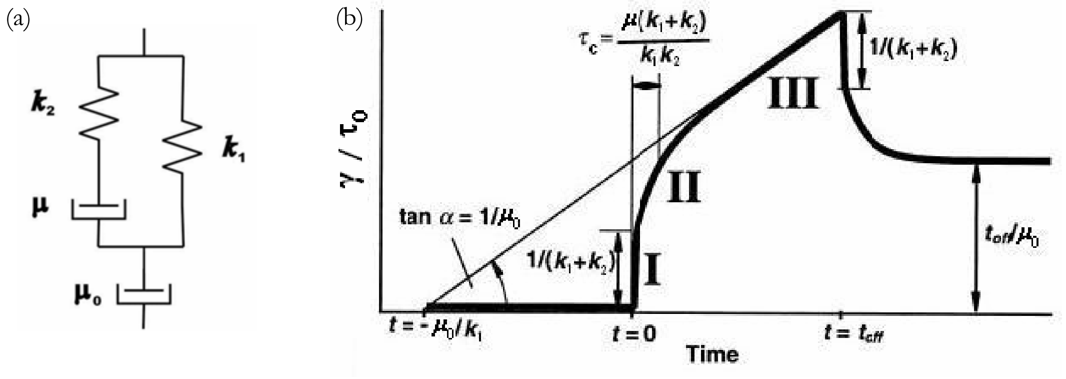

Fig. 2.10. The SLS-D model. (a) The spring-dashpot analog. (b) The normalized creep and relaxation response of this model when subjected to a constant stress τ_0 between $t = 0 \sim t_{off}$ (adopted from (Bausch *et al.* 1998)). The creep process is composed of three phases: a fast elastic response (I), a relaxation regime (II) and a flow regime (III).

A reduced form of this model, where k_2 was taken as infinity, has been applied to simulate the rotation of chains of magnetic endosomes inside a HeLa cell in response to a rotating magnetic field (Wilhelm *et al.* 2003) and the creep deformation of suspended fibroblasts in optical stretcher experiment (Wottawah *et al.* 2005). In the former case, the experimental rotating process could be well fitted by the theoretical model. In the later case, however, the model could only describe the short-term loading cases but became inaccurate for cases where the stretching lasted for more than 10 s.

From the discussion above, it seems apparent that as the number of springs and dashpots increases, the power to fit viscoelastic deformation processes increases. However, more complex spring-dashpot models have several drawbacks. Firstly, it may bring uncertainty into the curve fitting if the parameters cannot be uniquely determined. Secondly, it is difficult to give meaningful physical interpretation to the numerous springs and dashpots. More importantly, the spring-dashpot models were generally developed in the context of creep experiment in the time domain. The ability of these models in fitting the dynamic moduli of cells in the frequency domain remains to be evaluated.

2.2.4 Power-law rheology model

Oscillatory MTC (Maksym *et al.* 2000; Fabry *et al.* 2001a) and AFM (Mahaffy *et al.* 2000; Alcaraz *et al.* 2003) are popular techniques used for conducting dynamic tests on adherent cells. For both dynamic tests, low amplitude sinusoidal force signal resulted in a sinusoidal displacement at the same frequency but exhibited a phase lag in the steady-state. In the oscillatory AFM experiment, the oscillatory force is expressed as $F(t)-F_0=\mathrm{Rl}\left[A_F e^{i\omega t}\right]$ where F_0 is the operating force around which the indentation force F oscillates, A_F is the amplitude of this oscillation, ω is the angular frequency ($\omega = 2\pi f$, f being the frequency) and Rl[·] denotes the real part of a complex number. On the other hand, the oscillatory indentation is expressed as $\delta(t)-\delta_0=\mathrm{Rl}\left[A_\delta e^{i(\omega t-\psi)}\right]$ where δ_0 is the operating indentation depth around which the indentation δ oscillates, A_δ is the amplitude of this oscillation, ψ is the phase lag and Rl[·] denotes the real part. The frequency domain solution can be obtained from the corresponding elastic solution according to the correspondence principle (Fung 1965). Applying Taylor expansion to Eq. (2.11) around the operating indentation depth δ_0 and using the Fourier transform, Alcaraz *et al.* (2003) derived the equation for interpreting the complex shear modulus as

$$G^*(\omega)=G'+iG''=\frac{(1-\nu)\tan\theta}{3\delta_0}\left[\frac{A_F}{A_\delta}e^{i\psi}-i\omega b(0)\right] \tag{2.18}$$

where the term $i\omega b(0)$ is a correction term that accounts for the hydrodynamic drag force due to the viscous friction imposed on the cantilever by the surrounding fluid, and G' and G'' are the dynamic storage modulus and loss modulus, respectively.

Similarly, in the oscillatory MTC experiment, the formula for interpreting complex modulus stems from the corresponding elastic solution, Eq. (2.13). Both α_{OMTC} and α_{MMTC} are independent of frequency, thus the equations can be extended to account for the complex shear modulus as long as the linear viscoelasticity is obeyed (Mijailovich *et al.* 2002). Assuming $T(t) = \mathrm{Rl}\left[A_T e^{i\omega t}\right]$ and $\phi(t) = \mathrm{Rl}\left[A_\phi e^{i(\omega t-\psi)}\right]$ (for magnetic MTC) or $d(t) = \mathrm{Rl}\left[A_d e^{i(\omega t-\psi)}\right]$ (for optical MTC), we have

$$
\begin{aligned}
G^*(\omega) &= \frac{1}{\kappa\alpha_{MMTC}} \frac{A_T}{A_\phi} e^{i\psi} \\
G^*(\omega) &= \frac{R}{\kappa\alpha_{OMTC}} \frac{A_T}{A_d} e^{i\psi}
\end{aligned}
\tag{2.19}
$$

for magnetic MTC and optical MTC, respectively.

Importantly, in both the oscillatory MTC and AFM experiments, the storage modulus G' of the cells (including human bronchial and alveolar epithelial cell lines (Alcaraz *et al.* 2003), human airway smooth muscle cells, human lung epithelial cells, mouse embryonic carcinoma cells, mouse pulmonary macrophages and human neutrophils (Fabry *et al.* 2003)) was found to depend on the frequency (ranging from 10^{-2} to 10^3 Hz) according to a weak power law with a constant exponent between 0.1 and 0.4. The loss modulus G'' exhibited similar power-law frequency dependence at low frequency (< ~ 10 Hz) but a Newtonian viscous component became significant at high frequency (Fig. 2.11) (Fabry *et al.* 2001a; Alcaraz *et al.* 2003; Fabry *et al.* 2003). Such a weak power-law behavior has been suggested to be characteristic of soft glassy materials existing close to a glass transition (Sollich 1998; Fabry *et al.* 2001a), which indicates that the cytoskeleton might be a scale-free network in that it possess no internal scale that can typify the number of interactions per protein (Jeong *et al.* 2000; Fabry *et al.* 2003). Therefore it will exhibit a continuous spectrum of relaxation time, instead of the discrete spectrum shown by the spring-dashpot models. To model the observed rheological behavior of the adherent cells, the power-law rheology (PLR) model (also called power-law structural damping model or soft glassy rheology model) was proposed (Fabry *et al.* 2001a)

$$G^*(\omega) = G' + iG'' = G_0\left(\frac{i\omega}{\omega_0}\right)^{\alpha}\Gamma(1-\alpha) + i\omega\mu \qquad (2.20)$$

where α is the exponent of the power law ($0 < \alpha < 1$) ($\tan(\alpha\,\pi/2)$ represents the structural damping coefficient), μ is the Newtonian viscous term, ω is the angular frequency, $\Gamma(\cdot)$ denotes the gamma function and G_0 and ω_0 are scaling factors for stiffness and frequency, respectively (note that $G' = G_0\cos(\pi\alpha/2) \approx G_0$ when $\omega = \omega_0$ and $\alpha \to 0$). This model fitted the experimental data very well, whereas the SLS-D spring-dashpot model could not (Fig. 2.11). This illustrates the inherent limitation of spring-dashpot models in describing frequency domain tests of real materials (Pritz 1996). In the experiment for a single cell type, the plot of G′ against angular frequency curves for different drug treatments have been found to pass a common point, (G_0, ω_0), which indicates that G_0 and ω_0 are approximately invariant with drug treatments (Fabry *et al.* 2003). More recently, oscillatory experiments done with optical tweezer also provided support to the PLR model (Yanai *et al.* 2004; Balland *et al.* 2005).

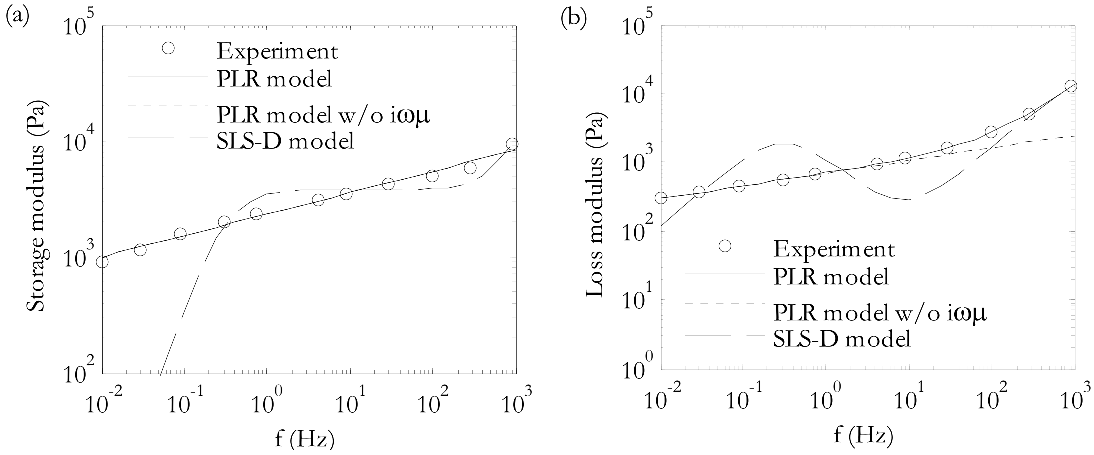

Fig. 2.11. Modeling the oscillatory twisting cytometry of human airway smooth muscle cells. (a) Storage modulus; (b) loss modulus. The experimental data (Fabry *et al.* 2001a) was fitted by (i) the PLR model (Eq. (2.20)) with $G_0\omega_0^{-\alpha}$ = 1733 Pa·s$^{\alpha}$, α = 0.185 and μ = 1.76 Pa·s (Djordjevic *et al.* 2003), (ii) the PLR model without the Newtonian term $i\omega\mu$ ($G_0\omega_0^{-\alpha}$ = 1733 Pa·s$^{\alpha}$, α = 0.185), and (iii) the SLS-D model (Eq. (B.6)) (k_1 = 3812 Pa, k_2 = 33627 Pa, μ = 2.6 Pa·s, and μ_0 = 1900 Pa·s). Note that the curves for PLR models with and without $i\omega\mu$ are completely overlapped in (a).

The Newtonian term $i\omega\mu$ in Eq. (2.20) is only significant at high frequency (or short time). Neglecting this term will only slightly affect the accuracy of curve fitting and the prediction of other PLR parameters ($G_0\omega_0^{-\alpha}$ and α) (Fig. 2.11). In addition, the factor $\Gamma(1 - \alpha)$ in Eq. (2.20) should be omitted as it will lead to a prediction of infinite loss modulus at the limit of α approaching 1 (see Appendix B.3 and B.4). Thus the simplified PLR model has been widely used (Lenormand *et al.* 2004; Yanai *et al.* 2004; Dahl *et al.* 2005; Desprat *et al.* 2005)

$$G^*(\omega) = G_0\left(\frac{i\omega}{\omega_0}\right)^{\alpha} \tag{2.21}$$

For convenience, ω_0 can be taken as 1 rad/s such that

$$G^*(\omega) = G_0\Big|_{\omega_0=1\ \mathrm{rad/s}}\left(\frac{i\omega}{1\ \mathrm{rad/s}}\right)^{\alpha} = A_G\left(i\omega\right)^{\alpha} \tag{2.22}$$

where $A_G = G_0\omega_0^{-\alpha} = G_0\big|_{\omega_0 = 1\ \text{rad/s}}$ is the stiffness constant corresponding to ω_0 = 1 rad/s and the unit of ω is taken as rad/s. A_G equals the magnitude of complex modulus at ω = 1 rad/s, $|G^*(1\ \text{rad/s})|$.

For this model, it can be shown that both the relaxation modulus and the creep function will follow power-law function of time (see Appendix B.3 and B.4). Three different experiments using magnetic twisting cytometry (via magnetic beads coupled to cell surface) (Lenormand *et al.* 2004; Bursac *et al.* 2005), microplates stretching of whole cells (Desprat *et al.* 2005), and pulling of intracellular organelles by optical trap (Yanai *et al.* 2004) measured the creep functions of several types of cells. The creep function of the isolated nuclei had also been measured with micropipette aspiration (Dahl *et al.* 2005). It was found that the creep functions could be faithfully fitted by a simple power law

$$J(t) = J_0\left(\frac{t}{t_0}\right)^{\alpha} \tag{2.23}$$

where J_0 and t_0 are constants for creep compliance and time, respectively. For convenience, t_0 can be taken as 1 s such that

$$J(t) = J_0\big|_{t_0 = 1\ \text{s}}\left(\frac{t}{1\ \text{s}}\right)^{\alpha} = A_J t^{\alpha} \tag{2.24}$$

where $A_J = J_0\big|_{t_0 = 1\ \text{s}}$ is the creep compliance corresponding to t_0 = 1 s and the unit of t is in seconds. From the creep function, the corresponding complex modulus can be derived as $G^*(\omega) = (i\omega)^{\alpha} \big/ \left[A_J\Gamma(1+\alpha)\right]$ (Desprat *et al.* 2005), a comparison of which with Eq. (2.22) indicates that $A_G = 1\big/\left[A_J\Gamma(1+\alpha)\right]$.

This PLR model was later shown to be explained by the fractional derivative viscoelasticity (Appendix B.3) (Djordjevic *et al.* 2003). More interestingly, the dynamic rheological properties of adherent cells were found to be related to the contractile stress – the larger the contractile stress, the higher the dynamic moduli (Stamenovic *et al.* 2004). Some of the reported mechanical parameters for the PLR model are presented in Table A.3.

2.2.5 Summary

With the advancement in experimental techniques, especially the capability to perform oscillatory experiments, the complex moduli and the creep function of cells can be measured with greater accuracy than before. A series of latest experimental results revealed that the cells have a continuous relaxation spectrum which cannot be explained by the classical spring-dashpot models. The PLR model, despite having fewer parameters than the spring-dashpot models (e.g. SLS-D), was found to more accurately describe the viscoelastic behavior of cells in both the time and frequency domains, matching results from different experimental techniques (e.g. microplate manipulation, optical tweezers, AFM and MTC).

Although evidence in support of the PLR model is becoming substantial, this model has not been confirmed with micropipette aspiration for cells, which was the basis for other competing models, such as the SLS model. The published data appears inconsistent with the PLR model (Evans and Kukan 1984; Needham and Hochmuth 1990; Jones *et al.* 1999b; Thoumine *et al.* 1999). Therefore, it would be necessary to re-examine the creep function of cells in response to micropipette aspiration.

Furthermore, all the experiments that supported the power-law model were on cells adherent to the substrate. The applicability of the PLR model to suspended cells has not been established. The optical stretching of suspended NIH 3T3 fibroblasts suggested that the PLR model is not applicable (Wottawah *et al.* 2005). However, one major concern remains for this technique. The effect of laser heating (Peterman *et al.* 2003), which may cause denaturation of proteins and alteration in rheological properties, has not been quantified for cells.

In view of the above, the micropipette aspiration technique was used in this work to examine the rheology of suspended NIH 3T3 fibroblasts (Chapter 3 ~ 5). It may not only serve to evaluate the applicability of different viscoelastic models but may also provide fresh insights into the relation between contractile stress and cell rheology (Stamenovic *et al.* 2004).

Chapter 3 Experimental Setup and Procedures

This chapter describes the methods for the micropipette aspiration experiments as well as cell culture and drug treatments performed in this thesis.

3.1 Micropipette aspiration technique

3.1.1 Fabrication of glass micropipettes and chambers

In order to perform the micropipette aspiration experiments, glass micropipettes were needed. Here, borosilicate glass capillaries with outer and inner diameters of 1.0 and 0.75 mm, respectively (World Precision Instruments, USA) were used to produce micropipettes with inner diameters of 2 ~ 11 μm using a micropipette puller and a microforge (ALA Scientific Instruments, Inc., USA). The pipette wall thickness ranges from 1.3 μm for a 2.2 μm pipette to 3.3 μm for a 10 μm pipette. The tips of the glass pipettes were coated with Sigmacote (Sigma Chemical, St. Louis, MO), which forms a hydrophobic thin film that prevents adhesion. Upon release of pressure after aspiration, cells were observed to detach from the pipette readily.

Glass chambers with side opening were made by sandwiching 6 layers of parafilm between two glass coverslips. Two layers of aluminum foil were then wrapped around the chambers to improve heat conductivity (Fig. 3.1).

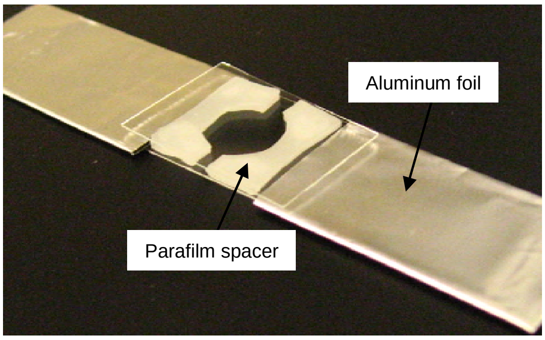

Fig. 3.1. Glass chamber for containing cell sample. The length and width of the chamber are 60 and ~ 10 mm, respectively.

3.1.2 Temperature control

The glass chamber was loaded with cell suspension and placed on a heating stage. The temperature was set at 37.5°C by a temperature controller (Leica, Germany). Due to heat loss, the temperature of the cell suspension was measured using a thermocouple to be about 30°C. It was noticed that if the temperature was set higher by about 2 ~ 3°C, the cells started to adhere and spread on the glass slide and this was undesirable. Hence, the temperature was maintained at 30°C.

3.1.3 Setup of the hydrostatic loading system

The micropipette aspiration system is in principle similar to those used by others (see review by Hochmuth 2000). The schematic design of the setup is shown in Fig. 3.2(a) and the photograph of the actual setup is shown in Fig. 3.2(b). Briefly, micropipettes were filled with the same medium for suspending cells and connected to a hydrostatic system which was composed of two reservoirs, a reference one and a variable one (Fig. 3.2). The water level of the reference reservoir was usually adjusted to equate that in the cell chamber and then kept constant. The water level of the variable reservoir can be adjusted either manually by a syringe or automatically by a precision pump (Cole-Parmer, USA) (Fig. 3.2(b)). The suction pressure, which is equal to the pressure difference between the variable and reference reservoirs, was inferred from the voltage output of a pressure transducer (Validyne Engineering, USA) with a resolution of 2.5 Pa (Fig. 3.2). The pressure transducer was calibrated based on the law of hydrostatic pressure. Within the working range of the transducer (pressure difference less than 14 mmH_2O), the pressure difference is proportional to the voltage output with a slope of 28 mmH_2O/V. Fine movement of the micropipette was controlled by a micromanipulator (Eppendorf AG, Germany) (Fig. 3.2(b)).

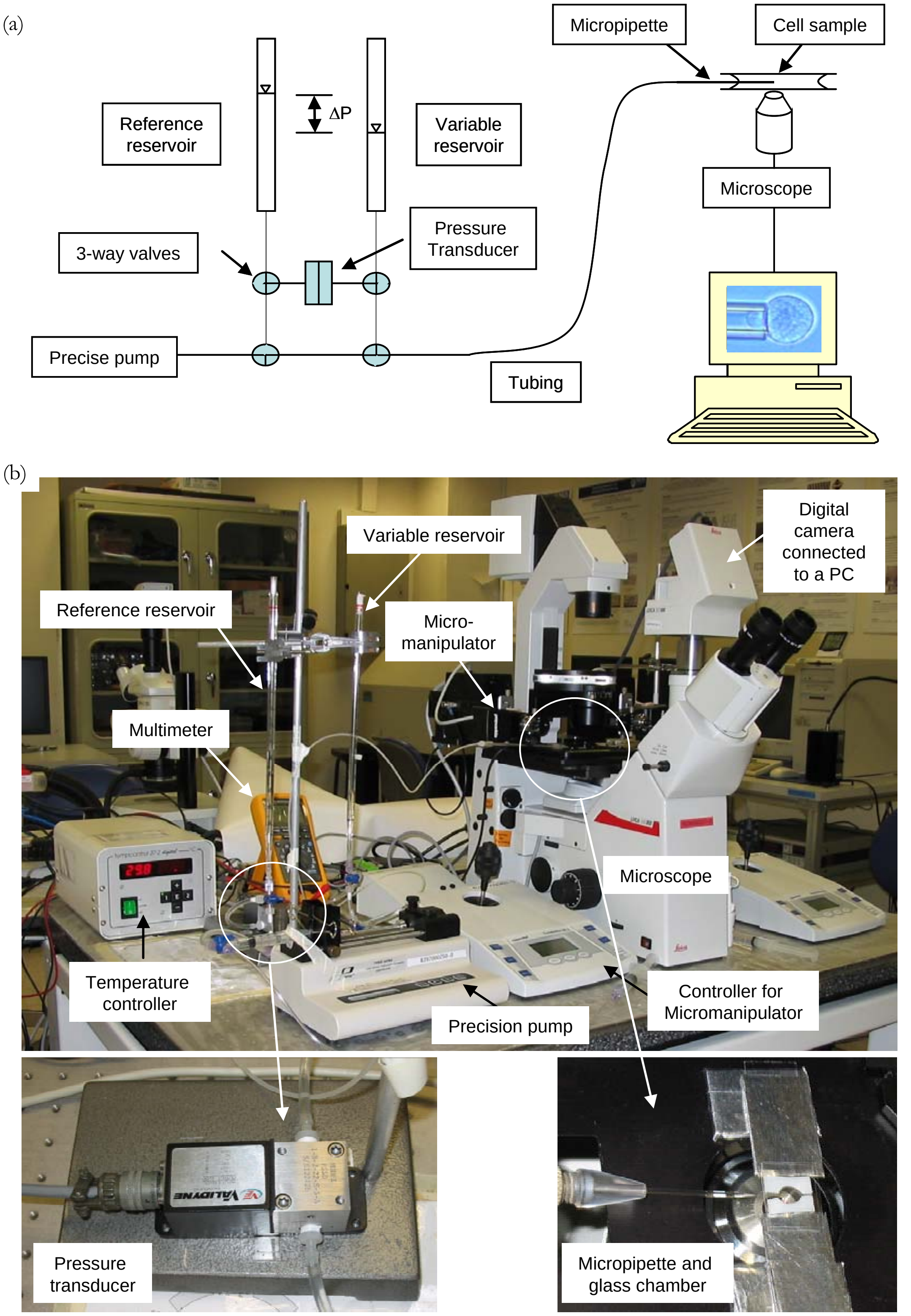
(a)
Micropipette
Cell sample
Reference reservoir
ΔP
Variable reservoir
Microscope
3-way valves
Pressure Transducer
Precise pump
Tubing
(b)
Variable reservoir
Digital camera connected to a PC
Reference reservoir
Micro-manipulator
Multimeter
Microscope
Temperature controller
Precision pump
Controller for Micromanipulator
Pressure transducer
Micropipette and glass chamber

Fig. 3.2. Experimental setup for micropipette aspiration. (a) Schematic of the setup. (b) Photograph of the setup.

The cells were viewed with a Leica microscope (Leica, Germany), using a 63x objective (numerical aperture = 0.7). Microscopic images were taken with a digital camera (Leica, Germany). Image dimensions were analyzed with the image analysis software, Image-Pro Plus (Media Cybernetics, USA). Fig. 3.3 shows the measurement of the typical image dimensions, the pipette diameter $2R_p$ and the total aspirated or projection length L_p^T.

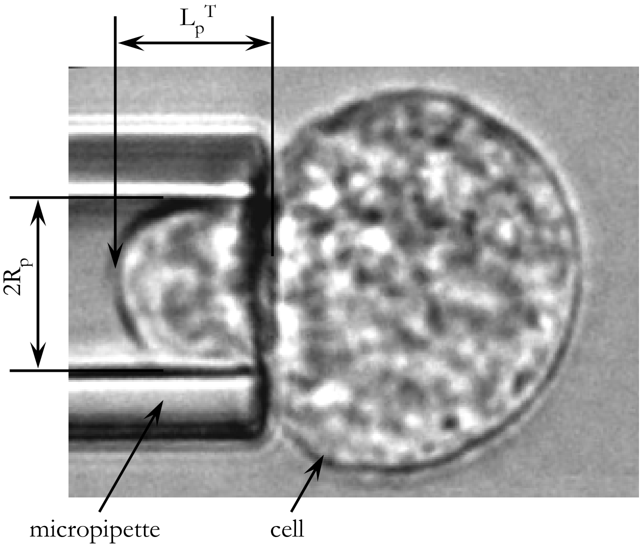

Fig. 3.3. Measurement of pipette diameter ($2R_p$) and total protrusion length (L_p^T) of a cell undergoing micropipette aspiration.

3.1.4 Testing procedures

During the ramp tests, the suction pressure on the cell was linearly increased from zero to 2 cmH_2O by constantly decreasing the water level in the variable reservoir with the precision pump. Image acquisition was started simultaneously with the aspiration of the cell. Two loading rates were employed (1/30 and 1/120 cmH_2O/s) to examine the rate effect. Different pipettes with radii ranging from 2 to 10 μm were used to systematically examine the effects of pipette size.

During the creep tests, a specific volume of water was withdrawn from the variable reservoir to achieve a constant suction pressure of 1 cmH_2O. Subsequently, image acquisition was initiated once the cell sealed the pipette. The frequency of image acquisition was 1 frame/s for the first 10 seconds and 1 frame per 4 s thereafter. The total creep time for each test was 100 s.

To avoid possible cell lysis during the experiment, all cells were tested within one hour after being harvested. Usually 8 ~ 12 cells could be tested within one hour using the present setup.

3.1.5 Accuracy in the measurement of pressure and time

During the creep experiments, the pressure was manually adjusted by a syringe and measured by the pressure transducer as 10.2 ± 0.8 mmH_2O (or 100 ± 7.9 Pa, 153 measurements). The creep time was measured from the start of deformation. Although efforts were made to start the suction of the cell and image acquisition at the same time, errors in determining the actual starting time occurred inevitably. The time between the start of deformation and the acquisition of the first image is always between 0 and 1 s. The starting time is assumed to be at 0.5 s on the average and has a nominal standard deviation of 0.17 s, which was derived by assuming a normal distribution with most (99.7%) of the starting time points falling between 0 and 1 s (NIST/SEMATECH 2005).

For the ramp tests, the loading rate was controlled by the precision pump with an accuracy of ± 1%, according to the manufacturer’s specifications. The time lag between the starting of image capturing and pressure application is always less than 1 s. Thus, the error in the absolute pressure value will be less than 1/30 and 1/120 mm, for the loading rates of 1/30 and 1/120 cmH_2O/s, respectively.

3.2 Cell culture

NIH 3T3 fibroblast cell line was obtained from the American Type Culture Collection (Manassas, VA). The cells were grown in Dulbecco’s minimum essential medium (DMEM), supplemented with 10% fetal bovine serum (FBS), 100 units/ml penicillin and 100μg/ml streptomycin. The cells were maintained at 37°C and 5% CO_2 in an incubator and subcultured every 3 - 4 days. Cells were tested between passage 20 and 30, during which the change in growth rate, morphology and mechanical properties was unnoticeable. Prior to the micropipette aspiration experiments, cells at subconfluent stage were gently detached with a cell scraper and suspended in DMEM with 10% FBS. 25 mM HEPES was supplemented to maintain the pH value, which was measured to be 7.8 ~ 7.9 at room temperature.

3.3 Drug treatments

For disrupting the actin cytoskeleton of the cells, stock solution of cytochalasin D (cytoD) was first made by dissolving cytoD powder in DMSO to 2 mM (1 mg/ml). Immediately prior to drug treatments, the stock solution was diluted in fresh culture medium to a final concentration of 2 μM. The drug-containing medium was used to replace that in the cell culture chambers, which were then placed back into the incubator for 30 minutes. The treated cells were subsequently detached with a cell scraper, suspended in the drug-containing medium, and tested with the same procedure as that for untreated ones (cf. Section 3.1.4). As a control experiment for cytoD treatment, the effect of 0.1% DMSO was also tested using the same procedure.

For disrupting the microtubules, stock solution of colchicine was first made by dissolving colchicine powder in deionized water to 100 mM (40 mg/ml). The final concentrations for cell treatments included 100 μM and 1 mM. The testing procedure is the same as that described for cytoD.

3.4 Staining of actin filaments

For cells grown on glass coverslips, the following steps were adopted.

(1) Fix cells in 4% paraformaldehyde in phosphate buffered saline solution (PBS) for 20 minutes.

(2) Wash cells in PBS.

(3) Permeabilize cells with 0.5% Triton-X-100 in PBS for 10 minutes.

(4) Wash cells in PBS.

(5) Incubate cells in 1 μg/ml TRITC-labeled phalloidin in PBS for 15 minutes.

(6) Wash cells with PBS three times.

(7) Drain the coverslip, mount it in FluorSave (Calbiochem, San Diego, CA) on a glass slide, and seal the edge with nail polish.

(8) Fluorescence images of the cells were taken with a confocal microscope (Leica, Germany).

For suspended cells, the same procedure was followed except that each of the steps from (1) to (6) was followed by a brief centrifugation.

All the chemicals were purchased from Sigma Chemical, St. Louis, MO, unless otherwise specified.

Chapter 4 Micropipette Aspiration of Fibroblasts – Ramp Tests and Effects of Pipette Size

4.1 Introduction

As reviewed earlier, the micropipette aspiration experiment had been widely used for evaluating the passive mechanical properties of cells, which led to the development of mechanical models based on the spring-dashpot concept (Lim *et al.* 2006). Literature review also reveals the power-law rheology as a promising candidate for modeling the general rheological behavior of cells and in particular, the cytoskeleton (Fabry *et al.* 2001a; Alcaraz *et al.* 2003; Lenormand *et al.* 2004; Yanai *et al.* 2004; Balland *et al.* 2005; Dahl *et al.* 2005; Desprat *et al.* 2005). However, this has not been used to model cells undergoing micropipette aspiration. Thus, it will be necessary to re-examine the creep function of cells with micropipette aspiration and evaluate the applicability of the power-law rheology model.

In order to accurately measure the creep function of cells using micropipette aspiration, three major concerns must be addressed. The first concern regards the consistency and reproducibility of the measurement of cell rheology. Arising from the existence of cytosol (Cunningham 1995), cytoskeleton structures and various organelles, the cell is considerably heterogeneous. It is possible that the cell responds differently to varying pipette sizes. Furthermore, it is possible that when the pipette size gets sufficiently large, the smeared property of the cell can be measured in a more consistent and reproducible way. However, previous micropipette aspiration experiments were usually performed with a relatively fixed pipette size, e.g. ~ 5 μm (Jones *et al.* 1999b; Thoumine *et al.* 1999; Richelme *et al.* 2000), without paying much attention to the effect of pipette size. Thus, the effect of pipette size on cell deformation needs to be studied.

Secondly, the linearity of force-deformation relationship needs to be considered for measuring the creep function. Current calculation of the creep function implied that the elastic-viscoelastic correspondence principle applies for the deformation of the cells during aspiration (Schmid-Schonbein *et al.* 1981; Sato *et al.* 1990; Jones *et al.* 1999b; Dahl *et al.* 2005). However, the applicability of this principle was based on a linear force-deformation relationship (Fung 1965; Flugge 1967). Thus, it would be desirable to examine the linearity of the force-deformation relationship.

Thirdly, the actual deformation of a cell in micropipette aspiration needs to be measured accurately. It is noted that the position of the micropipette entrance is often difficult to locate due to edge effect, which is a result of diffraction, refraction, and reflection of light. Systematic error may result if the pipette edge, as located with edge-detection algorithms, is significantly different from the real location. Thus, the accuracy of deformation measurement needs to be carefully addressed in micropipette aspiration.

NIH 3T3 fibroblasts have been widely used as a model system for studying cell mechanics (Mahaffy *et al.* 2000; Munevar *et al.* 2001; Mahaffy *et al.* 2004; Mizutani *et al.* 2004; Wottawah *et al.* 2005; Fernandez *et al.* 2006). As an adherent cell type, the stiffness of the cell will depend on the degree of prestress (Wang *et al.*

2002; Stamenovic *et al.* 2004; Trepat *et al.* 2004; Fernandez *et al.* 2006). For the purpose of measuring the passive rheological behavior of the cell, detaching and suspending the cells will result in less internal active prestress. Subsequently, the deformability of the cells can be measured in a more consistent manner (Guck *et al.* 2005; Wottawah *et al.* 2005). Therefore, in the current study, the NIH 3T3 fibroblasts were tested in a suspended state.

In this chapter, ramp tests were carried out by increasing the suction pressure on the suspended fibroblasts linearly. The effect of pipette size on cell deformation was investigated by deforming cells with pipettes ranging from 2 to 10 μm in diameter. Through the ramp tests, a suitable range of pipette size was identified for obtaining linear, consistent and reproducible results. The pipette edge effect was indirectly inferred from the ramp tests by estimating the stress-free projection length through extrapolation. Two loading rates, 1/30 and 1/120 cmH_2O/s, was chosen, which provided preliminary information on the viscoelastic properties of the cells. The ramp-test results provided the basis for accurate measurement of the creep function using creep tests and this will be presented in the next chapter.

4.2 Experimental results

Although two loading rates were tested, more consistent results were obtained with the higher loading rate, i.e. 1/30 cmH_2O/s. Thus, the results will be presented based on this loading rate. The effect of slower loading rate will be discussed at the end of this section.

4.2.1 Effect of pipette size on cell deformation

In the ramp tests, at a loading rate of 1/30 cmH_2O/s, the suction pressure on cells was linearly ramped up from 0 to 2 cmH_2O (196 Pa) within 1 min and one image was captured at every 1s interval. Different pipettes, ranging from 2 to 10 μm in diameter, were used. The cells were tested at a temperature of ~ 30°C (it was observed that a temperature that is ~ 2°C higher will cause the cells to spread on the glass substrate, which is undesirable, see Chapter 3 for details). Most fibroblasts assumed approximately rounded shape within a few minutes after detachment. The radius of suspended fibroblasts was 8.8 ± 1.3 μm (mean ± SD, n = 139).

The deformation of the cells were magnified with a microscope and recorded with a digital camera. The deformation of cells in response to aspiration using four different pipette sizes is shown in Fig. 4.1.

For the smallest pipette, the deformation of the cell was usually unnoticeable at small pressure but increased rapidly after a threshold pressure was reached (Fig. 4.1(a1) and (a2)). The protrusion of the cell was often found granule free and detached membrane blebs were sometimes observed (Fig. 4.1(a2)). This may indicate the separation of the membrane from the cytoskeleton, similar to that occurred in blebbing (Cunningham 1995; Hagmann et al. 1999; Charras et al. 2005). With the increase in pipette size, the threshold pressure decreased, the growth of the projection length became steadier and the protrusion was found to be more homogeneous with respect to the outside body in appearance (Fig. 4.1(b), (c) and (d)). It is further noted that for pipettes larger than ~ 6.8 μm, the threshold pressure became relatively insensitive to pipette diameter (Fig. 4.1(c) and (d)).

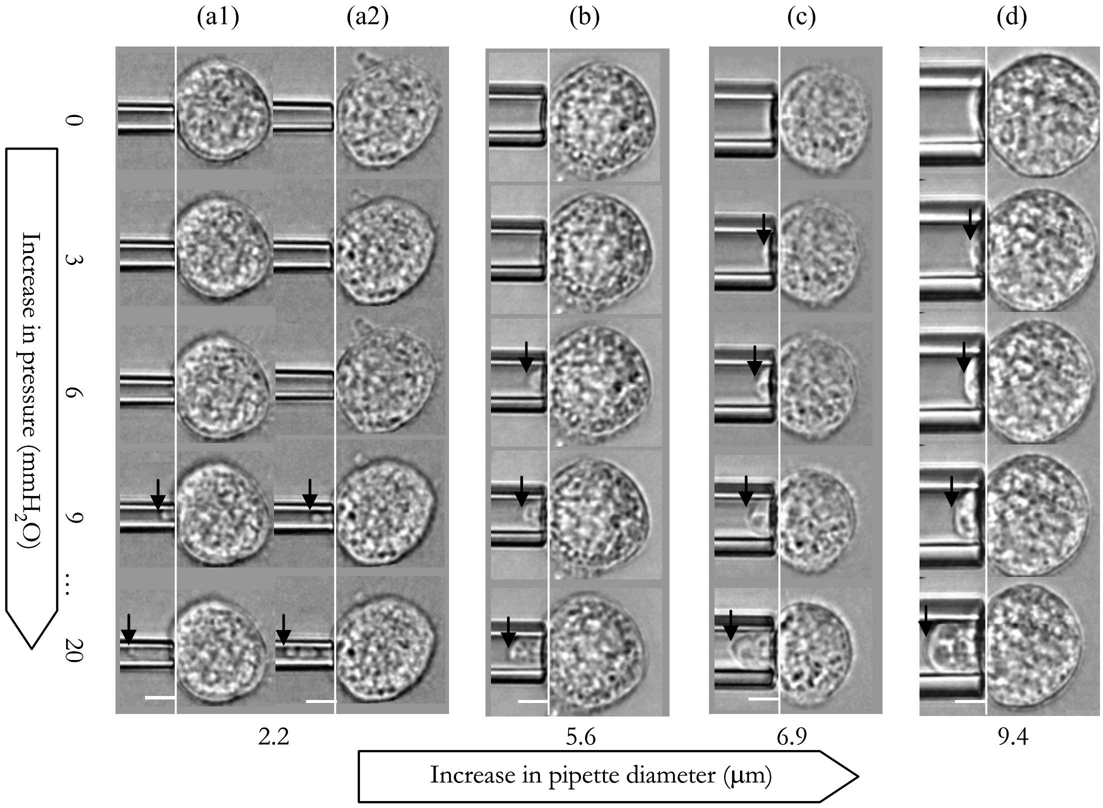
(a1)
(a2)
(b)
(c)
(d)
Increase in pressure (mmH2O)
0
3
6
9
…
20
2.2
5.6
6.9
9.4
Increase in pipette diameter (μm)

Fig. 4.1. Deformation of cells during ramp tests with micropipette aspiration. Results are shown for four pipette sizes: (a1) and (a2) 2.2, (b) 5.6, (c) 6.9 and (d) 9.4 μm. For each pipette size, the deformation was shown for 0, 3, 6, 9 and 20 mmH_2O, from top to bottom (1 mmH_2O = 9.8 Pa). The positions of the pipette entrance and the aperture of the cell protrusion were indicated by the white vertical lines and the black arrows, respectively. (Scale bar in white: 5 μm.)

Deformation of the cell was measured as the total projection length (L_p^T), the distance between the protrusion tip and the pipette entrance (Fig. 4.1). Measured projection length (L_p^T) was plotted against pressure (ΔP) for a small pipette (diameter 3.5 μm) and a large one (diameter 9.4 μm) in Fig. 4.2(a) and (b), respectively. Small protrusions of the cells could not be determined because they were masked by the fussy edge of the micropipette opening (Fig. 4.1, top row), which accounts for the missing data points at very low pressure (Fig. 4.2(a) and (b)).

The linearity and consistency of the ΔP-L_p^T relationship can be evaluated with the square of the Pearson product moment correlation coefficient (R^2), which was plotted against pipette diameter in Fig. 4.2(c).

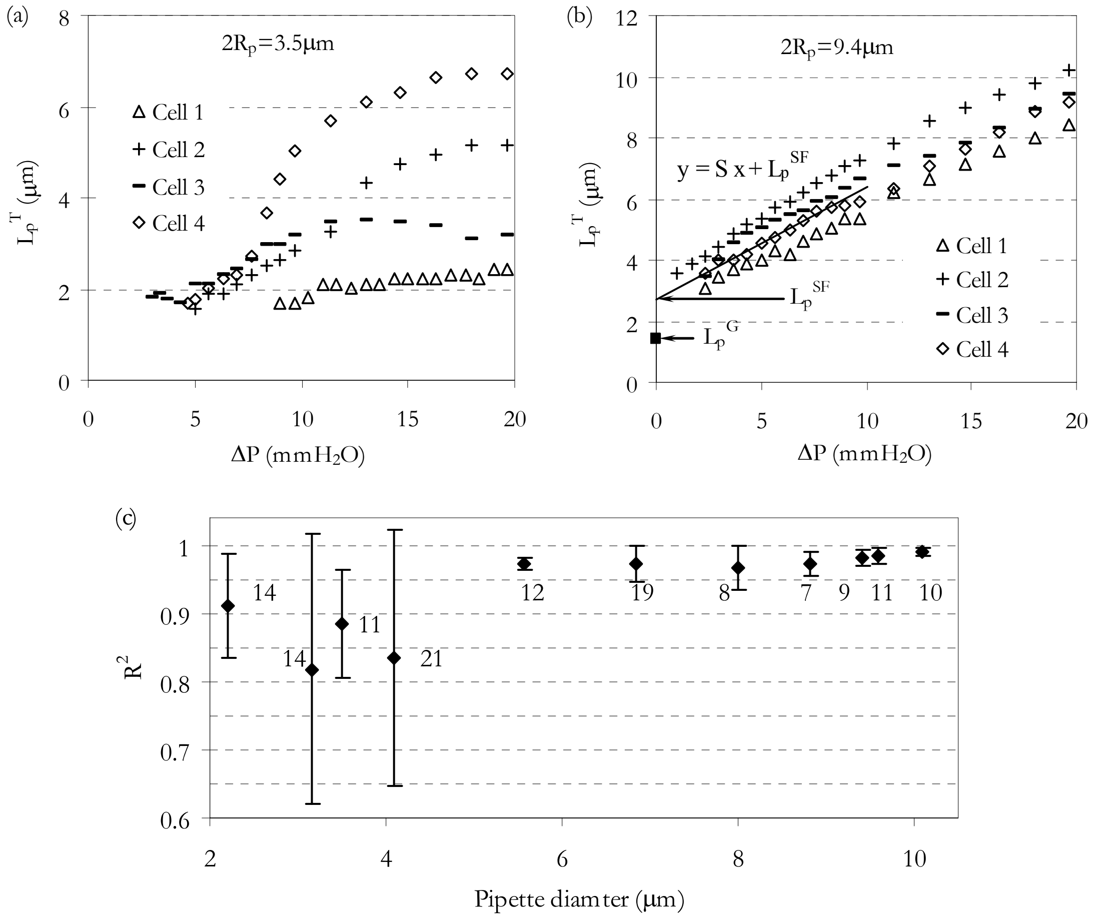

Fig. 4.2. Effect of pipette size on ramp-test results. (a) and (b) Plots showing ΔP-L_p^T relations measured using a small pipette ((a) $2R_p = 3.5$ μm) and a large pipette ((b) $2R_p = 9.4$ μm). The straight line and the equation in (b) represents the average linear fit to the experimental data for $\Delta P = 0 \sim 1$ cmH$_2$O. (c) The dependence of the R^2 on the pipette size. The numbers denote the number of cells tested for the corresponding pipette diameter and the error bars represent standard deviation.

For the small pipette, deformation of the cells was often unnoticeable until a threshold pressure was reached. The deformation was usually irregular and highly variable, and frequently involved blebbing (very fast protrusion) and retraction (Fig. 4.2(a)). Similar observations were made for other pipettes less than ~ 5 μm in diameter (the smallest pipette used was 2.2 μm). The nonlinearity of the measured force-deformation relationship with these small pipettes is also evident from the lower correlation between ΔP and L_p^T (Fig. 4.2(c)).

For the large pipette, the protrusion length increased with pressure in a fairly linear and reproducible manner (Fig. 4.2(b)). Blebbing and retraction were largely absent from cell protrusions into large pipettes. Similar results were obtained for pipettes larger than ~ 5 μm (the largest pipette used was 10.1 μm). The high correlation coefficient further confirms the linearity associated with the large pipettes (Fig. 4.2(c)). Thus, linear curve fitting can be applied to describe the ΔP-L_p^T relation for large pipettes (Fig. 4.2(b)). It is noted that the linear curve fitting was applied to the pressure range of 0 ~ 1 cmH_2O, because the ramp test data within this range showed better linearity. The slope (S) is useful for interpreting the deformability of the cell. The y-intercept can be used to estimate the projection length at the stress free state ($\Delta P = 0$) and is thus referred to as stress-free (SF) projection length (L_p^{SF}).

Nonetheless, it is worth noting that for $2R_p = 5.6$ μm, although the linearity of the measured ΔP-L_p^T relation was high, the deformation was often unnoticeable until the pressure reached ~ 4 mmH_2O (Fig. 4.1(b)), qualitatively similar to the observation with pipettes smaller than 5 μm. Therefore, the 5.6 μm pipette might fall into the transition region between small and large pipettes.

Sato et al. (1987a) and Theret et al. (1988) performed micropipette aspiration of suspended endothelial cells using small pipettes ($2R_p = 2.0 \sim 3.4$ μm). For suspended endothelial cells, the authors did not report any inconsistency and irregularity of cell deformation, given the small pipette size used. This could reflect the difference in the cytoskeleton between the two different cell types. Thoumine and Ott (1997a) performed micropipette aspiration on human dermal fibroblasts with small pipettes ($2R_p = 2.8 \pm 0.4$ μm). The cells exhibited irregular deformation when subjected to a constant pressure. This is qualitatively consistent with the observation made here.

4.2.2 Apparent deformability measured with large pipettes

In order to quantify the mechanical properties of cells, the ramp-test data with large pipettes ($2R_p = 5 \sim 10.1$ μm) were used. The slope, S, of the ΔP-L_p^T relation was quantified as shown in Fig. 4.2(b).

The dependence of S on pipette diameter is presented in Fig. 4.3(a), each data point representing the average of 7 ~ 19 cells. It was found that S approximately increased linearly with pipette diameter larger than 6.8 μm. The slope S was further scaled by pipette radius R_p, which gave a normalized measure of deformability of the cells (Fig. 4.3(b)). It was found that $S/R_p = 0.11 \pm 0.04$ (1/mmH$_2$O) for $2R_p = 5.6$ μm. However, S/R_p remained relatively constant for $2R_p = 6.8 \sim 10.1$ μm, $S/R_p = 0.076 \pm 0.02$ (1/mmH$_2$O). Student's t-test revealed significant difference between the deformability measured by the 5.6 μm pipette and that measured by the larger pipettes ($p < 0.01$); no significant difference was found among the deformability measured by the larger pipettes ($2R_p = 6.8 \sim 10.1$ μm) ($p > 0.3$). This further confirms that the 5.6 μm pipette can be considered as within the transition region for pipette size. For consistency, only the data with $2R_p = 6.8 \sim 10.1$ μm will be used for quantifying the mechanical properties of the cells.

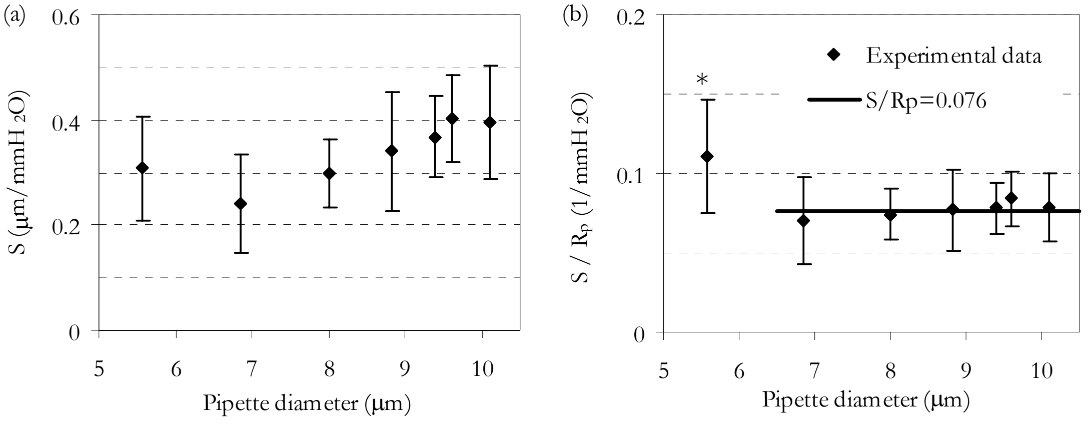

Fig. 4.3. Dependence of measured deformability on pipette size. (a) *S* versus pipette diameter. (b) S/R_p versus pipette diameter. Each point represents the average of 7-19 cells. The symbol (*) in (b) represents significant statistical difference.

The boundary-value problem of micropipette aspiration had been solved analytically using the half-space model (Theret *et al.* 1988) or numerically using the finite element (FE) model (Baaijens *et al.* 2005; Zhou *et al.* 2005a). The elastic half-space model can be written as (Theret *et al.* 1988)

$$\frac{L_p}{R_p} = \frac{\Phi_P}{2\pi}\frac{\Delta P}{G} \approx 0.334\frac{\Delta P}{G} \tag{4.1}$$

where G is the apparent elastic shear modulus and Φ_P is a function of the ratio of the pipette wall thickness to the pipette radius ($\Phi_P \approx 2.1$ for the wide pipettes employed in this study). Note that the deformed projection length L_p can be calculated by subtracting the whole protrusion length with the SF projection length as (cf. Fig. 4.2(b))

$$L_p \equiv L_p^T - L_p^{SF} \tag{4.2}$$

whereby $S = L_p/\Delta P$ for $\Delta P = 0 \sim 1$ cmH$_2$O. The elastic FE model predicted that

$$\frac{L_p}{R_p} = C\frac{\Delta P}{G}$$
$$C = 1.6\left(\frac{R_p}{R_c}\right)^2 - 0.7\frac{R_p}{R_c} + 0.47, \quad \text{for } 0.25 \le \frac{R_p}{R_c} \le 0.60 \tag{4.3}$$

which was derived by applying linear curve fitting to the initial part ($\Delta P/G = 0 \sim 1$) of the FE-simulated force-deformation curves (Zhou *et al.* 2005a) (cf. Section 6.4.1). It is noted that the FE model predicted that C (i.e. the ratio between L_p/R_p and R_p/R_c) will increase mainly because of the slippage between the cell and the pipette, whereas the half-space model did not take the slippage into account. In order to compare the applicability of these two models, the measured relation between S/R_p (i.e. $L_p/(\Delta P\ R_p)$) and R_p is plotted in Fig. 4.4 together with predictions from the half-space model and the FE model.

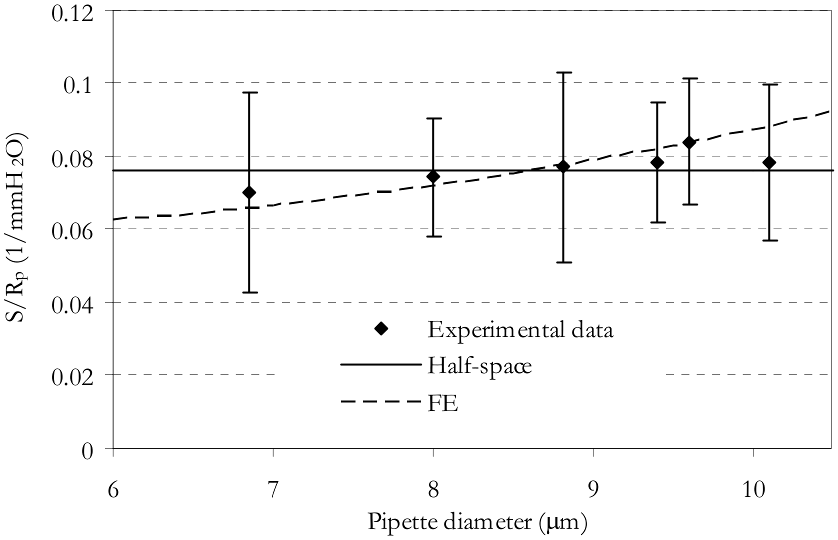

Fig. 4.4. Fitting ramp-test data with half-space model and elastic FE model. The error bars indicate standard deviation.

From Fig. 4.4, it was difficult to compare the applicability of the half-space model with that of the FE model. Using the half-space model, G could be calculated as 47.5 ± 17.3 Pa (mean ± SD, n = 65). In contrast, the FE model predicted G as 73.4

± 26.2 Pa. The ratios of the standard deviation with respect to the mean were the same for the FE model and the half-space model (~ 36%). No dependence was found of the measured elastic modulus on cell radius (the correlation coefficient between the cell radius and the measured G was less than 0.05).

However, the FE model was more accurate in modeling the boundary-value problem of micropipette aspiration because it was not limited by the simplifying assumptions made by the half-space model (such as the half-space and linear-elastic assumptions). Therefore, the FE solution will be preferred for interpreting the micropipette aspiration results.

Few works reported the apparent shear modulus of suspended NIH 3T3 fibroblasts. A recent optical stretcher experiment found the instantaneous shear modulus for this cell type to be 100 ± 10 Pa (Wottawah *et al.* 2005), which is closer to the FE prediction than the half-space prediction.

4.2.3 Stress-free projection length measured with large pipettes

The total projection length of the cell L^T is composed of the SF projection length L_p^{SF} and the deformed projection length L_p (Eq. (4.2)). To identify L_p^{SF}, the most straightforward way is to measure from undeformed cells. Unfortunately, due to the fuzziness of the digital images, the tongue of undeformed cells was difficult to locate (Fig. 4.1). In the ramp tests, however, the linearity of the ΔP-L_p relations indicate that the SF projection length can be estimated from the extrapolation of the ΔP-L_p relations to zero pressure, which corresponds to the undeformed, stress-free state (Fig. 4.2(b)).

L_p^{SF} was found to depend weakly on cell diameter but strongly on pipette diameter for $2R_p = 6.8 \sim 10.1$ μm. The estimated L_p^{SF} is plotted against pipette diameter in Fig. 4.5.

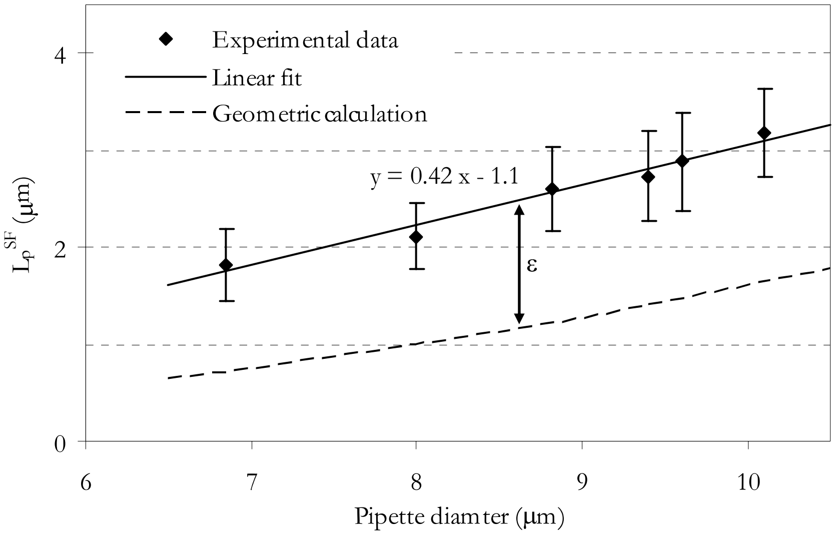

Fig. 4.5. Dependence of the measured stress free projection length on pipette diameter. The measured SF protrusion was found significantly larger than that predicted from geometric calculation (the dash line). ε represents the difference between L_p^{SF} and L_p^{G}.

The average SF projection length can be written as

$$L_p^{SF} = 0.84R_p - 1.1 \tag{4.4}$$

which provides an important reference for calculating the deformed projection length, especially for the ensuing creep experiments. It is noted that because it only depends on the cell diameter and the position of the most distinct edge with respect to the real pipette edge, the SF projection length should not change with the type of measurements or drug treatments.

On the other hand, the SF protrusion length could have been estimated based on geometry as $L_p^G = R_c - \sqrt{R_c^{\ 2} - R_p^{\ 2}}$ (Fig. 4.5), if the most distinct edge, which was used for measuring the total projection length L_p^T (Fig. 4.6), corresponds to the real pipette entrance. However, the linear fits of the measured ΔP-L_p relations usually did not pass through this point (Fig. 4.2(b)) and the experimentally measured L_p^{SF} was significantly larger than L_p^{G} (Fig. 4.5). Furthermore, it is unlikely that the cell undergoes such large deformation (more than 1 μm), given the short time and small pressure. This indicates that the most distinct edge does not correspond to the real pipette entrance, which is illustrated in Fig. 4.6. The distance between the most distinct edge and the real pipette entrance can thus be computed as $\varepsilon = L_p^{SF} - L_p^{G}$, which increases slightly with pipette size but has an average of 1.3 ± 0.4 μm for $2R_p$ = 6.8 ~ 10.1 μm.

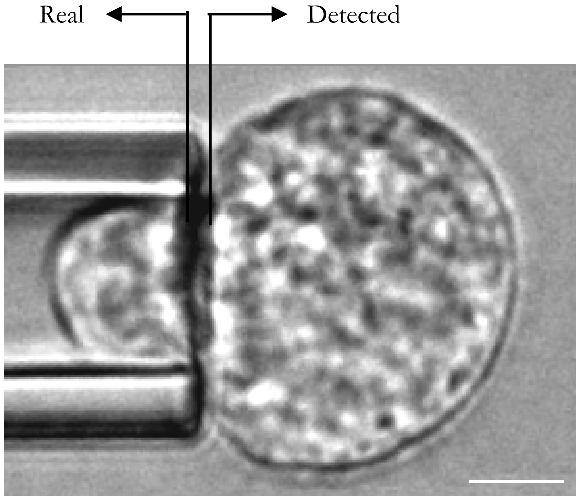

Fig. 4.6. Determination of the pipette entrance location. The detected edge using edge-detection algorithms may not correspond to the real entrance location. (Scale bar in white is 5 μm.)

4.2.4 Ramp-test results for 1/120 cmH$_2$O/s

Similar results were obtained for the effect of pipette size at a slower loading rate, 1/120 cmH$_2$O/s (Fig. 4.7). Therefore, the discussion in Section 4.2.1 also applies to this loading rate.

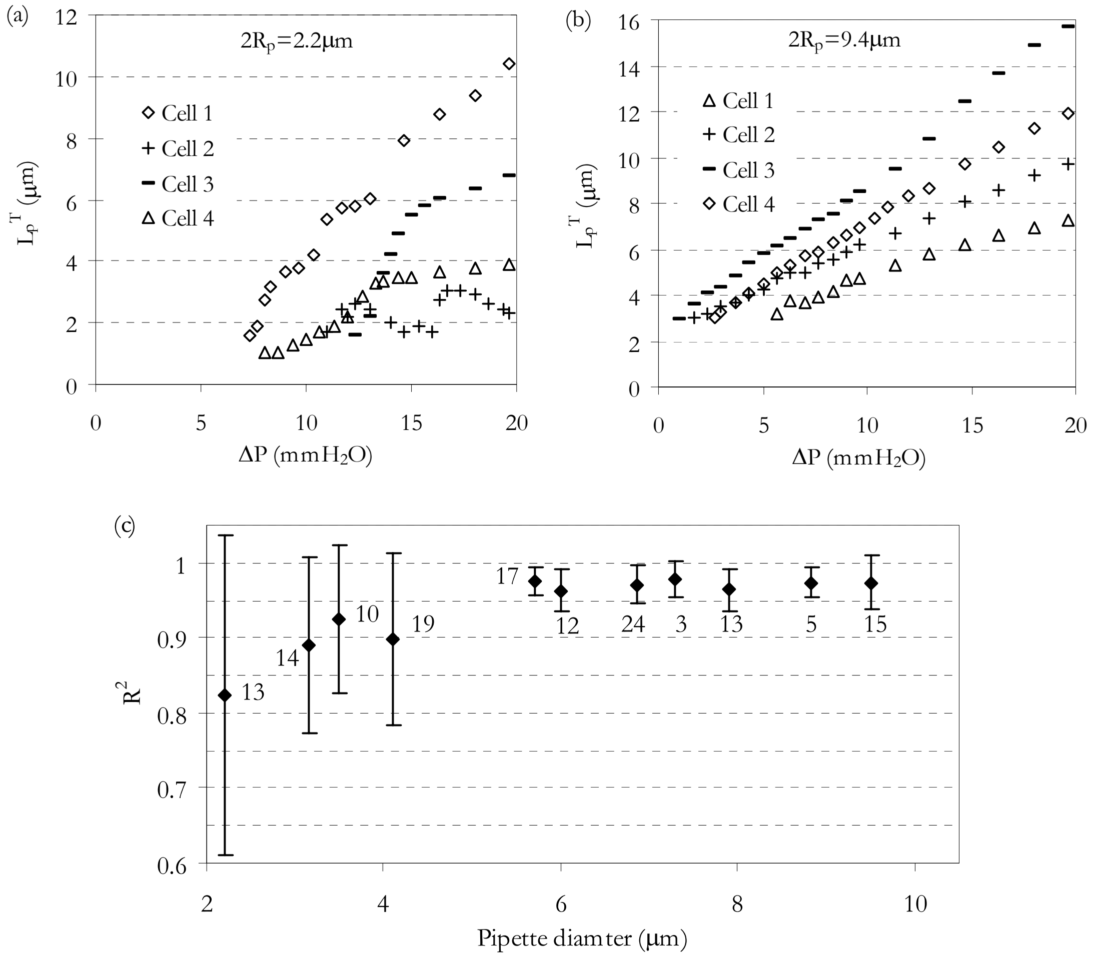

Fig. 4.7. Effect of pipette size on ramp-test results at the loading rate of 1/120 cmH_2O/s. Four representative ΔP-L_p^T plots were shown for (a) a small pipette ($2R_p = 2.2$ μm) and (b) a large pipette ($2R_p = 9.4$ μm), respectively. (c) The dependence of the R^2 on the pipette size. The numbers denote the number of cells tested for the corresponding pipette diameter.

When linear curve fitting was applied to the ramp-test data ($\Delta P = 0 \sim 1$ cmH_2O) for relatively large pipettes ($2R_p = 5 \sim 9.6$ μm), the measured deformability was found to become relatively constant for pipettes larger than ~ 7 μm (Fig. 4.8). For $2R_p = 7.3 \sim 9.56$ μm, S/R_p was measured as 0.105 ± 0.04 (1/mmH_2O). G was calculated as 36.5 ± 15.2 Pa (mean ± SD, n = 36) with the half-space model, whereas the elastic FE model predicted $G = 55.4 \pm 24.6$ Pa. The deformability measured with 1/120 cmH_2O/s was significantly higher than that measured with 1/30

cmH_2O/s ($p < 0.01$); the elastic shear modulus measured with 1/120 cmH_2O/s was significantly lower than that measured with 1/30 cmH_2O/s ($p < 0.01$). This is due to the viscoelastic properties of the cell, which will be more accurately quantified with creep tests (cf. Chapter 5).

The ratios of the standard deviation with respect to the mean were 44% if the FE model is used or 42% if the half-space model is used, both of which were larger than those obtained with the higher loading rate (36%). This indicates that the lower loading rate induces less consistent deformation of the cells. In addition, the efficiency of testing was lower with 1/120 cmH_2O/s, because the testing of each single cell will take longer time than with 1/30 cmH_2O/s. Therefore, the higher loading rate is preferred for improved efficiency and consistency of testing.

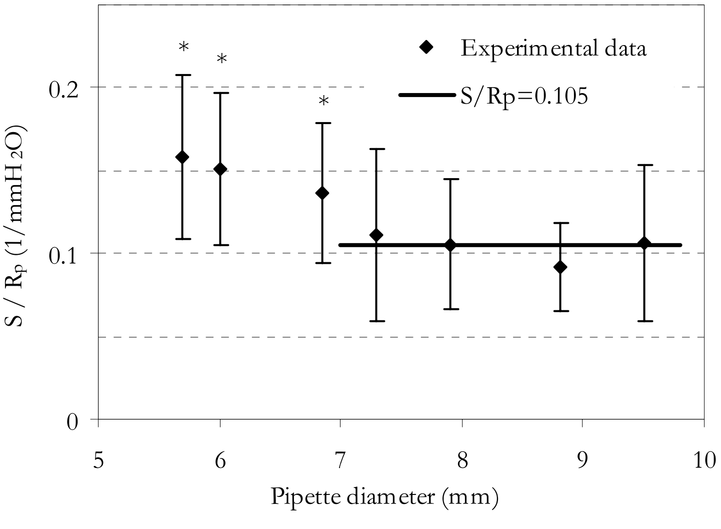

Fig. 4.8. Dependence of measured deformability on pipette size at the loading rate of 1/120 cmH_2O/s. The symbols (*) represent significant statistical difference against the deformability measured with $2R_p = 7.3 \sim 9.56$ μm.

For $2R_p = 7.3 \sim 9.56$ μm, the SF projection length at 1/120 cmH_2O/s was found slightly lower than that measured with the higher loading rate. This is expected because of the viscoelastic properties of the cells. Although the loading rates we have tested included only 1/120 and 1/30 cmH_2O/s, theoretical analysis shows that the SF projection length will only slightly increase with loading rate and soon reach a plateau when the loading rate gets sufficiently fast (cf. Section 5.3.2).

4.3 Discussion

4.3.1 Blebbing and nonlinear deformation preferentially occur with smaller pipettes

The effect of pipette size on the pressure-deformation relationship of suspended fibroblasts has been examined. It was found that pipettes with diameter smaller than ~ 5 μm generated nonlinear results which are not reproducible (Fig. 4.2(a) and Fig. 4.7(a)). More interestingly, given the same suction pressure, cell blebbing was found to occur more frequently with smaller pipettes but seldom with larger ones (Fig. 4.1). It is known that cell blebbing is a result of rupture between plasma membrane and underlying cytoskeleton and subsequent intracellular solvent flow (Cunningham 1995; Hagmann et al. 1999; Charras et al. 2005) and that blebbing can be induced by micropipette aspiration using hydrostatic suction pressure (Rentsch and Keller 2000). The results reported here therefore suggest that, at the same suction pressure, smaller pipettes are more likely to cause detachment between plasma membrane and cytoskeleton. The molecular mechanism that underlies the pipette-size effect on blebbing remains to be explored.

The observed nonlinearity and inconsistency in the pressure-deformation relationship with small pipettes may be attributed to four reasons. It may firstly be attributed to cell blebbing as mentioned above. Secondly, the large difference among individual measurements might reflect the heterogeneity of the cell cortex. A smaller pipette will measure the average property over a smaller area and therefore, will show larger scattering than that measured by larger pipettes. Thirdly, the nonlinearity in a single experiment may be due to the heterogeneity of the cytoplasm, especially the coexistence of cytosol and the relatively rigid organelles and cytoskeleton (CSK) structures with different sizes and shapes (Bausch *et al.* 1999). These CSK structures and organelles may only be “felt” by pipettes that are smaller than or comparable to them in size. The intermittent entrance of cytosol and CSK structures/organelles might be responsible for the observed nonlinearity in Fig. 4.2(a) and Fig. 4.7(a). Lastly, it is possible that the active force generation of the cells is comparatively more evident in smaller pipettes than in larger ones. If we assume that the active force generation (for example through actin-myosin interaction) is only in the cortex of the cell (Albrecht-Buehler 1987; Schmid-Schonbein *et al.* 1995), then the total amount of active force is proportional to the circumference of the cell projection, which is proportional to R_p, whereas the suction force is proportional to R_p^2. Therefore, with the reduction in pipette diameter, the suction force will decrease faster than the active force. When the active force becomes comparable to the suction force, active motion of the cell may become prominent enough to lead to retraction, which was sometimes observed to occur with small pipettes but seldom in larger ones (Fig. 4.2 and Fig. 4.7).

4.3.2 Larger pipettes are more suitable for probing smeared mechanical properties of cells

The ramp tests with different pipette sizes also revealed that coherent deformation of cells could generally be induced with large pipettes, judging by the homogeneous appearance of cell protrusion with respect to the outside cell body (Fig. 4.1(c) and (d)). The pressure-deformation relationships were linear and reproducible when the cells were probed with pipettes larger than ~ 5 μm (Fig. 4.2(b) and Fig. 4.7(b)). We attribute the linearity and reproducibility to the following reasons. First of all, blebbing is less likely to occur with large pipettes. Secondly, the large pipettes are probing the smeared property of a large portion of the cell. Finally, the active force of the cell might be relatively negligible in comparison to the total suction force.

However, the measured deformability S/R_p was found to be not constant for pipettes larger than 5 μm. The deformability measured was higher with the smaller pipettes and reached a plateau for pipettes larger than ~ 7 μm (Fig. 4.3(b) and Fig. 4.8). On the other hand, the apparent deformability of the cell (S/R_p) was predicted not to decrease with increasing pipette size when the cell was modeled as a homogeneous solid (Theret *et al.* 1988; Haider and Guilak 2002; Baaijens *et al.* 2005; Zhou *et al.* 2005a). The discrepancy between theoretical prediction and experimental results might be because that partial detachment between cell membrane and cytoskeleton, which is accompanied by inflation of intracellular cytosol (Charras *et al.* 2005), can still considerably occur for pipettes with diameter between 5 and 7 μm.

In view of the above, it is recommended that larger pipettes be adopted for the purpose of measuring the bulk rheology of the cells in a consistent and reproducible manner with micropipette aspiration.

4.3.3 Rate dependence of measured deformability

The deformability of suspended NIH 3T3 fibroblasts was measured to be relatively constant for pipettes larger than ~ 7 μm in the ramp tests (Fig. 4.3(b) and Fig. 4.8). The measured properties of the cells are shown in Table 4.1. It was found that the measured mechanical properties depended on the loading rate, which is a manifestation of the viscoelasticity of the cell. Nonetheless, a complete description of the viscoelastic properties cannot be derived from the ramp tests with limited number of loading rates, although the ramp-test results will serve to validate proposed viscoelastic models (cf. Chapters 5 and 6). More accurate characterization of the viscoelasticity will be achieved using creep tests, which will be presented in Chapter 5.

Table 4.1. Measured mechanical properties of cells with ramp tests using large pipettes

Loading rate (cmH_2O/s)	S/R_p ($1/mmH_2O$)	Apparent elastic shear modulus G (Pa)		Number of cells tested
		Half-space model	FE model	
1/30	0.076 ± 0.02	47.5 ± 17.3	73.4 ± 26.2	65
1/120	0.105 ± 0.04	36.5 ± 15.2	55.4 ± 24.6	36

4.3.4 Calculation of deformed projection length

Due to the edge effect of the glass pipette, the location of the pipette entrance may not correspond to the most distinct edge derived through image analysis using edge-detection algorithms. In ramp tests, the SF projection length was derived through extrapolation of the ΔP-L_p relations to zero pressure (Eq. (4.4)) and found significantly larger than the prediction based on geometrical calculation assuming the most distinct edge as the real pipette entrance. This suggested that real pipette edge might be away from the detected edge by 1.3 ± 0.4 μm for the large pipettes

($2R_p = 6.8 \sim 10.1$ μm) in the current study (Fig. 4.5). It is noted that the edge effect might differ with the pipette wall thickness and the imaging system (including the microscope and digital camera). It is possible that the edge effect will be less significant with thinner pipette wall, higher magnification and/or higher numerical aperture.

The edge effect must be taken into consideration for accurate measurement of the deformed projection length. Although the absolute value of the deformed projection length appears to be not so important for ramp tests (the apparent deformability is only sensitive to the slope of the ΔP-L_p relation), it has significant influence on the creep function measured with micropipette aspiration (cf. Chapter 5).

In principle, the SF projection length should only depend on the cell diameter and the position of the most distinct edge with respect to the real pipette edge. Thus it should not change with the type of measurements or drug treatments. As such, Eq. (4.2) and Eq. (4.4) will be used to calculate the deformed projection length of cells in the creep tests in Chapter 5.

4.3.5 On approximate applicability of linear viscoelasticity to cells

The measurement of creep function from creep experiments depends on the extent to which linear viscoelasticity applies to deformation of cells, especially when large deformation is involved. The approximate applicability of linear viscoelasticity is firstly supported by the linear force-deformation relationship while performing ramp experiments (or other pseudo-elastic ones). Approximately linear force-deformation relationship have been observed with the tensile tester for fibroblasts (Miyazaki *et al.* 2000), microplate manipulation for fibroblasts (Thoumine and Ott 1997b), micropipette aspiration for chondrocytes (Jones *et al.* 1999b) and endothelial cells (Theret *et al.* 1988). Similarly, the current ramp tests with micropipette aspiration revealed significant linearity of the force-deformation relationship for fibroblasts for pressure up to 200 Pa, when large pipettes were employed.

The second evidence for the approximate applicability of linear viscoelasticity lies in the independence on magnitude of stress of the measured mechanical moduli. In OMTC experiment, the measured dynamic moduli of human airway smooth muscle cells (HASM) were found to be independent of load when the specific torque varied from 1.8 Pa to 130 Pa (Fabry *et al.* 2003). In microplate manipulation experiment, the dynamic moduli of fibroblasts were found to be constant when stress is below ~ 1 kPa (Fernandez *et al.* 2006). It is worth noting that power-law stress stiffening, with exponent ~ 1, was observed for higher stress with fibroblasts (Fernandez *et al.* 2006), which indicate that linear viscoelasticity becomes inapplicable for stress above ~ 1 kPa.

The third support is provided by creep experiments. The creep experiment using microplate manipulation (Desprat *et al.* 2005), which measured large-strain creep function of cells, predicted power-law behavior with viscoelastic parameters comparable to those measured by small-strain experiments such as the OMTC (Fabry *et al.* 2001a). Desprat et al. (2005) also showed that the measured creep function were not affected by the magnitude of stress (3 ~ 180 Pa) and proposed that the cells remained in the linear viscoelastic regime for engineering strain up to 1.

Lenormand *et al.* (2004) performed both creep experiments and dynamic experiments on HASM cells using OMTC. Consistent results were obtained between the two measurements, which is consistent with linear viscoelasticity.

The experimental results presented above suggest that linear viscoelasticity can approximately describe the mechanical properties of cells at moderately large stress and strain. In the context of linear viscoelasticity, the elastic-viscoelastic correspondence principle (Flugge 1967) and the half-space model (Theret *et al.* 1988) can be used to estimate the creep function of cells in creep tests using micropipette aspiration, which will be presented in the Chapter 5.

Finite element analysis of the experiments will be reported in Chapter 6, which provides better understanding of large deformation of cells in micropipette aspiration.

Chapter 5 Micropipette Aspiration of Fibroblasts – Creep Tests and Power-law Behavior

5.1 Introduction

As reviewed in Chapter 2, the viscoelasticity of a cell is intimately involved in its structural integrity, locomotion and deformability. The wide application of micropipette aspiration has generally led to the development of continuum models based on the spring-dashpot concept, such as the cortical shell-liquid core models (Dong *et al.* 1988; Yeung and Evans 1989; Needham and Hochmuth 1990; Tsai *et al.* 1993) and the standard linear solid model (Schmid-Schonbein *et al.* 1981; Sato *et al.* 1990; Jones *et al.* 1999b; Guilak *et al.* 2000; Koay *et al.* 2003). With the advancement in experimental techniques, the complex moduli and the creep function of cells can be measured with greater accuracy than before. Using oscillatory magnetic twisting cytometry (OMTC), Fabry *et al.* (2001a; 2003) found that the dependence of complex mechanical moduli on frequency could be fitted by the power-law rheology model for a wide range of adherent cell types (cf. Table A.3). Subsequently, this model has been confirmed for more adherent cell types using at least five experimental techniques, in both frequency domain and time domain (Fabry *et al.* 2001a; Alcaraz *et al.* 2003; Lenormand *et al.* 2004; Yanai *et al.* 2004; Balland *et al.* 2005; Dahl *et al.* 2005; Desprat *et al.* 2005).

As evidence in support of the power-law model accumulates, this model has not been confirmed with micropipette aspiration experiment for cells (Evans and Kukan 1984; Needham and Hochmuth 1990; Jones *et al.* 1999b; Thoumine *et al.*

1999), although it has been shown valid for nuclei using this technique (Dahl *et al.* 2005). Therefore, it would be necessary to re-examine the creep function of cells in response to micropipette aspiration. Furthermore, all the experiments that supported the power-law model for whole cells were on cells adherent to the substrate (even in the microplate manipulation, the cells were allowed to adhere to the glass microplates firmly before testing). The applicability of the power-law rheology model to suspended cells has not been established. The optical stretching of suspended NIH 3T3 fibroblasts suggested that the power-law rheology model is not applicable (Wottawah *et al.* 2005). However, there is still one major concern on this conclusion. The effect of laser heating (Peterman *et al.* 2003), which may cause denaturation of proteins and alteration in rheological properties, has not been quantified for optical stretcher. Thus, performing micropipette aspiration of suspended cells will further clarify the rheology of suspended cells.

The previous chapter established that linear and coherent deformation of cells can be more reproducibly obtained with larger pipettes. The stress-free projection length has also been quantified as a function of pipette size. In this chapter, creep tests will be performed with large pipettes on suspended cells. Based on measured creep function, the applicability of different rheological models, including the spring-dashpot models and the power-law rheology model, are evaluated. In addition, the effect of drug treatments on the mechanical properties of cells is investigated to understand the relative contribution of actin filaments and microtubules. In particular, the hypothesis that high concentration of microtubule-disrupting drugs can lead to activation and stiffening of cells will be tested.

5.2 Experimental results

Ramp tests revealed that larger pipettes are needed to produce more consistent deformation of cells and that the pressure-deformation relationship is fairly linear for pressure up to 2 cmH$_2$O. Thus, creep tests were done on suspended fibroblasts using large pipettes ($2R_p = 7.4 \sim 10.1$ μm) at a step pressure of 1 cmH$_2$O (98 Pa). The creep behavior of untreated cells was presented first, followed by the creep behavior of cells treated by two cytoskeleton disrupting drugs, cytochalasin D (cytoD) and colchicine.

5.2.1 Creep behavior of untreated fibroblasts

In Fig. 5.1(a), the creep deformation of several fibroblasts in response to a step pressure was shown. Upon application of the suction pressure, the deformation of the cells was usually fast at the beginning and gradually decelerated with time. The deformation of the fibroblasts usually would not stabilize within typical time scale of creep experiments. Similarly, Thoumine et al. (1999) found that the deformation of fibroblasts would not stop even after ten minutes of loading, unlike what was reported for chondrocytes (Jones *et al.* 1999b) or endothelial cells (Sato *et al.* 1996) undergoing micropipette aspiration. This difference might be attributable to different cells types, with chondrocytes and endothelial cells being more elastic than fibroblasts in suspension.

The stress-free projection length is needed for quantifying the actual deformation of cells. Due to the pipette edge effect, the stress-free projection length, L_p^{SF}, is larger than that predicted with geometric calculation, L_p^G (Fig. 5.1(a)) (cf. Section 4.2.3). Thus, the deformed projection length of the cell was computed as L_p

$= L_p^T - L_p^{SF}$ (cf. Fig. 5.1(a)). L_p^{SF} was taken as that measured with ramp tests (Eq. 4.4). Deformed projection length for the four cells in Fig. 5.1(a) was plotted against time in log-log scale in Fig. 5.1(b), where linearity can be observed over two decades of time for individual cells.

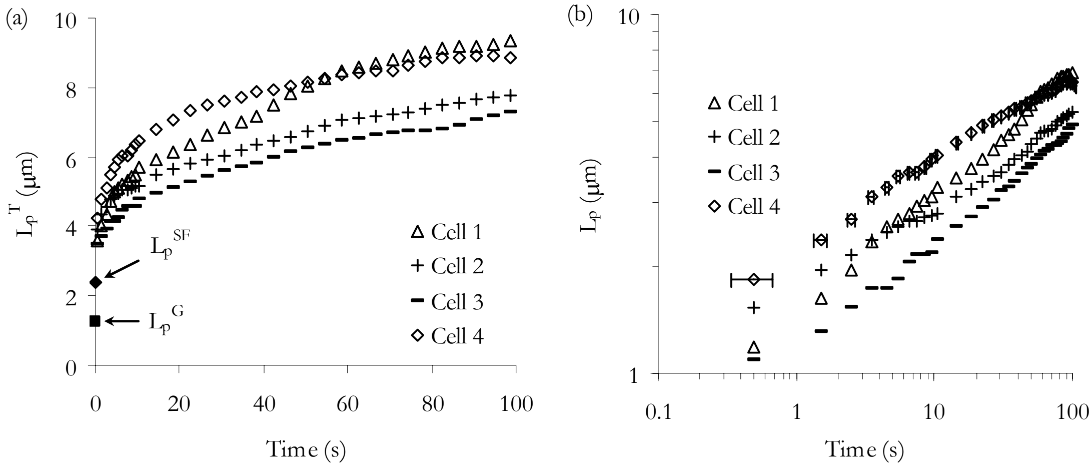

Fig. 5.1. The creep deformation of several fibroblasts measured by micropipette aspiration. (a) The total projection length was plotted against time in linear scale. L_p^G and L_p^{SF} are explained in the text. (b) The actual deformation was plotted against time in log-log scale. The pipette diameter was 9.1 microns and the step pressure was 1 cmH_2O.

Note that the time for the first deformation measurement was assumed to be at 0.5 s and the error bars correspond to a nominal standard deviation of 0.17 s in time (Fig. 5.1(b)) (cf. Section 3.1.5). Improvement of time resolution can be achieved using a camera with higher speed in the future.

5.2.1.1 Interpretation and modeling of creep function

Based on the discussion in Section 4.3.5, the creep function of cells can be estimated based on the half-space model (Theret *et al.* 1988) and the elastic-viscoelastic correspondence principle (Flugge 1967). The shear creep function $J(t)$ can be derived as (see Appendix B.5)

$$J(t) = \frac{2\pi}{\Phi_p R_p} \frac{L_p(t)}{\Delta P} \tag{5.1}$$

which is more general than the SLS half-space solution (Sato *et al.* 1990) and same as that employed by Dahl et al. (2005). A total of 81 untreated fibroblasts were tested using pipettes with diameters ranging from 7.4 to 10.1 μm. Average creep function was computed for all the cells and presented in Fig. 5.2.

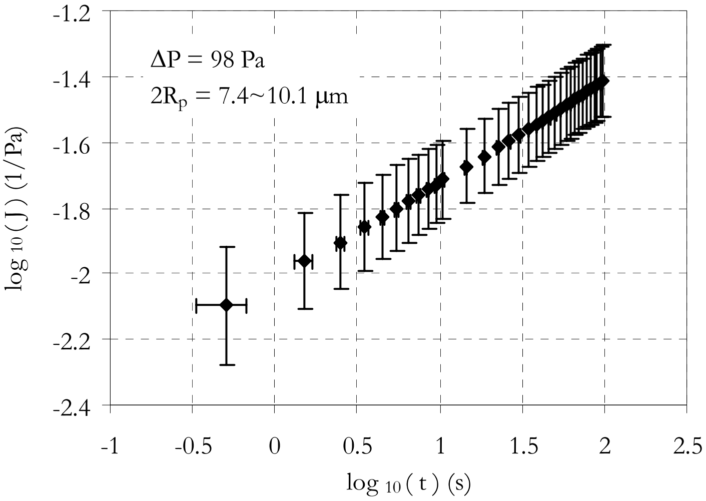

Fig. 5.2. Average creep function of 81 suspended fibroblasts plotted in log-log scale. (Error bars are standard deviation.)

In order to model the creep function, three viscoelastic models were considered: the power-law rheology model (Eq. (2.21)), the standard linear solid (SLS) model (Eq. (2.15)) and the standard linear solid-dashpot (SLS-D) model (Eq. (2.17)). Least-squares method was used to achieve the curve fitting and the coefficient of determination (R^2) was used to assess the goodness of fit (Fig. 5.3). It was found that the power-law rheology model could best fit the creep function, as shown by the highest R^2 value, despite the fact that it has the fewest free parameters. The SLS model and the SLS-D model performed reasonably well within 1 ~ 2 time decades but will deviate for shorter or longer time scales. This observation is qualitatively similar to the creep experiments done using other techniques, including micropipette aspiration of nuclei, magnetic bead twisting, optical trap pulling of intracellular organelles and microplates pulling (Lenormand *et al.* 2004; Yanai *et al.* 2004; Dahl *et al.* 2005; Desprat *et al.* 2005).

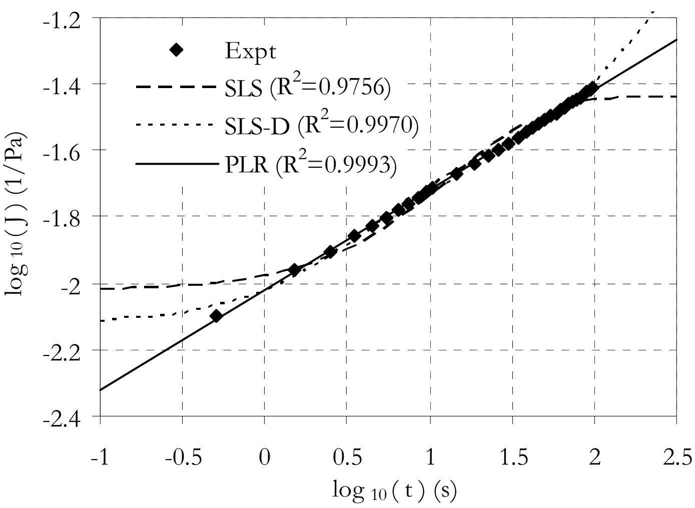

Fig. 5.3. Fitting the average creep function of suspended fibroblasts by the power-law rheology (PLR) model, SLS model and SLS-D model.

Therefore, the mechanical properties of the cells can be interpreted based on the power-law rheology model (Eq. (2.24)), which is rewritten here for convenience

$$J(t) = A_J t^{\alpha} \tag{5.2}$$

where A_J (Pa^{-1}) is the shear compliance constant reflecting the deformability of the cell (note that $A_J = J(1\ \text{s})$) and α is the power-law exponent ($0 < \alpha < 1$). Smaller α will indicate a more elastic behavior whereas a larger α indicates a more fluidic behavior (Fabry *et al.* 2001a). From the creep function, the corresponding complex modulus and relaxation modulus can respectively be derived as (Desprat *et al.* 2005) (cf. Appendix B.4)

$$G^*(\omega) = A_G(i\omega)^\alpha = \frac{1}{A_J\Gamma(1+\alpha)}(i\omega)^\alpha \tag{5.3}$$

and

$$G(t) = G(1)t^{-\alpha} = \frac{A_G}{\Gamma(1-\alpha)}t^{-\alpha}. \tag{5.4}$$

A_G (Pa) is the shear stiffness constant ($A_G = 1/[A_J\,\Gamma(1+\alpha)]$) and $\omega = 2\pi f$, f being the frequency (in Hz). A_G corresponds to the magnitude of complex modulus at $\omega = 1$ rad/s, $|G^*(1\text{ rad/s})|$; $G(1) = A_G/\Gamma(1-\alpha)$ equals the relaxation modulus at $t = 1$ s. Based on the relations above, α, A_J and A_G can then be interpreted from the measured creep function of suspended fibroblasts.

5.2.1.2 Statistical distribution of the power-law parameters

The distribution of α, A_J and A_G are plotted in Fig. 5.4. The distribution of the exponent α is best fitted with the normal distribution with $\alpha = 0.30 \pm 0.05$ (mean ± SD, 81 cells) (Fig. 5.4(a)). The power-law exponent reported here for suspended NIH 3T3 fibroblasts is comparable to that measured for nuclei using micropipette aspiration (Dahl *et al.* 2005) but generally higher than those measured with cells attached to substrate using other techniques (Table A.3). It is noted that the standard deviation is generally smaller than those found for attached cells. For example, Fabry et al. (2003) reported SD ≈ 0.06 using OMTC and Desprat et al. (2005) reported SD = 0.08 using microplate manipulation.

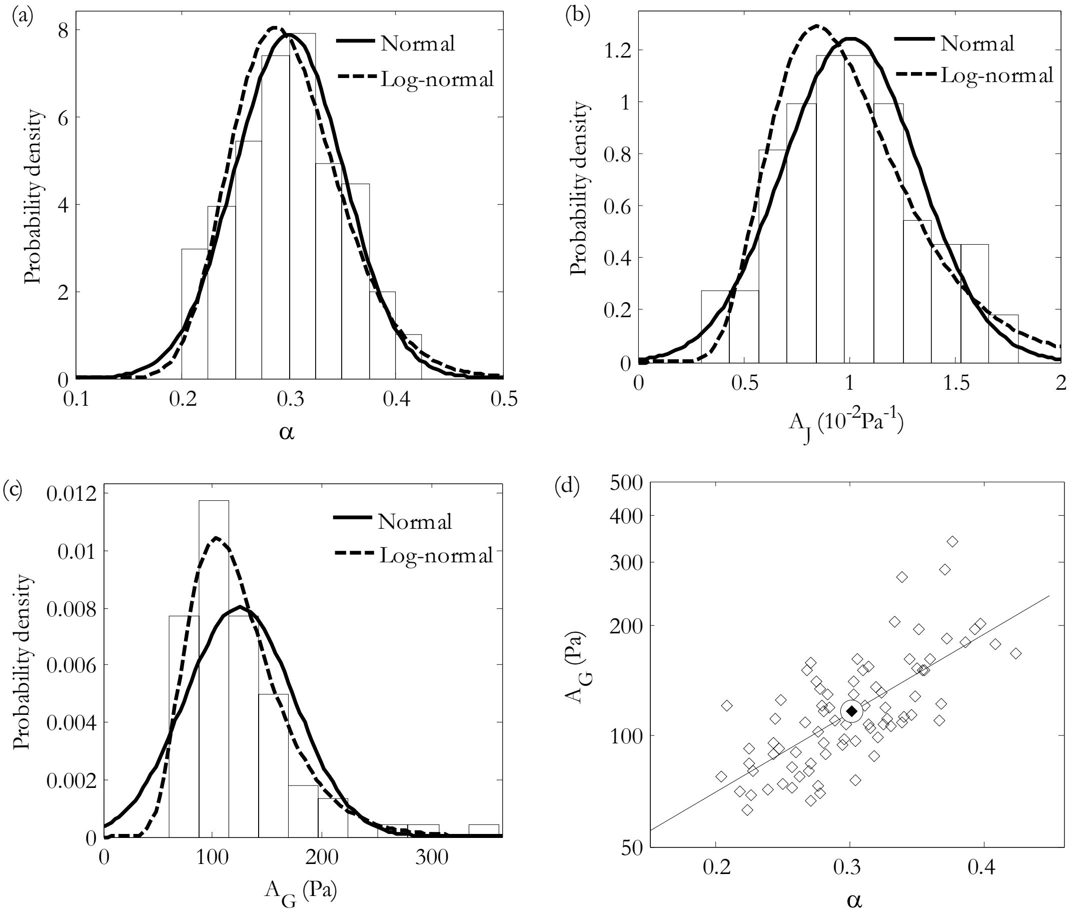

Fig. 5.4. Statistical distribution of the power-law rheology parameters. (a)–(c) Probability density for the distribution of (a) power-law exponent, (b) shear compliance and (c) shear stiffness measured for untreated fibroblasts (n = 81). The best fits of normal and log-normal distribution functions were also shown. (d) Correlation between A_G and α.

The distribution of A_J is slightly better fitted by a normal distribution than by a log-normal distribution (Fig. 5.4(b)). The normal distribution will predict $A_J = 1.0 \pm 0.3$ (10^{-2} Pa^{-1}) (mean ± SD) whereas the log-normal one will predict a geometric mean of $<A_J> = 0.95$ (10^{-2} Pa^{-1}) and a geometric standard deviation of 1.41. Finally, the distribution of A_G is more faithfully fitted by a log-normal distribution, with geometric mean of $<A_G> = 116.6$ Pa and a geometric standard deviation of 1.36 (Fig. 5.4(c)). The average stiffness as well as the variation of the data reported here are generally less than those reported for attached cells using other techniques (Table A.3).

Interestingly, A_G and α seem to be positively correlated with each other (Fig. 5.4(d)). The correlation coefficient between $\log_{10}(A_G)$ and α is 0.50 and the data could be approximately fitted with $A_G = 26 \times 0.007^{\alpha}$ Pa (the straight line in Fig. 5.4(d)). This suggests that individual cells which are stiffer (larger A_G) tend to be more fluidic (higher α) and vice versa. This is similar to the observations made with OMTC (Fabry *et al.* 2003).

5.2.1.3 Effect of pipette size on creep function

In order to examine the dependence of the measured creep function on pipette size, the compliance constant (A_J) and the power-law exponent (α) are plotted against pipette diameter in Fig. 5.5. The t-test performed revealed no significant difference among A_J or α measured by different pipette sizes, which is consistent with the results from ramp tests, where the deformability was found constant over the range of $2R_p = 7 \sim 10.1$ μm (cf. Fig. 4.4 and Fig. 4.8). Similar conclusion can also be made for the stiffness constant A_G (A_G is approximately the reciprocal of A_J). This further substantiates the consistency and reproducibility of cell deformation associated with large pipettes.

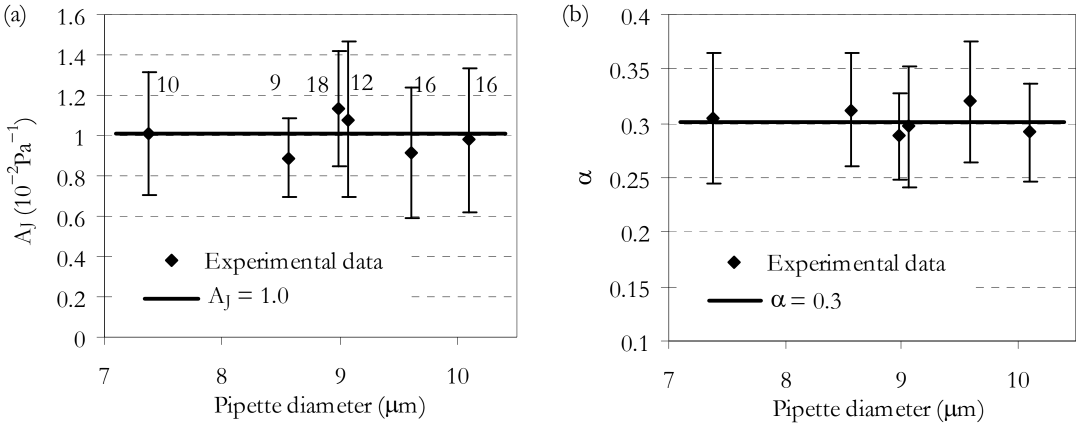

Fig. 5.5. Effect of pipette size on the measured creep function. Neither A_J (a) nor α (b) is affected by the pipette size. The numbers above the experimental data points in (a) denote the sample size measured for each pipette size.

5.2.2 Effect of drug treatments

In order to understand the roles of actin filaments and microtubules in cell rheology, the effect of cytoD and colchicine on the mechanical properties of cells were investigated using the methods described in Chapter 3. After 30 minutes of treatment in the culture dish, DMSO (solvent for delivering cytoD) caused no observable change to the cell morphology. CytoD (2 μM) usually caused the cells to appear relaxed and to detach from the substrate. Colchicine at 1 mM caused cells to loss their elongated shape and polarity. Active small swelling could be seen on the surface of some cells, similar to that observed for IAR-2 liver epithelial cells treated with nocodazole, which also depolymerizes microtubules (Omelchenko *et al.* 2002). The effect of 100 μM colchicine is similar to but less pronounced than that of 1 mM colchicine.

The creep deformation of drug-treated cells in comparison with untreated cells during micropipette aspiration is shown in Fig. 5.6. It is noted that while disruption of actin filaments by cytoD consistently led to significantly larger deformation (cf. Fig. 5.6(a) and (c)), the effect of microtubule disruption by high dosage of colchicine is less consistent. Some colchicine-treated cells exhibited passive deformation similar to that of untreated cells (Fig. 5.6(d1)), but some showed active protrusions and retractions and deformed very little into the micropipette (Fig. 5.6(d2)).

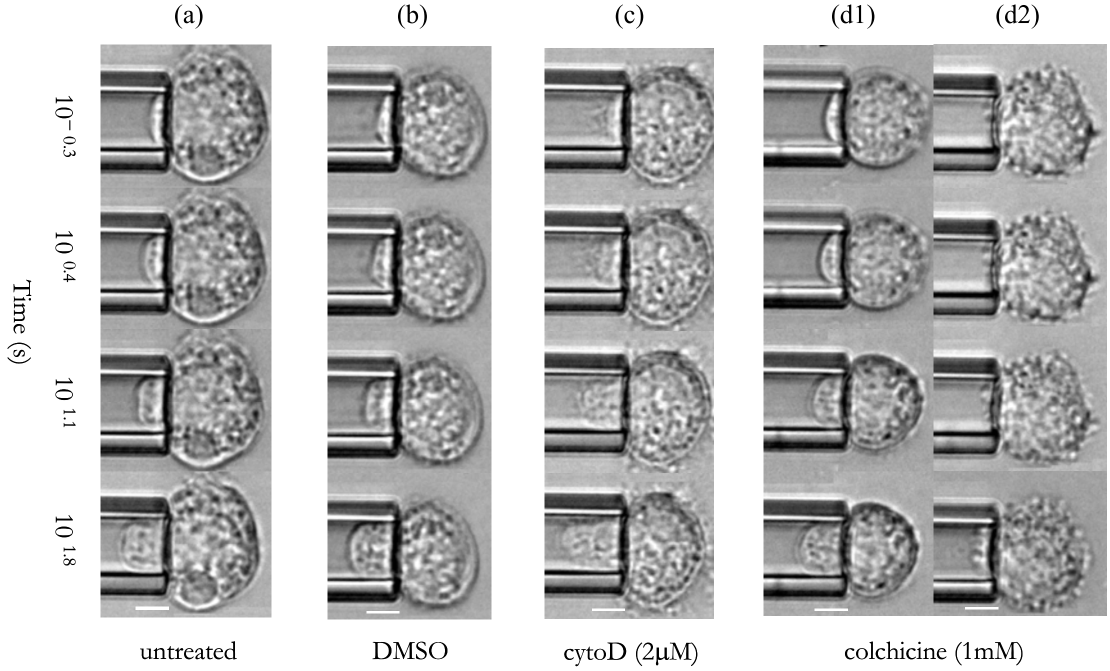

Fig. 5.6. Effect of drug treatments on cell deformation during creep experiments. (a) An untreated cell, (b) a cell treated by DMSO (0.1%), (c) a cell treated by 2 μM cytoD, and (d1) and (d2) two cells treated with 1 mM colchicine. For each cell, deformation was shown for $t = 0.5$ (~ $10^{-0.3}$), 2.5 (~ $10^{0.4}$), 12.5 (~ $10^{1.1}$) and 62.5 (~ $10^{1.8}$) s. The pipette size was 9 μm and pressure was 98 Pa. (Scale bar: 5 μm.)

The average creep functions measured for drug-treated cells are plotted together with those for untreated cells and DMSO-treated cells in Fig. 5.7. It was found that the power-law rheology model could be applied to the average creep functions of both treated and untreated cells.

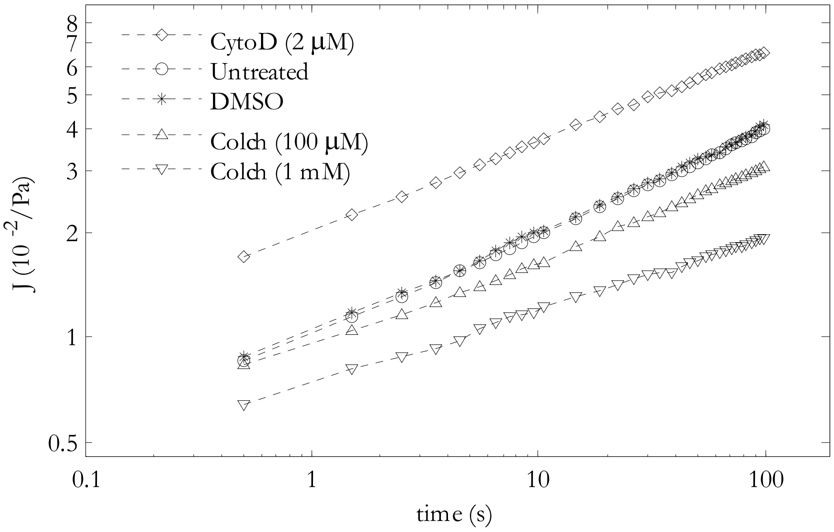

Fig. 5.7. Power-law behavior of average creep functions after drug treatments.

The average compliance constant and power-law exponent were computed for each treatment and plotted in Fig. 5.8, together with superimposed standard error. DMSO (0.1%) treatment did not cause any change in mechanical properties (Fig. 5.8(a) and (b)), which is consistent with the finding by others (Tsai *et al.* 1998). The treatment with cytoD (2 μM) caused a 2-fold increase in A_J (Fig. 5.8(a)), which is qualitatively consistent with previous findings for single cells tested using OMTC (Fabry *et al.* 2003) or for fibroblast populated matrices probed with dynamic stretch (Wakatsuki *et al.* 2001). However, the exponent of untreated cells was significantly decreased by the cytoD treatment, from 0.3 to 0.26 (Fig. 5.8(b)). This is different from the findings of OMTC and AFM experiments, where significant increase was revealed (Fabry *et al.* 2003; Smith *et al.* 2005). It is noted that OMTC and AFM probes the cytoskeleton from the cell surface and with small deformation whereas micropipette aspiration measures the global smeared properties of cells with large deformation. This might explain the above discrepancy.

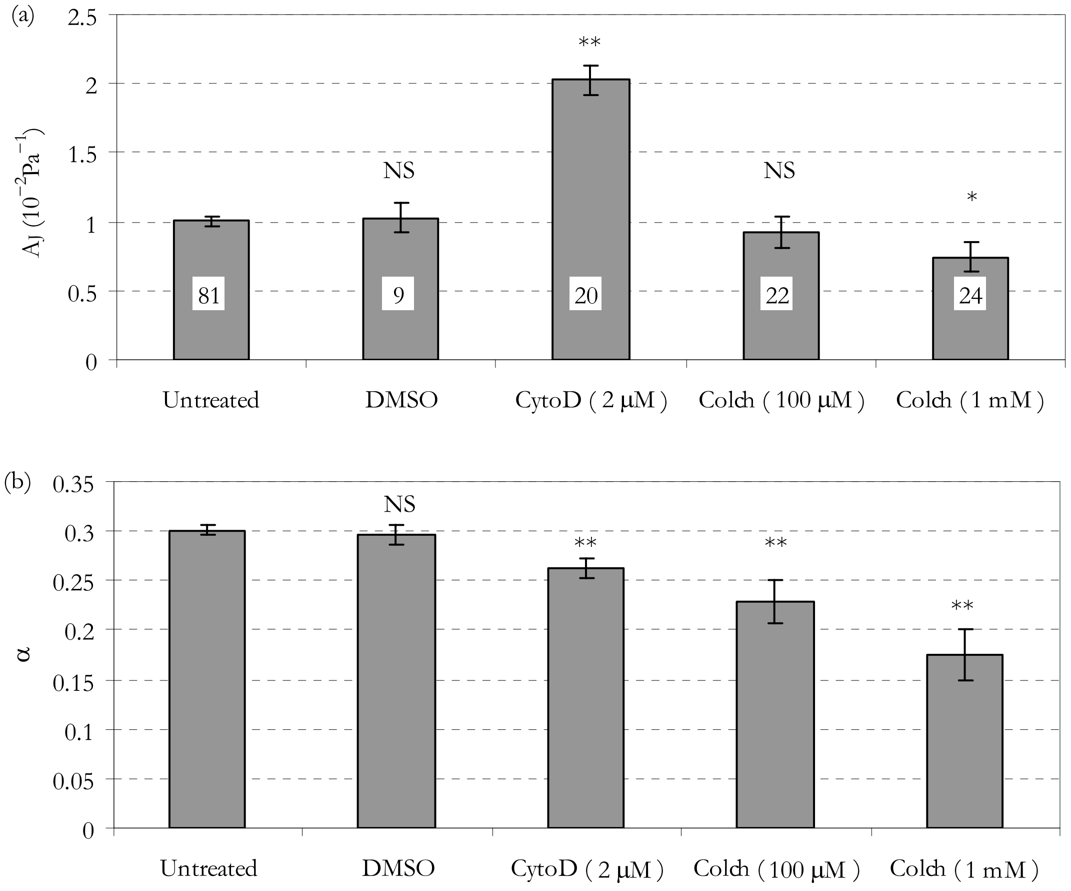

Fig. 5.8. Effect of drug treatments on power-law coefficients: (a) compliance constant A_J and (b) power-law exponent α. Error bars are standard errors. The significance level of the change caused by drug treatments is denoted as NS (not significant, $p > 0.3$), * (significant, $p < 0.05$) or ** (highly significant, $p < 0.01$). The numbers in (a) denote the sample size measured for each drug treatment.

Colchicine treatment at 100 μM caused negligible change in A_J but a significant decrease in α, suggesting a more elastic behavior (Fig. 5.8(a) and (b)). A higher concentration of colchicine (1 mM) caused significant decrease in both A_J and α., suggesting that the treated cells became stiffer and less dissipative (Fig. 5.8(a) and (b)). At both concentrations, some of the treated cells were found to exhibit strong active motion both in free suspension and during aspiration (Fig. 5.6(d)). The intensity and frequency of the active motion was higher with the higher dosage. The percentages of activated cells in all mechanically tested were approximately 30% for 100 μM and 60% for 1 mM. The active motion might be due to the enhanced contractile activity (Keller *et al.* 1984; Danowski 1989) as well as actin polymerization and stress fiber formation (Enomoto 1996; Tsai *et al.* 1998) stimulated by microtubule depolymerization. Therefore, the passive contribution of microtubules to the overall mechanical properties of NIH 3T3 fibroblasts may not be readily quantified by microtubule depolymerization.

5.3 Discussion

5.3.1 Power-law behavior of creep function and its dependence on pipette edge effect

In this chapter, creep experiments were performed on suspended fibroblasts using large pipettes. Coherent deformation of cells was generally induced (Fig. 5.6), which is consistent with the observations of ramp tests.

The creep function measured for suspended fibroblasts with and without drug treatments was found to depend on time with weak power law (Fig. 5.3 and Fig. 5.7). This power-law behavior is qualitatively similar to that of the creep functions measured with other techniques for a variety of cell types as well as cell nuclei (Lenormand *et al.* 2004; Yanai *et al.* 2004; Dahl *et al.* 2005; Desprat *et al.* 2005) and is consistent with the power-law structural damping model for the complex modulus (Fabry *et al.* 2001a; Lenormand *et al.* 2004; Desprat *et al.* 2005; Lenormand and Fredberg 2006). This work thus further substantiates the generality of the power-law rheology model, in the time domain and for suspended cells. The physical explanation for the power-law structural damping model lies in the soft glassy rheology hypothesis, which regards the cytoskeleton as a soft glassy material existing close to glass transition (Sollich 1998; Fabry *et al.* 2001a; Fabry *et al.* 2003).

It is noted that the stress-free projection length (L_p^{SF}) was quantified from ramp experiments (Fig. 4.5) and the deformed projection length was estimated as $L_p = L_p^T - L_p^{SF}$ (L_p^{SF}-based estimation). Previous micropipette aspiration studies which reported the creep deformation of cells generally did not quantify the stress-free projection length (e.g. Evans and Kukan 1984; Evans and Yeung 1989; Tsai *et al.* 1993). Following these, if the detected edge is taken as the real pipette edge (cf. Fig. 4.6), L_p will be calculated as $L_p = L_p^T - L_p^G$ (L_p^G-based estimation). The L_p^G-based creep function can then be derived according to Eq. (5.1). This creep function, which is shown in Fig. 5.9, is qualitatively similar to that observed for leukocytes in micropipette aspiration (Figures (4) to (6) in (Evans and Kukan 1984)). It curves up slightly and is better fitted by the SLS-D model than by the power-law model, judging from the R^2 values (Fig. 5.9).

In addition, the power-law exponent for the L_p^G-based creep function is $\alpha = 0.21 \pm 0.03$, which is significantly lower than that for L_p^{SF}-based creep function (0.30 ± 0.05), while the compliance constant for the L_p^G-based creep function is $A_J = 1.7 \pm 0.3$ (10^{-2} Pa^{-1}), which is much higher than that for the L_p^{SF}-based creep function (1.0 ± 0.3 (10^{-2} Pa^{-1})). It is noted that the effect of drug treatments will not be qualitatively affected by the pipette edge effect, as long as the cell deformation for both treated and untreated cells is computed based on the same edge location.

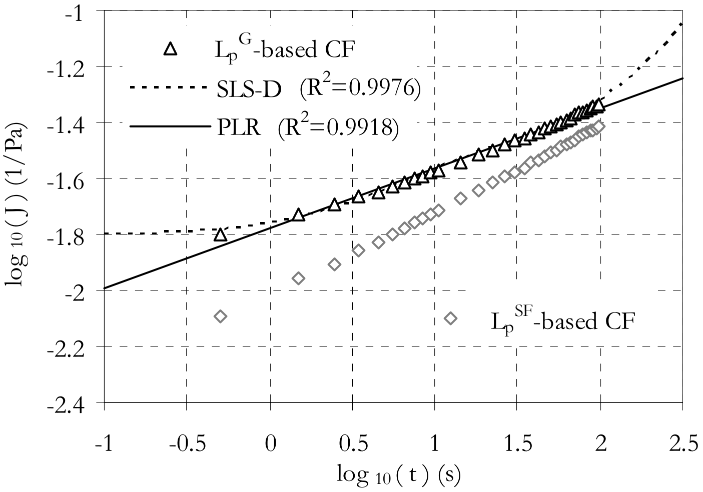

Fig. 5.9. Fitting the L_p^G-based creep function (CF) with the power-law rheology (PLR) model and SLS-D model. The L_p^{SF}-based creep function is also shown for comparison.

In view of the above, the power-law relationship is very sensitive to the addition of a constant, such as that caused by the pipette edge effect. In this work, the pipette edge effect was estimated indirectly from ramp experiments. Alternatively, direct approach can be employed to enhance the imaging resolution such that the deformed projection length can be directly and accurately quantified.

5.3.2 Compatibility between creep tests and ramp tests

In the ramp tests, the apparent deformability S/R_p was measured at two loading rates by applying linear curve fitting to the pressure-deformation relationship (cf. Chapter 4). On the other hand, the apparent deformability can also be predicted based on the measured power-law creep function (Appendix B.6). Thus, the compatibility between creep tests and ramp tests can be examined by comparing S/R_p measured by the latter versus that predicted from the creep function measured by the former.

Based on the power-law creep function (Eq. (5.2)), the deformation of a cell in a ramp test carried out with micropipette aspiration can be derived as (see Appendix B.6)

$$\frac{L_p(t)}{R_p} = \frac{\Phi_P v_{\Delta P}}{2\pi(1+\alpha)} A_J t^{1+\alpha} = \frac{\Phi_P \Delta P(t)}{2\pi(1+\alpha)} A_J t^{\alpha} \tag{5.5}$$

where $\Delta P(t) = v_{\Delta P} t$, $v_{\Delta P}$ being the loading rate.

Given the average power-law parameters ($\alpha = 0.3$ and $A_J = 1.0$ (10^{-2} Pa^{-1})) measured with the creep tests and the loading rates used in the ramp tests, the relation between pressure and deformation can be calculated for the typical pressure range between 1 and 10 mmH$_2$O (Fig. 5.10). From the average slope of $L_p(t)/R_p$ versus $\Delta P(t)$, the apparent deformability was calculated as 0.0725 (1/mmH$_2$O) for the loading rate of 1/30 cmH$_2$O/s, and 0.110 (1/mmH$_2$O) for 1/120 cmH$_2$O/s (Fig. 5.10), which compares favorably (within 5% error) with those found with the ramp tests (cf. Table 4.1). This further substantiates the applicability of the power-law rheology model.

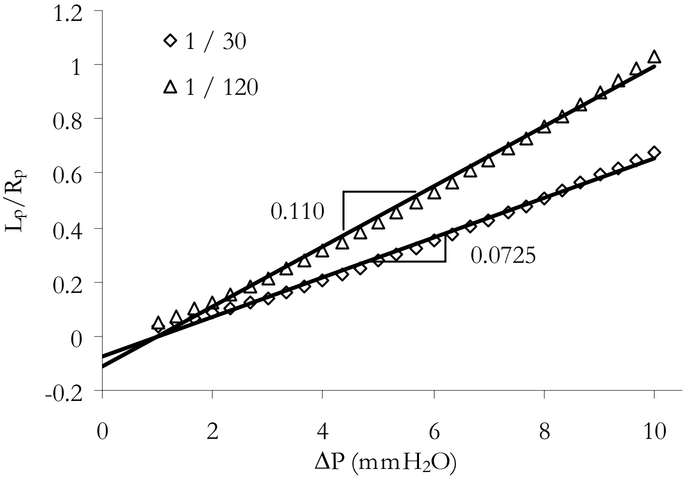

Fig. 5.10. Predicting the ramp-test deformation based on the creep-test results. The pressure-deformation relationship for ramp tests was computed based on Eq. (5.5) for two loading rates, 1/30 and 1/120 cmH$_2$O/s. The apparent deformability was taken as the average slope of the curves.

It is noted that the curves in Fig. 5.10 slightly curve up. In contrast, in ramp experiments, the ΔP-L_p^T curves were generally observed to be fairly linear for ΔP = 0 ~ 1 cmH$_2$O and slightly curving down for higher pressure (Fig. 4.2(b)). The discrepancy might arise from the friction between the cell and the pipette wall, active force of the cell and/or from the nonlinearity in the viscoelasticity of the cell, which remain to be further explored.

The linear regression lines in Fig. 5.10 do not pass through the original point and have a negative y-intercept, which implies that linear regression may lead to underestimation of the SF projection length in ramp tests (cf. Fig. 4.2(b)). For the loading rate of 1/120 cmH$_2$O/s, the y-intercept is $L_p/R_p = -0.1$ (Fig. 5.10), which will lead to ~ 0.45 μm underestimation of L_p^{SF} for a typical pipette size of 9 μm. Similarly, the amount of underestimation of L_p^{SF} for 1/30 cmH$_2$O/s is about ~ 0.3 μm, which is small compared with the measured L_p^{SF} (~ 2.7 μm for $2R_p$ = 9 μm according to Eq. (4.4)). In addition, the nonlinearity of ΔP-L_p^T relation is not apparent in the ramp experiments. Therefore, the nonlinearity observed in Fig. 5.10 was not taken into account for estimating L_p^{SF}.

5.3.3 Mechanical properties of fibroblasts – a comparison with others' work

In this work, the shear stiffness constant A_G of suspended NIH 3T3 fibroblasts, was measured as 116.6 Pa on average (ranging from 60 to 350 Pa), which corresponds to $|G^*(1 \text{ rad/s})|$ = 116.6 Pa in dynamic tests. Similar stiffness (100 ± 10 Pa at 1 rad/s) had also been reported for suspended NIH 3T3 fibroblasts using optical stretcher (Wottawah *et al.* 2005). Thoumine et al. (1997b) measured the viscoelastic properties of chick embryo fibroblasts with micropipette manipulation. The SLS model was used to interpret the creep deformation of cells, which results in k_1 = 320 Pa, k_2 = 170 Pa and μ = 1700 Pa·s (cf. Table A.2). This roughly corresponds to A_G = 489 Pa (this estimation is based on the complex modulus for SLS model at ω = 1 rad/s (Eq. (B.8))). AFM indentation on attached NIH 3T3 fibroblasts reported shear storage modulus of 350 to 715 Pa for frequency between 80 and 300 Hz, which translates into A_G = 101 ~ 166 Pa (assuming α = 0.2 for adherent fibroblasts (Lenormand *et al.* 2004)). More recently, Fernandez et al. (2006) measured the shear stiffness of 3T3 fibroblasts with microplate manipulation to be 0.3 ~ 30 kPa at ω = 0.628 rad/s. In view of the above, the stiffness constant measured for suspended fibroblasts using micropipette aspiration is comparable to the measurements made on the same type of cells in suspended state but generally lower than those determined for attached cells.

For suspended NIH 3T3 fibroblasts, the power-law exponent α was found as 0.30 ± 0.05 (mean ± SD, 81 cells). Lenormand et al. (2004) characterized the rheology of attached human fetal lung fibroblasts with OMTC and found that the power-law rheology model applies with $\alpha \approx 0.2$, which is significantly smaller than that found for suspended NIH 3T3 fibroblasts in this work (unfortunately the magnitude of stiffness was not reported for attached fibroblasts). It is known that decreased prestress will lead to lower stiffness and higher exponent (Wang *et al.* 2002; Stamenovic *et al.* 2004). Therefore, the lower stiffness and higher power-law exponent measured for suspended NIH 3T3 fibroblasts might be attributable to the decrease in prestress for suspended cells. To further confirm the effect of suspension on the cytoskeleton, the actin filaments of NIH 3T3 fibroblasts were stain at both adherent and suspended states (Fig. 5.11). It can be seen that the attached cells are taut with actin stress fibers (Fig. 5.11(a)). One the other hand, the actin fibers are relaxed and curved in the suspended fibroblasts (Fig. 5.11(b)).

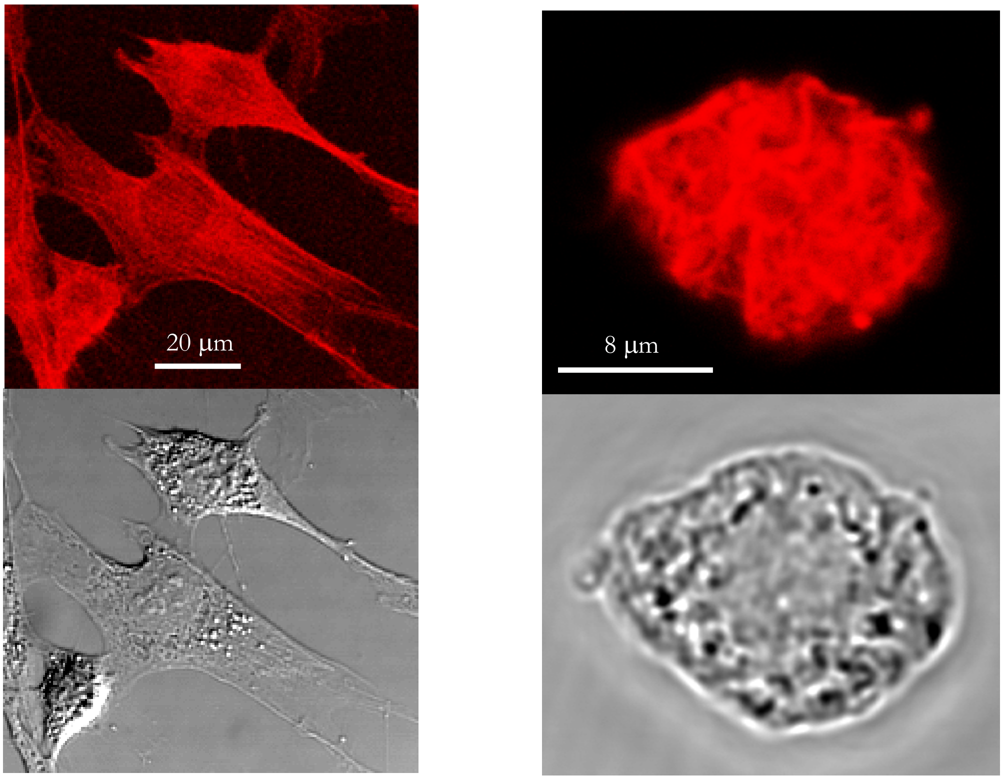

(a) (b)

Fig. 5.11. The difference in actin cytoskeleton for (a) attached and (b) suspended fibroblasts. The upper panels show the fluorescence images of actin cytoskeleton stained with phalloidin-FITC taken with a confocal microscope and the lower ones show the phase contrast images.

5.3.4 A general trend for power-law rheology of cells

The reported parameters for power-law rheology model measured on various cell types, using different techniques and with different drug interventions are compiled in Table A.3 and graphically presented in Fig. 5.12. A general trend is apparent from Fig. 5.12 that lower stiffness is generally associated with higher exponent (negative correlation). This relationship can be approximately described by

$A_G = G_0\omega_0^{-\alpha}$ where $G_0 = 10^4 \sim 10^6$ Pa and $\omega_0 = 10^7 \sim 10^{13}$ rad/s, similar to that reported with OMTC (Puig-De-Morales *et al.* 2004) and AFM (Smith *et al.* 2005).

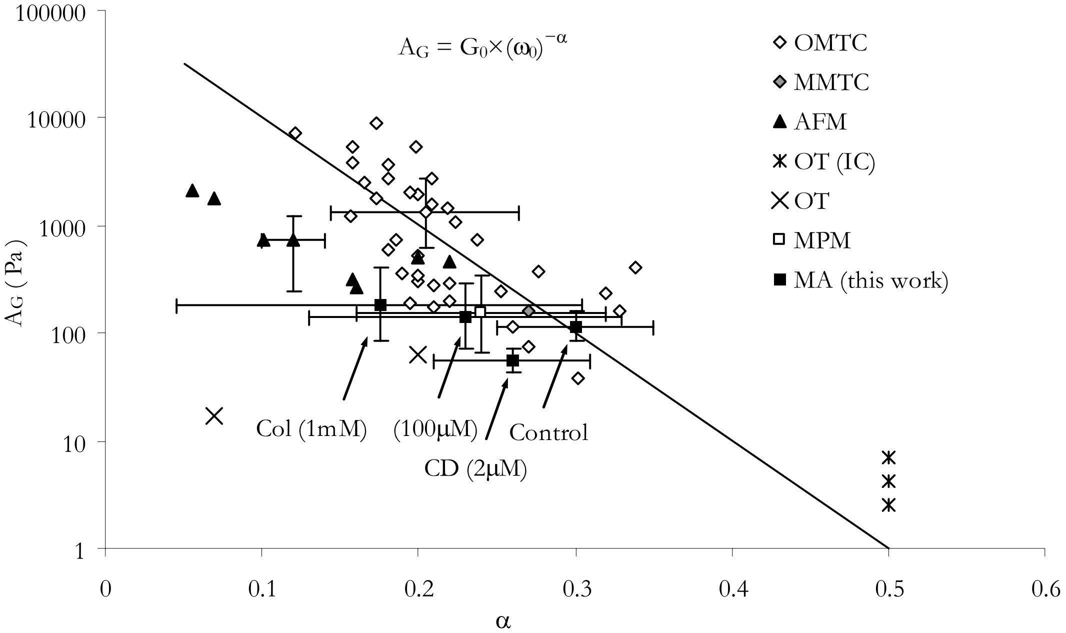

Fig. 5.12. Comparison of the power-law rheology parameters reported with different techniques. For the data acquired with the current work (MA), the drug treatments are indicated by a label with an arrow. Error bars indicate standard deviation. The data sources are as follow: OMTC (Fabry *et al.* 2003; Lenormand *et al.* 2004; Puig-De-Morales *et al.* 2004; Stamenovic *et al.* 2004; Trepat *et al.* 2004; Laudadio *et al.* 2005), MMTC (Puig-De-Morales *et al.* 2001), AFM (Alcaraz *et al.* 2003), OT (IC) (Yanai *et al.* 2004), OT (Balland *et al.* 2005), MPM (Desprat *et al.* 2005), MA (this work). (Abbreviations: OMTC − optical MTC, MMTC − magnetic MTC, OT − optical tweezers, MPM − microplate manipulation, (IC) − intracellular measurements, Col − colchicine. CD − cytochalasin D. For more details including cell types and drug treatments, see Table A.3.)

It is worth noting that negative covariance between $\log_{10}(A_G)$ and α with different drug interventions on the cytoskeleton had also been reported for single types of cells using OMTC and AFM. The α-A_G relation could thus be scaled into master curves which are similar (with comparable G_0 and ω_0) to the one in Fig. 5.12 (Fabry *et al.* 2001a; Fabry *et al.* 2003; Lenormand *et al.* 2004; Puig-De-Morales *et al.* 2004; Laudadio *et al.* 2005; Smith *et al.* 2005). Nonetheless, it is noted that the trend line in Fig. 5.12 does not necessarily describe the covariance of α and A_G with *drug* treatments (drug treatments may also cause simultaneous drop/rise in both α and A_G measured with other techniques, which will be discussed in Section 5.3.6). Instead, it emphasizes the effect of measurement method on the power-law rheology parameters. From Fig. 5.12, the following trend can be observed. OMTC (Fabry *et al.* 2003; Lenormand *et al.* 2004; Puig-De-Morales *et al.* 2004; Stamenovic *et al.* 2004; Trepat *et al.* 2004; Laudadio *et al.* 2005) and AFM (Alcaraz *et al.* 2003), which probe on the cortical cytoskeleton of firmly attached cells, tend to exhibit higher stiffness and lower exponent (thus more elastic). Microplate manipulation (Desprat *et al.* 2005), which involves global cell deformation and less cell spreading, measured slightly lower stiffness and higher exponent. In contrast, micropipette aspiration (this work), which deforms cells globally and in suspension, showed even lower stiffness and higher exponent. Finally, optical tweezer (Yanai *et al.* 2004), which probed the intracellular rheology through trapped organelles, resulted in the lowest stiffness and highest exponent. The reasons for the different rheological properties probed by different techniques remain to be better understood but may involve heterogeneity of the cell and the different level of prestress within the cytoskeleton (Stamenovic *et al.* 2004).

5.3.5 High reproducibility and low variability of the current measurement

Previous experiments on adherent cells routinely found large scattering of mechanical moduli (or compliance), which typically spanned nearly two orders of magnitude for a single cell type tested with the same technique. For example, Bausch et al. (1999) found the shear modulus varied between 20 ~ 735 Pa in the cytoplasm of macrophages (magnetic tweezers). The OMTC experiments revealed that the stiffness of cells varied across two orders of magnitude following a log-normal distribution with geometric standard deviation of 2.1 to 2.8 (Fabry *et al.* 2001b; Fabry *et al.* 2003). Interestingly, four papers using the same OMTC technique reported four different sets of mechanical parameters for untreated human airway smooth muscle cells, with α ranging from 0.158 to 0.209 and A_G ranging from 1308 to 3822 Pa (cf. Table A.3) (Fabry *et al.* 2003; Lenormand *et al.* 2004; Puig-De-Morales *et al.* 2004; Stamenovic *et al.* 2004). Similar scattering had also been observed at the whole cell level using microplate manipulation where the cells adheres to the microplates (Desprat *et al.* 2005; Fernandez *et al.* 2006). Desprat et al. (2005) reported a geometric standard deviation of 2.27 (= $e^{0.82}$) for measured compliance of myoblasts and Fernandez et al. (2006) found the stiffness of fibroblasts to vary from 0.3 to 30 kPa at a single loading frequency.

In contrast, relatively narrower distribution of mechanical moduli (100 ± 55 Pa) was found while performing experiments on suspended fibroblasts with optical stretcher (Guck *et al.* 2005; Wottawah *et al.* 2005). In the current work, the variability for untreated fibroblasts is even less (Fig. 5.12). The geometric standard deviation for A_G is 1.36 based on 81 cells (or 40% of standard deviation with respect to mean if a normal distribution is assumed) (cf. Section 5.2.1.2). Similarly, with the ramp tests, the ratio of the standard deviation to mean of stiffness (assuming normal distribution) was only 36% and 42%, for the loading rates of 1/30 and 1/120 (cmH_2O/s), respectively.

More importantly, the suspended fibroblasts (81 cells) were tested on different days using different pipettes (ranging 7.4 to 10.1 in diameter). The fact that consistent results were obtained with each batch (cf. Fig. 5.5) substantiates the high reproducibility of the current experiment.

The reduced scattering of mechanical properties for suspended fibroblasts might be attributable to three main reasons. Firstly, it may be attributed to the relatively large diameter of the probing pipettes. Larger pipettes tend to deform the cells globally, such that the smeared properties of the whole cell can be measured. On the other hand, AFM, magnetic tweezers and OMTC tend to probe the local properties of smaller area and thus are likely to encounter higher heterogeneity (Bausch *et al.* 1999; Rotsch and Radmacher 2000; Fabry *et al.* 2003). However this may not be the sole reason because microplate manipulation, which revealed large scattering, also probed cells at a global scale (Desprat *et al.* 2005; Fernandez *et al.* 2006). It is noted that the microplates, coated with fibronectin or glutaraldehyde to promote cell adhesion, may stimulate active stress in the cell and increase variability for the measurement (Fernandez *et al.* 2006). In addition, the stiffness measured with microplate manipulation may depend not only on the density of actin stress fibers but also on the orientation of the fibers with respect to the direction of pulling, which is another source of variability. In contrast, cells are less likely to develop active stress in micropipette aspiration because cell adhesion to the glass pipettes was prevented by Sigmacote (cf. Chapter 3). This accounts for the second reason for the reduced variability. Further, the orientation of stress fibers for suspended cells is largely random (Fig. 5.11(b)) and thus may appear more homogeneous and isotropic in response to aspiration by large pipettes, which accounts for the third reason for the reduced scattering.

It is noted that larger heterogeneity of data limits the reproducibility, accuracy and efficiency of mechanical measurements and will necessitate more cells to be tested in order to achieve statistical significance for comparing different groups of cells. In view of the above, micropipette aspiration, when optimized for pipette diameter, is a reliable and sensitive tool for probing the rheological properties of cells.

5.3.6 Effect of actin cytoskeleton disruption

In the current work, 2 μM cytoD was used to disrupt actin cytoskeleton. Staining of actin cytoskeleton for cytoD-treated cells is shown in Fig. 5.13(b). It is found that the stress fibers became largely absent (cf. Fig. 5.11(a)) and actin aggregation is observable, similar to the observation by others (Rotsch and Radmacher 2000; Wakatsuki *et al.* 2001). The treated cells appeared both softer (lower A_G) and more elastic (lower α) (Fig. 5.8 and Fig. 5.13(a)). Similar effect of cytoD on cell stiffness had been widely obtained for other types of cells using other techniques including micropipette aspiration (Sato *et al.* 1990; Trickey *et al.* 2000; Wu *et al.* 2000; Trickey *et al.* 2004). However the change in the power-law exponent is difficult to assess from these studies because the mechanical properties were generally reported in terms of the SLS or other spring-dashpot models. Wakatsuki et al. (2000; 2001) studied the mechanics of fibroblasts with fibroblast populated matrices (FPM). It was found that treatment with cytoD caused the FPM to become both softer and more elastic, as reflected by the reduced phase angle δ in dynamic tests (note that $\tan\delta = G''/G'$), which is qualitatively consistent with the results of the current study.

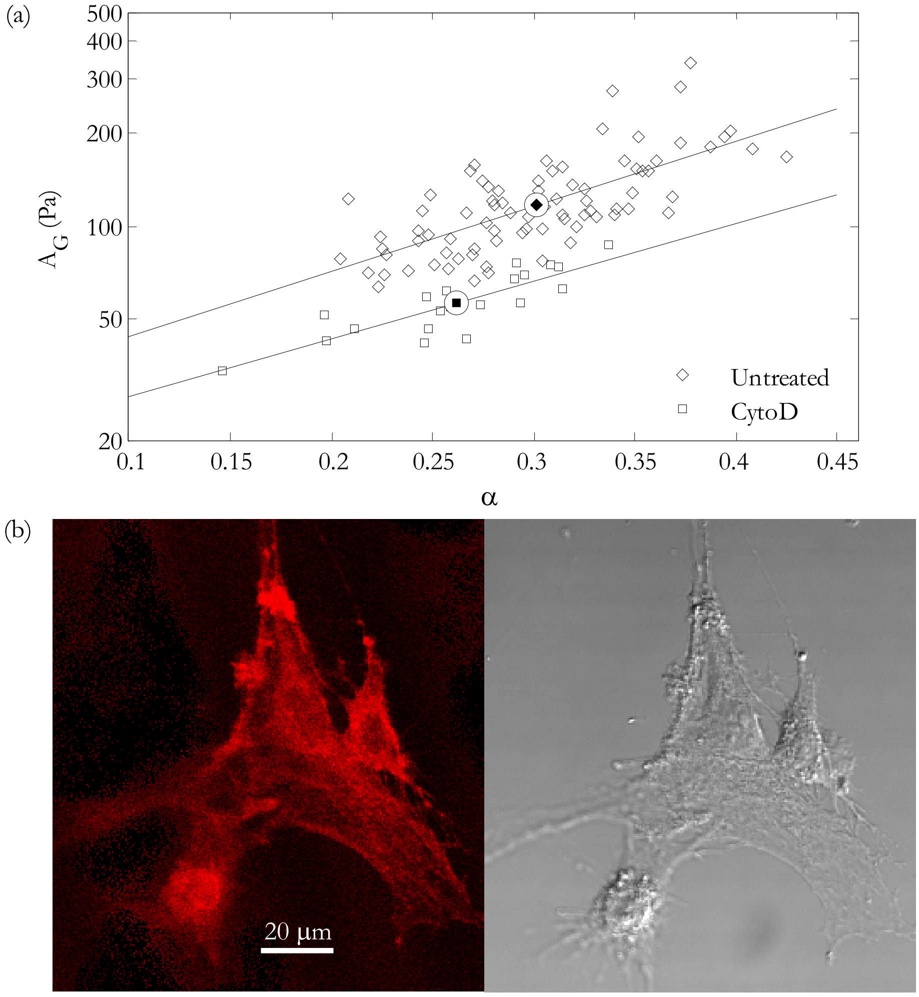

Fig. 5.13. Effect of cytoD treatment on the rheological properties and actin cytoskeleton of NIH 3T3 fibroblasts. (a) Distributions of power-law parameters for untreated and cytoD-treated cells measured with micropipette aspiration. (b) The fluorescence image of actin cytoskeleton (left) and the phase contrast image (right) of cytoD-treated cells.

On the other hand, covariance of α and A_G with negative correlation had been widely observed with OMTC and AFM experiments when the cells were treated with different drug which interfere with the cytoskeleton. In particular, cytoD treatment, while rendering the cells less stiff, was also observed to make the cells more dissipative (higher α) (Fabry *et al.* 2001a; Fabry *et al.* 2003; Lenormand *et al.* 2004; Puig-De-Morales *et al.* 2004; Laudadio *et al.* 2005; Smith *et al.* 2005), which is in contrast to the finding in this study (lower α). It is noted that both OMTC

(Fabry *et al.* 2001a) and AFM (Smith *et al.* 2005) probes from the cell surface at small strain. Thus actin cytoskeleton may be preferentially probed. The fact that higher α were measured with OMTC and AFM after cytoD treatment indicates that disruption of actin filaments caused the actin cytoskeleton to fluidize. In contrast, micropipette aspiration causes large deformation to the whole cell. Thus it is not specific to actin cytoskeleton but measures the integrative behavior of the cell as a whole. When cytoD fluidize the actin network, contribution of other cytoskeletal elements, such as intermediate filaments, microtubules and possibly spectrin-like membrane cytoskeleton (Burridge *et al.* 1982), becomes more prominent when probed with micropipette aspiration. It is possible that these networks are less dissipative than actin cytoskeleton, which explains the lower α value for cytoD treated cells measured with micropipette aspiration. Similar explanation may also apply to the cytoD effect on FPM mentioned above (Wakatsuki *et al.* 2000).

5.3.7 Effect of microtubule cytoskeleton disruption

Although colchicine is well known to depolymerize microtubules (Anderson *et al.* 1982; Andreu and Timasheff 1982), the published results on the effect of colchicine on the rheological properties of cells were inconsistent with each other. Sato et al. (1990) found 2 ~ 3 fold decrease in stiffness of endothelial cells after colchicine treatment (2 μM). In contrast, the micropipette aspiration of neutrophils revealed negligible effect at 0.1 and 1 μM and significant increase in viscosity with higher dosages (10 and 100 μM) (Tsai *et al.* 1998). Rotsch and Radmacher (2000) found little effect on the stiffness of NRK fibroblasts for colchicine at concentration up to 500 μM using AFM indentation. The current work focused on the effect of high dosages of colchicine treatment (100 μM and 1 mM). Activation and rigidification in some of the NIH 3T3 fibroblasts were observed (Fig. 5.6). The colchicine-treated cells exhibited larger scattering in measured mechanical properties, but on average the cells became stiffer and more elastic (Fig. 5.8 and Fig. 5.12).

Interestingly, more than half of the cells tested exhibited active motions after depolymerization of microtubules with 1 mM colchicine (Fig. 5.6(d)). This is consistent with previous findings with microtubule-depolymerizing drugs, such as vinblastine, colcemide, nocodazole and colchicine. Keller *et al.* (1984) found that vinblastine (10 μM), nocodazole (1 μM) and colchicine (10 μM) can stimulate motility and random locomotion in polymorphonuclear leukocytes. Danowski (1989) observed rapidly increased fibroblast contractility following the exposure to vinblastine (10 μM), colcemide (2.7 μM) or nocodazole (16.7 μM). Formation of actin stress fibers after treatment by vinblastine or colcemide has also been observed in Balb/c 3T3 cells (Enomoto 1996). The mechanisms that underlie the elevated acto-myosin contractility and stress fiber formation after microtubule depolymerization may involve Rho GTPases signaling (Enomoto 1996; Kjoller and Hall 1999; Wittmann and Waterman-Storer 2001; Omelchenko *et al.* 2002).

In view of the above, the inconsistency in mechanical properties measured for cells treated with high dosage of microtubule-depolymerizing drugs may be largely due to the increased acto-myosin contractility and reorganization of the actin cytoskeleton, which may be cell type-specific (Omelchenko *et al.* 2002). As such, the mechanical contribution of microtubules probably cannot be directly understood by just disrupting them with depolymerizing drugs unless the actin cytoskeleton and acto-myosin contractility can be controlled during the microtubule depolymerization. This might be achievable through inhibition of the Rho kinase, for example using Y-27632 (Uehata *et al.* 1997).

5.4 Conclusions

The rheological properties of fibroblasts were investigated using micropipette aspiration in this and the previous chapters. The ramp tests revealed that large pipettes were needed for producing linear and reproducible deformation of cells and the apparent stiffness was measured at two loading rates. Creep tests were performed on suspended fibroblasts in this chapter. The measured creep functions were found to vary with time following a weak power law for both drug-treated and untreated cells. Despite having only two parameters, the power-law rheology model could fit the creep function better than spring-dashpot models with more parameters. In addition, the parameters for the power-law rheology model have clear physical explanations in the context of a soft glassy rheology hypothesis. Therefore, the power-law rheology model provides a better framework for interpreting the rheological properties of suspended fibroblasts in micropipette aspiration.

This work, together with the work by others, provides widespread support towards the generality of the power-law rheology model, which hints on the possibility that the physical organization of cells is similar to that of soft glassy materials, such as foams, pastes, colloids, emulsions and slurries (Sollich 1998; Fabry *et al.* 2001a). The common features that governs the physical behavior of this class of materials are structural disorder and metastability (Sollich *et al.* 1997). As a result, the cell modulates its mechanical properties mainly by changing the effective temperature (related to α) of its glassy matrix, which in turn determines its ability to deform, flow and reorganize. The soft glassy hypothesis thus stands in contrast to the traditional notion that cells are like gels whose physical properties are governed by sol-gel transition (Pollack 2001). If true, this hypothesis will represent a paradigm shift with broad implications in biology and physics (Fabry and Fredberg 2003).

Chapter 6 Finite Element Simulation of Micropipette Aspiration Based on Power-law Rheology

6.1 Introduction

In the last chapter, the half-space model (Theret *et al.* 1988) was used in combination with the elastic-viscoelastic correspondence principle to calculate the viscoelastic properties of cells. Similar approach has also been widely employed by others to interpret the viscoelastic properties of cells undergoing micropipette aspiration (Sato *et al.* 1990; Ward *et al.* 1991; Sato *et al.* 1996; Trickey *et al.* 2000; Trickey *et al.* 2004; Dahl *et al.* 2005). However, the accuracy of this analytical solution is questionable because it cannot account for the nonlinearity caused by large deformation and contact slippage between the cell and pipette (Baaijens *et al.* 2005; Zhou *et al.* 2005a).

Various numerical studies have been carried out to evaluate the accuracy of the half-space solution using elastic models or SLS models. Haider and Guilak (2000; 2002) developed a boundary element model to simulate the large, viscoelastic deformation of cells in micropipette aspiration, where the cells were modeled with the SLS model. Their work suggested that the creep deformation process ($L_p(t)$) was not proportional to the creep function (cf. Fig. 6 in (Haider and Guilak 2000)). Baaijens *et al.* (2005) applied the finite element (FE) method to simulate micropipette aspiration of chondrocytes, which were modeled as a two-mode viscoelastic model (essentially equivalent to the SLS model). The authors qualitatively showed that the experimental creep data could be fitted with the simulation, without assessing the accuracy of the viscoelastic half-space solution.

Zhou *et al.* (2005a) also performed FE analysis of micropipette aspiration, the cells being modeled as a standard neo-Hookean solid model (a large-strain version of the SLS model). The viscoelastic deformation of the cells was found to be significantly affected by pipette size and the half-space solution was found reasonably accurate only when pipette diameter is less than one fourth of cell diameter. All the studies above treated the cell as elastic solid or SLS solid.

The extensive experimental evidence, including that presented in the last chapter, supported the general applicability of the power-law rheology model to cell viscoelasticity (Fabry *et al.* 2001a; Alcaraz *et al.* 2003; Lenormand *et al.* 2004; Yanai *et al.* 2004; Balland *et al.* 2005; Dahl *et al.* 2005; Desprat *et al.* 2005). However, a FE model for modeling power-law rheology of cells is not available. Further, no numerical simulation has been done to assess the accuracy of the half-space model when the cell is modeled with power-law rheology.

In this chapter, a finite-strain, viscoelastic FE model will be developed based on the power-law rheology to simulate micropipette aspiration experiments, including both ramp tests and creep tests. One of the major goals was to study the effect of the power-law exponent on the deformation of cells. The effect of pipette geometry on cell deformation will also be systematically assessed. Validation of the proposed model is carried out by comparing the simulation results with those of experiments. It is hoped that a large-strain viscoelastic FE model with experimental verification may contribute towards the study of mechanotransduction by predicting the distribution of stress and strain within cells (Guilak et al. 1999; Humphrey 2001; Charras and Horton 2002a; Charras and Horton 2002b; Charras et al. 2004; Lim et al. 2006).

6.2 Material constitutive relations

6.2.1 Neo-Hookean elasticity

The hyperelastic material model utilizes a general strain energy potential to describe the material behavior at finite strain for incompressible rubber-like materials (ABAQUS 2003b). The incompressible neo-Hookean constitutive law is the simplest hyperelastic model and is characterized by only one parameter, the shear modulus *G*. The strain energy density function of an incompressible neo-Hookean material is

$$U = \frac{G}{2}\left(I_1 - 3\right) \tag{6.1}$$

where I_1 is the deviatoric strain invariant, defined as

$$I_1 = \lambda_1^2 + \lambda_2^2 + \lambda_3^2 \tag{6.2}$$

with λ_1, λ_2 and λ_3 being the principal stretches. From the virtual work principle, it can be deduced that (ABAQUS 2003b)

$$\begin{gathered} \boldsymbol{\tau} = G\left(\mathbf{B} - \frac{1}{3} I_1 \cdot \mathbf{I}\right) \\ \mathbf{B} = \mathbf{F} \cdot \mathbf{F}^T \qquad \mathbf{F} = \frac{\partial \mathbf{x}}{\partial \mathbf{X}} \end{gathered} \tag{6.3}$$

where $\boldsymbol{\tau}$ is the deviatoric part of the Cauchy stress tensor, *G* is the elastic shear modulus, **F** is the deformation gradient of the current configuration **x** relative to the initial configuration **X, B** is the left Cauchy-Green strain tensor, and **I** is the unit tensor. The neo-Hookean hyperelastic model reduces to the linear model for small deformation and does not deviate far from the linear elastic model at large deformation. In fact, for simple shear, the engineering shear stress is proportional to engineering shear strain by

$$\tau = G\gamma \tag{6.4}$$

Therefore, the shear moduli of linear elasticity and neo-Hookean elasticity are directly comparable.

6.2.2 Power-law rheology approximated by Prony series expansion

As a time domain generalization of the neo-Hookean hyperelastic model, the elastic shear modulus need to be replaced by the relaxation shear modulus. The relaxation shear modulus corresponding to the power-law rheology is

$$G(t) = \frac{A_G}{\Gamma(1-\alpha)} t^{-\alpha} = G(1) t^{-\alpha} \tag{6.5}$$

which is the same as Eq. (5.4) (also see Appendix B.4); *G*(1) being the relaxation modulus at 1 s. In Chapter 5, the average rheological properties of suspended NIH 3T3 fibroblasts were measured as A_G = 116.6 Pa and α = 0.3 using micropipette aspiration, which corresponds to *G*(1) = 90 Pa. For the FE simulation, the stiffness constant was chosen to be slightly higher than that measured experimentally but equal to the suction pressure for convenience, such that

$$G(t) = G(1) t^{-\alpha} = 100 t^{-\alpha} \text{ Pa} \tag{6.6}$$

where α is variable, as one of the major goals was to study the effect of α on the deformation of cells. Subsequently, the creep compliance of the cell is (cf. Eqs. (5.2) ~ (5.4) and Appendix B.4)

$$J(t) = A_J t^{\alpha} = \frac{1}{\Gamma(1-\alpha)\Gamma(1+\alpha)} \frac{1}{G(1)} t^{\alpha} . \tag{6.7}$$

For the convenience of numerical implementation (ABAQUS 2003a), the relaxation modulus is expressed with the Prony series expansion as

$$G(t) = G(0)\left[1 - \sum_{i=1}^{N} g_i\left(1 - e^{-t/\lambda_i}\right)\right] \tag{6.8}$$

where $G(0)$ is the instantaneous shear modulus, and g_i and λ_i (i = 1, 2, …, N) are material constants characterizing the relaxation spectrum. Typical experimental time scale spans less than 5 decades, which can be adequately described by 5-term Prony series expansion. Given a set of A_G and α, one can use nonlinear least-squares regression to determine the parameters for the Prony series expansion.

Based on the relaxation modulus (Eq. (6.8)), the deviatoric part of the Cauchy stress tensor can be expressed as (ABAQUS 2003b)

$$\begin{gathered}\boldsymbol{\tau}(t) = \boldsymbol{\tau}_0(t) + \mathrm{SYM}\left[\int_0^t \frac{\dot{G}(s)}{G(0)} \mathbf{F}_t^{-1}(t-s) \cdot \boldsymbol{\tau}_0(t-s) \cdot \mathbf{F}_t(t-s)\,ds\right] \\ \mathbf{F}_t(t-s) = \frac{\partial \mathbf{x}(t-s)}{\partial \mathbf{x}(t)}\end{gathered} \tag{6.9}$$

where $\boldsymbol{\tau}_0(t)$ represents the instantaneous stress caused by the current deformation, which can be computed using Eq. (6.3), $\mathbf{F}_t(t-s)$ is the deformation gradient of the configuration $\mathbf{x}(t-s)$ at time $t-s$, relative to the configuration $\mathbf{x}(t)$ at time t, and SYM[·] denotes the symmetric part of a matrix. It is noted that this equation is essentially equivalent to its linear viscoelastic counterpart

$$\boldsymbol{\tau}(t) = \int_0^t G(t-s)\dot{\boldsymbol{\gamma}}(s)\,ds \tag{6.10}$$

except for the calculation of the instantaneous stress and the large-deformation formulation (ABAQUS 2003b).

6.3 Finite element model based on power-law rheology

6.3.1 Basic assumptions

The basic assumptions made for the FE model are as follows:

(a) The material properties are constant, homogeneous and adequately described by the incompressible power-law rheology model.

(b) The micropipette is rigid and the contact between the cell and the pipette is free from adhesion and friction.

(c) The pipette is a round cylinder and the mouth is smooth-edged with a round fillet.

(d) The shape of the cell is spherical and the deformation of the cell is axisymmetric.

(e) Any possible active force generated by the cytoskeleton is not taken into consideration.

6.3.2 Geometric description of micropipette aspiration

Geometric parameters of interest include the cell radius, R_c, pipette radius, R_p, fillet radius, e, and deformed projection length, L_p, as illustrated in Fig. 6.1. ΔP is the hydrostatic pressure difference.

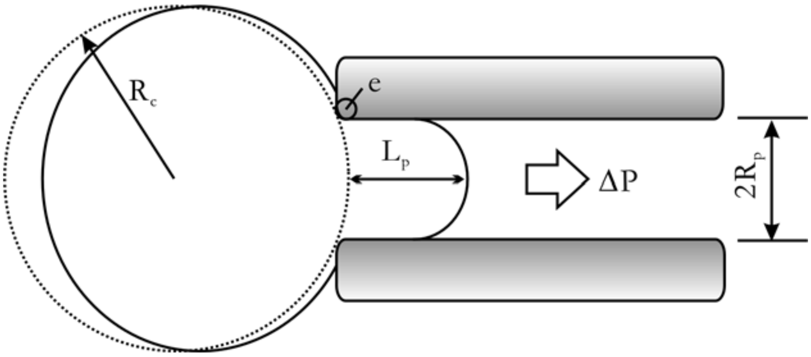

Fig. 6.1. Schematic of micropipette aspiration of a cell.

The geometry is normalized by the initial cell radius R_c. Hence, the dimensionless cell radius, pipette radius and fillet radius are defined by

$$R_c^* = 1 \qquad R_p^* = \frac{R_p}{R_c} \qquad e^* = \frac{e}{R_c} \tag{6.11}$$

As a consequence of this scaling, the computed displacement is also R_c-scaled. The strain and deformation gradients are dimensionless and not affected by the scaling.

For the convenience of comparing with the experimental data, the projection length was usually reported as L_p/R_p, which is dimensionless and not affected by the scaling.

6.3.3 Boundary and loading conditions

The force boundary condition was modeled as a suction pressure exerted on the free surface of the cell tongue inside the pipette (cf. Fig. 6.1), which is the same as that adopted by others (Sato *et al.* 1990; Haider and Guilak 2000; Zhou *et al.* 2005a).

The creep response of a cell to a step pressure of 100 Pa was studied. In the simulation, the pressure was linearly increased from 0 to 100 Pa in 10^{-4} s and then kept constant for 100 s. The effect of α on the creep deformation will be investigated firstly, followed by the effect of pipette geometry.

In the simulation of the ramp tests, the pressure was linearly increased from 0 to 100 Pa within a period ranging from 1 s to 240 s, such that the effect of loading rate can be studied. The effect of α and pipette geometry on the pressure-deformation relationship is examined.

The pipette radii surveyed include R_p^* = 0.25, 0.40, 0.50 and 0.60, the fillet radii include e^* = 0.02, 0.06 and 0.10, and the power-law exponents include $\alpha = 0$, 0.1, 0.2, 0.25, 0.3, 0.35, 0.4 and 0.45. Note that $\alpha = 0$ corresponds to the elastic model.

6.3.4 Finite element mesh

The displacement and pressure-based mixed-formulation finite elements were chosen for the analysis (Bathe 1996; ABAQUS 2003b). Eight-node second-order axisymmetric elements were used to discretize the cell model. A dense mesh was adopted near the pipette fillet because of the concentration of deformation gradient occurring in that region (Fig. 6.2). Convergence study on mesh density and time increment was carried out to ascertain the accuracy of the FE solution before meaningful deductions can be made.

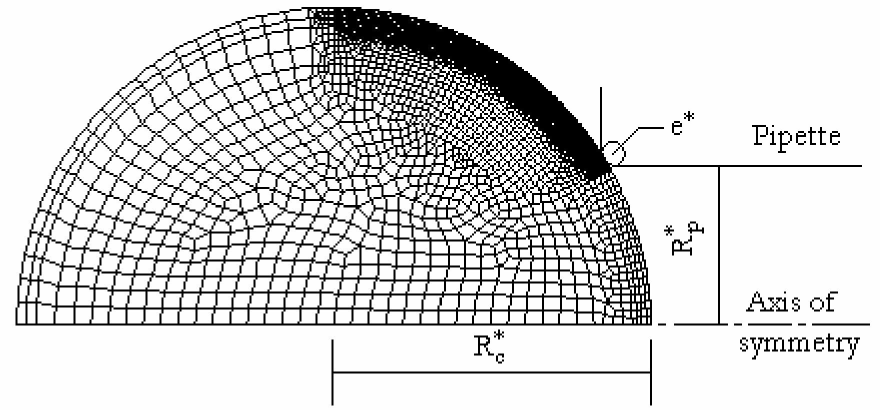

Fig. 6.2. An axisymmetric FE model for a spherical cell, which contains 8061 nodes and 2612 elements. Note that different meshes were used for different pipette sizes to account for the different stress profiles.

6.4 Results

Limitations of the half-space model (Fig. 6.3(b)) had been discussed in Section 4.1. In contrast to the analytical half-space model, the FE simulation can model the large deformation of the cell in micropipette aspiration more accurately by taking into account the realistic cell geometry and the nonlinear effects caused by large deformation and slip (Fig. 6.3(a)). In addition, the FE simulation calculates the viscoelastic deformation through numerical integration, the accuracy of which is ensured by an incremental time-stepping algorithm. Therefore, the FE method is more accurate than the half-space analytical method in solving the initial-boundary-value problem of micropipette aspiration, where large deformation is involved.

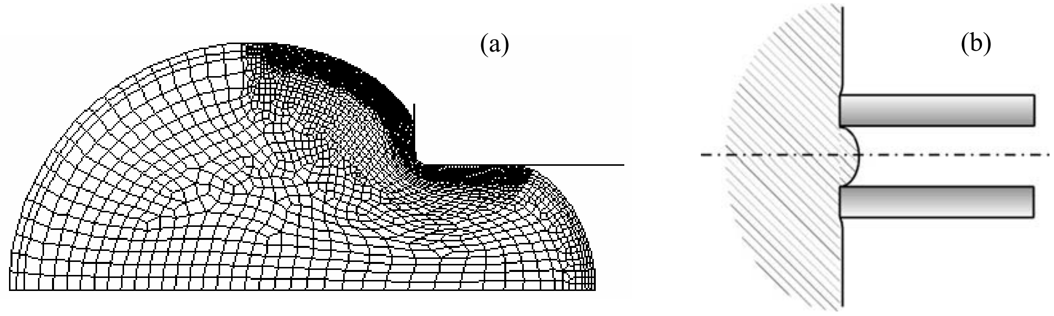

Fig. 6.3. Geometric comparison of the FE model with the half-space model. (a) The deformed FE mesh ($R_p^* = 0.5$ and $e^* = 0.06$) of a cell aspirated into a micropipette. (b) The half-space model.

Through the FE analysis, the effect of the power-law exponent and pipette geometry on the cell deformation will be systematically assessed, in the context of both creep and ramp experiments. As a pilot study, a model with a set of mechanical properties will be proposed for untreated NIH 3T3 fibroblasts. Verification of this model will be carried out by simulating both creep and ramp tests, with different pipette sizes.

6.4.1 Elastic deformation

When $\alpha = 0$, the power-law rheology model reduces to an elastic one, with constant shear modulus: $G = G(1)$. The time-independent force-deformation relationship was derived for pressure up to $\Delta P = 2.5\ G(1) = 250$ Pa. The effect of pipette radius and fillet radius was systematically examined (Zhou *et al.* 2005a).

The FE-simulated force-deformation relationship is shown in Fig. 6.4 for the cases where $e^* = 0.02$ and $R_p^* = 0.25$, 0.40, 0.50 and 0.60.

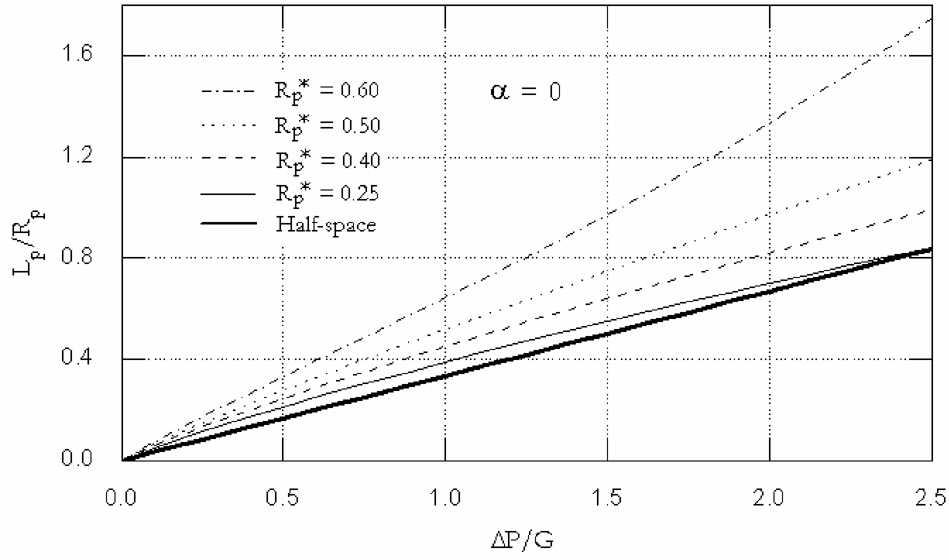

Fig. 6.4. Effect of pipette radius on elastic force-deformation relationship predicted with $\alpha = 0$ and $e^* = 0.02$. The prediction of the half-space model (Eq. (4.1)) is also plotted for comparison.

A comparison of the current neo-Hookean elastic FE solution with that reported by Baaijens *et al.* (2005) revealed favorable agreement. It was found that for the same pressure, the normalized projection length will increase significantly with increasing pipette radius. This happens because when the pipette radius becomes larger with respect to the cell radius, larger slippage will occur between the cell and the pipette wall.

On the other hand, the effect of the fillet radius was found insignificant for moderately large micropipettes ($R_p^* \geq 0.25$) (Zhou *et al.* 2005a). Therefore, it is reasonable to formulate the elastic solution for $0.6 \geq R_p^* \geq 0.25$ by only considering ΔP/G(1) and R_p^*. For simplicity, linear curve fitting was applied to the initial part ($\Delta P/G(1) = 0 \sim 1$) of the force-deformation curves, which resulted in

$$\frac{L_p}{R_p} = C_{FE}^{\alpha=0} \frac{\Delta P}{G(1)}$$
$$C_{FE}^{\alpha=0} \approx 1.6 R_p^{*2} - 0.7 R_p^{*} + 0.47 \tag{6.12}$$

where $C_{FE}^{\alpha=0}$ is the average slope of L_p/R_p against $\Delta P/G(1)$ for $\Delta P/G(1) = 0 \sim 1$ (cf. Fig. 6.4). The dependence of $C_{FE}^{\alpha=0}$ on R_p^* is approximated by a second-order polynomial, which shows good fit to the original data (Fig. 6.5).

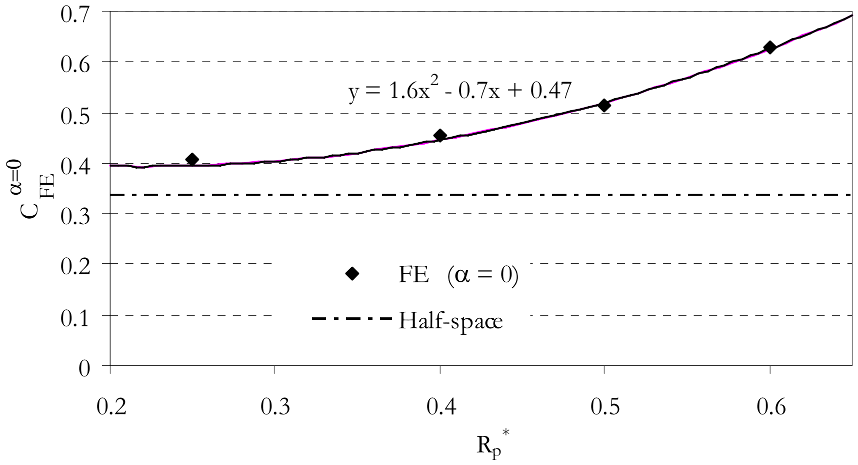

Fig. 6.5. Dependence of $C_{FE}^{\alpha=0}$ on R_p^* for elastic FE analysis ($\alpha = 0$). The equation describes the curve fitted to the elastic FE results. The half-space solution (Eq. (4.1)) is also shown for comparison.

It was found that, for $\alpha = 0$, the slope $C_{FE}^{\alpha=0}$ increased with increasing pipette size and was significantly larger than predicted from the half-space model (Fig. 6.5). This is not entirely consistent with the experimental results (cf. Fig. 4.4 and Fig. 4.8), where the apparent deformability was found only slightly increasing or constant for the pipette sizes between 7 to 10 μm (R_p^* ranging from ~ 0.3 to ~ 0.6). However, as will be shown later, effect of pipette size will decrease when α increases.

6.4.2 Creep deformation

The creep deformation of the cell with $G(t) = 100t^{-\alpha}$ Pa in response to a step pressure of ΔP = 100 Pa was studied. Using the half-space solution (Sato *et al.* 1990), the creep deformation can be derived as (cf. Eqs. (5.1) and (6.7))

$$\frac{L_p(t)}{R_p} = \frac{\Phi_P \Delta P}{2\pi} J(t) = \frac{0.334}{\Gamma(1-\alpha)\Gamma(1+\alpha)} t^{\alpha} = B_{H-S} t^{\beta_{H-S}} \tag{6.13}$$

where $B_{H\text{-}S}$ and $\beta_{H\text{-}S}$ denote the power-law scaling factor and exponent for $L_p(t)/R_p$. The half-space solution does not account for the effect of pipette geometry and large deformation of the cell, which can be investigated through the following FE simulation.

6.4.2.1 Prony-series approximation of power-law rheology and simple shear test

The coefficients for the Prony-series expansion were determined by applying nonlinear curve fitting to discrete data points which represent the power-law relaxation modulus $G(t) = 100t^{-\alpha}$ (α = 0 ~ 0.5) on the time scale t = 10^{-3} ~ 10^{3} s. The Prony-series coefficients are listed in Table C.1 for representative α values. The data points representing the power-law relaxation modulus are plotted together with the Prony-series approximation in Fig. 6.6, which showed good curve fitting. It is noted that the 5-term Prony-series approximation can only fit the relaxation modulus for t = 10^{-3} ~ 10^{3} s, which covers the time scales used in most cell mechanics experiments including the ones in the current work.

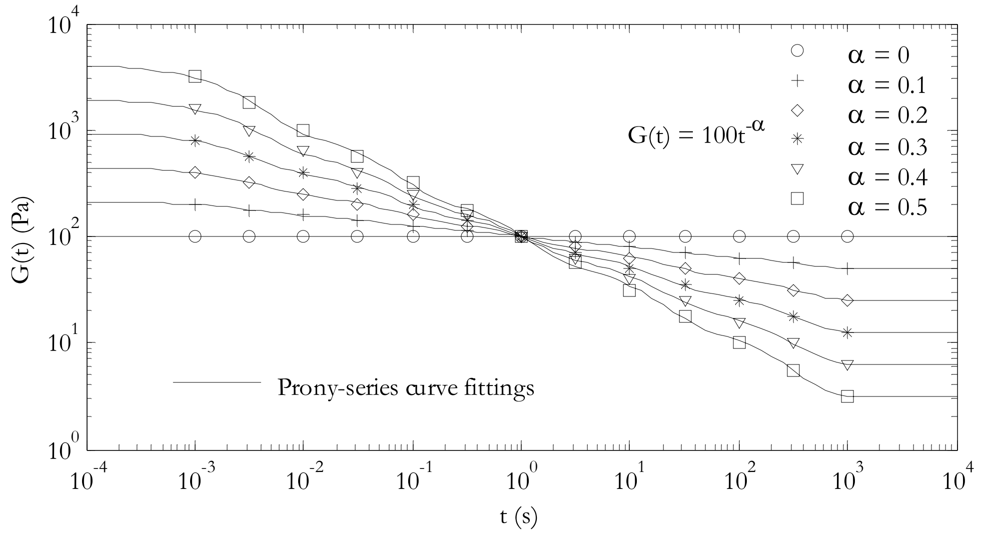

Fig. 6.6. Fitting power-law relaxation modulus with 5-term Prony series expansion. Symbols are data points based on the power-law relaxation modulus and solid lines are Prony-series curve fittings.

In the context of linear viscoelasticity, it is known that $\int_0^t G(t)J(t-\tau)d\tau = t$ (Ferry 1980), from which *J*(*t*) was estimated as Eq. (6.7). At large deformation, the applicability of this formula is unknown. It has been shown that, at simple shear deformation, engineering shear stress τ is proportional to engineering shear strain γ for neo-Hookean elasticity even for large deformation (Eq. (6.4)). Here, simple-shear creep tests are simulated for a single element, the relaxation modulus of which was described by the Prony-series approximation for $G(t) = 100t^{-0.3}$ (cf. Eq. (6.8)). The creep function was defined as $J_{FE}(t) = \gamma(t)/\tau$, τ being the step stress applied at $t = 0$ (cf. inset of Fig. 6.7). The creep functions for the FE model are shown in Fig. 6.7 for different levels of stress together with the analytical prediction $J(t) = 0.0086t^{0.3}$ (cf. Eq. (6.7)). It was found that $J_{FE}(t)$ is very close to *J*(*t*) at low stress but deviates away from $J(t)$ as τ increases. This is indicative of the departure from the theory of linear viscoelasticity at large deformation.

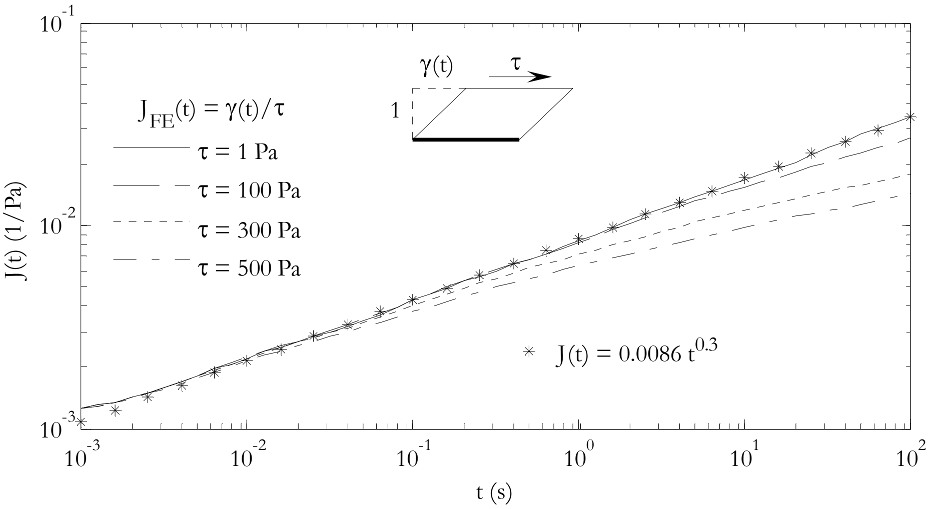

Fig. 6.7. Comparison of FE-computed creep functions at different stress levels with analytical prediction for $\alpha = 0.3$.

6.4.2.2 Power-law behavior of simulated creep deformation

The simulated creep process was represented by the evolution of projection length with time. The simulated creep deformation for different power-law exponents (ranging from 0 to 0.4) is shown in Fig. 6.8. Significant linearity ($R^2 \geq 0.99$) could be seen in the log-log scale. Similar observations were also made for other pipette sizes and power-law exponents (the goodness of fit (R^2) was larger than 0.99 for all cases). It is noted that creep curves, when plotted in linear-linear scale (inset of Fig. 6.8), resemble those predicted with the SLS model (Baaijens *et al.* 2005; Zhou *et al.* 2005a), which has only one relaxation time constant. Thus, the log-log scale is more suitable for examining the relaxation spectrum for cells.

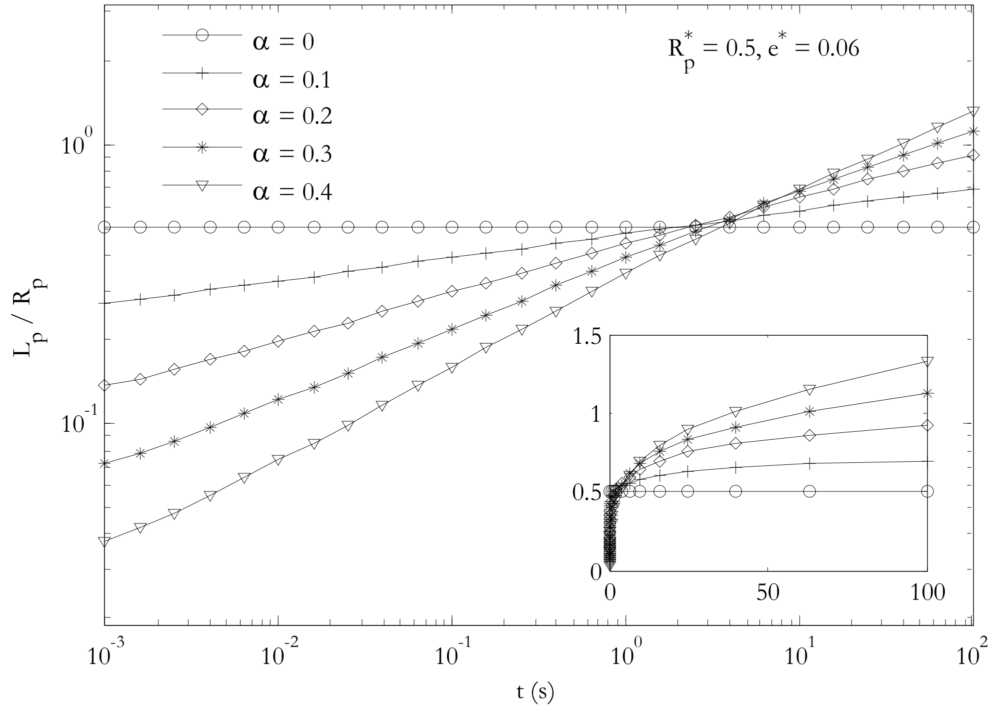

Fig. 6.8. Evolution of L_p/R_p with time for different power-law exponents (α). The inset shows the same data in linear scales. Data is shown for $R_p^* = 0.5$, $e^* = 0.06$.

The creep process can be faithfully fitted with power-law function as

$$\frac{L_p(t)}{R_p} = B_{FE} t^{\beta_{FE}} \tag{6.14}$$

where $B_{FE} = L_p(1\ \mathrm{s})/R_p$ is the scaling constant for scaled projection length and β_{FE} is the average slope of $\log_{10}\left(L_p(t)/R_p\right)$ versus $\log_{10} t$ (Fig. 6.9). Both B_{FE} and β_{FE} are functions of α and pipette geometry, that is, $B_{FE} = B_{FE}(\alpha, R_p^*$ and $e^*)$ and $\beta_{FE} = \beta_{FE}(\alpha, R_p^*$ and $e^*)$.

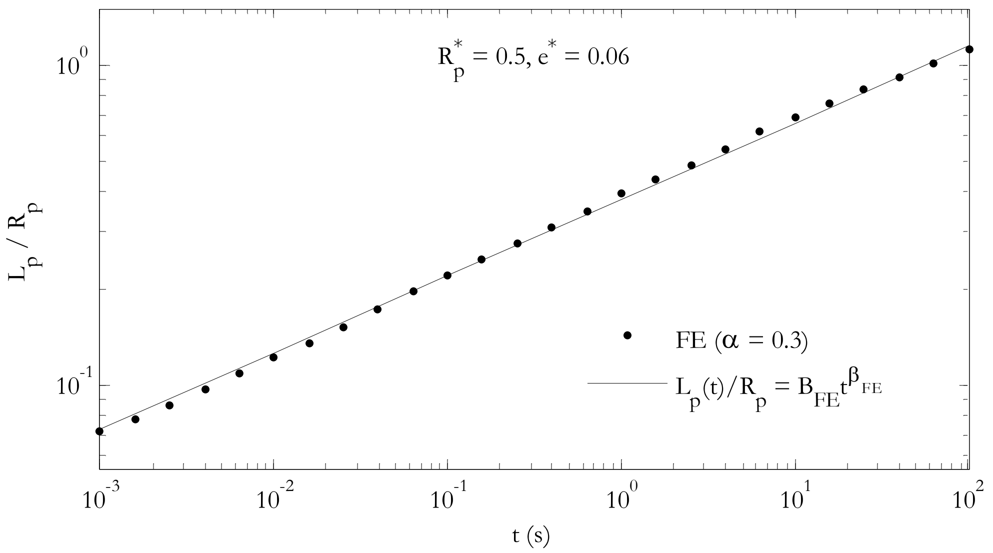

Fig. 6.9. Fitting simulated creep deformation with power-law function (Eq. (6.14)). The FE-simulated data is shown for $R_p^* = 0.5$, $e^* = 0.06$ and $\alpha = 0.3$.

In Chapter 5, the creep deformation of cells in creep experiments was found to follow power-law function, which can be expressed as

$$\frac{L_p(t)}{R_p} = Bt^{\beta} \tag{6.15}$$

where B and β denote the power-law constants for experimentally measured $L_p(t)/R_p$. The average creep function for suspended NIH 3T3 fibroblasts was interpreted as $J(t) = 0.01\ t^{0.3}$ (Pa^{-1}) (cf. Section 5.2.1), which is proportional to $L_p(t)/R_p$ because the half-space solution (Eq. (5.1)) was used. Thus, the average projection length $L_p(t)/R_p$ in response to a suction pressure of 100 Pa can be estimated as $L_p(t)/R_p = (\Phi_P/2\pi)\Delta PJ(t) = 0.334t^{0.3}$. In order for FE-simulated deformation to match that of an average NIH 3T3 fibroblast in micropipette aspiration, the rheological parameters should be chosen such that B_{FE} = 0.334 and β_{FE} = 0.3 for R_p^* = 0.4 ~ 0.6.

6.4.2.3 Effect of α on B_{FE} and β_{FE}

Although the simulated creep deformation can be fitted with power-law functions (Fig. 6.9), its exponent β_{FE} is generally smaller than that of the corresponding relaxation modulus (α). For example, when $\alpha = 0.3$, $R_p^* = 0.5$ and $e^* = 0.06$, the exponent for $L_p(t)/R_p$ is $\beta_{FE} = 0.24$ (Fig. 6.9).

B_{FE} and β_{FE} were calculated for two geometric cases ($R_p^* = 0.25$ and 0.5, and $e^* = 0.06$), for which α was varied between 0 and 0.45. The empirical relation between α and β_{FE} is not sensitive to pipette geometry and can be well described by a power-law equation (cf. Fig. 6.10(a))

$$\beta_{FE} = 0.70\alpha^{0.89}. \tag{6.16}$$

On the other hand, the half-space solution will predict $\beta_{H\text{-}S} = \alpha$ (cf. Eq. (6.13)). It is noted that when $\alpha = 0.387$, β_{FE} approximately equals 0.3 for FE simulation, which matches that measured experimentally.

The effect of α on B_{FE} is shown in Fig. 6.10(b) for the same two cases of pipette geometry, together with the prediction of the half-space solution (Eq. (6.13)). The half-space solution predicted that $B_{H\text{-}S}$ decrease with increasing α according to $B_{H-S} = 0.334/\left[\Gamma(1-\alpha)\Gamma(1+\alpha)\right]$ (cf. Eq. (6.13)). The FE simulation predicted similar trend. However, B_{FE} is larger with larger pipette size in FE simulation, given the same α and e^*.

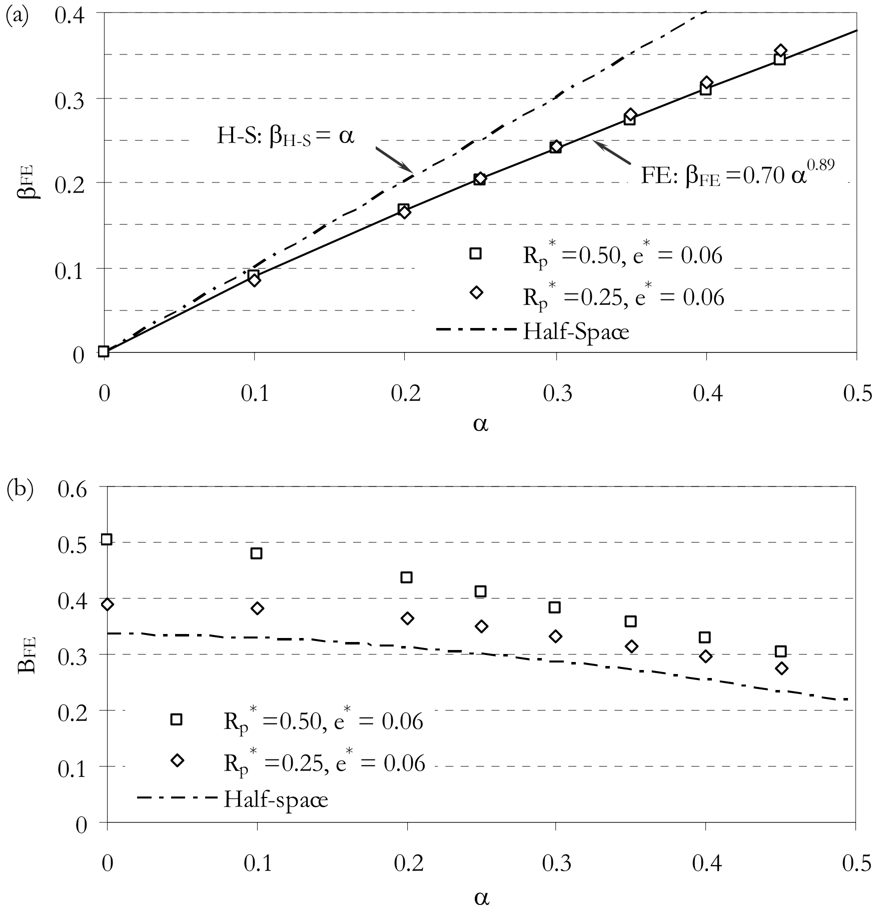

Fig. 6.10. Effect of α on (a) β_{FE} and (b) B_{FE}. The equations in (a) describe the relationship between α and β predicted by the half-space (H-S) solution and the FE simulation.

In addition, as α increases, faster decrease in B_{FE} was observed for the larger pipette than for the smaller one (Fig. 6.10(b)). As a consequence, the relative difference in B_{FE} between the two pipette sizes will decrease as α increases. For example, $B_{FE}(\alpha = 0, R_p^* = 0.25, e^* = 0.06)$ is smaller than $B_{FE}(\alpha = 0, R_p^* = 0.5, e^* = 0.06)$ by 23%, but $B_{FE}(\alpha = 0.45, R_p^* = 0.25, e^* = 0.06)$ is smaller than $B_{FE}(\alpha = 0.45, R_p^* = 0.5, e^* = 0.06)$ by only 10%. This indicates that the effect of pipette geometry is modulated by α, which will be discussed in more details in the next section. When

α = 0.387, B_{FE} falls within the range 0.3 ~ 0.34, which matches the experimental measurement (0.334) favorably (Fig. 6.10(b)).

If the elastic-viscoelastic correspondence principle (Flugge 1967; Schmid-Schonbein *et al.* 1981; Sato *et al.* 1990) is accurate, then $\beta_{FE} = \alpha$. Thus, the simulation results indicate that this principle is not accurate for the current initial-boundary-value problem. The reason why it is inaccurate may be due to the nonlinearity involved in large deformation and the slippage of the cell across pipette edge, which changes boundary condition and causes stress redistribution.

6.4.2.4 Effect of pipette geometry on B_{FE} and β_{FE}

The geometry of the pipette is governed by its radius and the fillet radius (Fig. 6.2). Different pipette size with respect to that of the cell will lead to different stress/strain distribution in the cell and thus may affect the R_p-scaled deformation (Baaijens *et al.* 2005; Zhou *et al.* 2005a).

The effect of R_p^* on B_{FE} and β_{FE}, which characterize the creep deformation, is shown in Fig. 6.11 for different values of α. Firstly, larger pipette radius generally leads to larger scaled deformation, as reflected by higher value of B_{FE}. This is consistent with previous findings from numerical simulations (Baaijens *et al.* 2005; Zhou *et al.* 2005a), which showed that larger slippage will occur with larger pipette radius. In contrast, the half-space model cannot take the slippage into account and will predict a constant value for $B_{H\text{-}S}$. Interestingly, the effect of R_p^* on B_{FE} was found more significant at small α, but weaker at higher α (Fig. 6.11(a)). At α = 0.387, the difference between $B_{FE}(\alpha = 0.387, R_p^* = 0.4, e^* = 0.06)$ and $B_{FE}(\alpha = 0.387, R_p^* = 0.6, e^* = 0.06)$ is only 14%, which is relatively consistent with the experimental observation that the creep compliance constant is insensitive to pipette size (Fig. 5.5(a)). Secondly, β_{FE} is not significantly affected by the pipette radius (Fig. 6.11(b)), consistent with previous observation (cf. Fig. 6.10(a)).

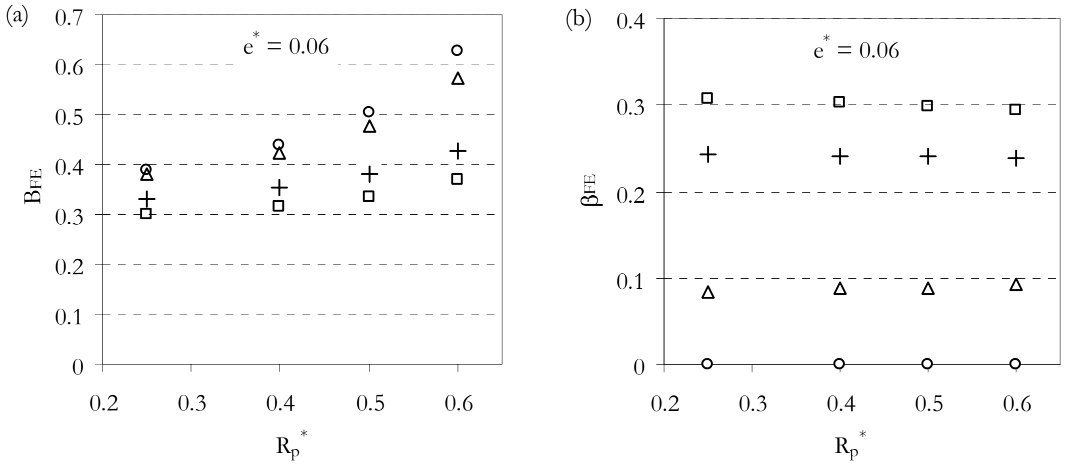

Fig. 6.11. Effect of pipette radius on (a) B_{FE} and (b) β_{FE} for $\alpha = 0$ (○), $\alpha = 0.1$ (△), $\alpha = 0.3$ (+) and $\alpha = 0.387$ (□).

B_{FE} is tabulated in Table 6.1 for $\alpha = 0 \sim 0.4$, $e^* = 0.06$ and $R_p^* = 0.25 \sim 0.6$, together with $B_{H\text{-}S}$ predicted from the half-space solution.

Table 6.1. B_{FE} for $\alpha = 0 \sim 0.4$, $e^* = 0.06$ and $R_p^* = 0.25 \sim 0.6$ and $B_{H\text{-}S}$ for $\alpha = 0 \sim 0.4$.

α	$B_{H\text{-}S}$	B_{FE}			
		0.25	**0.4**	**0.5**	**0.6**
0	0.334	0.389	0.438	0.504	0.627
0.1	0.328	0.382	0.424	0.478	0.575
0.2	0.312	0.362	0.394	0.434	0.499
0.3	0.287	0.332	0.354	0.382	0.428
0.387	0.258	0.300	0.316	0.336	0.368
0.4	0.253	0.293	0.309	0.327	0.358

The effect of fillet radius is shown in Fig. 6.12. Generally, the sharpness of pipette edge (e^*) will affect the local stress concentration near the corner but will not significantly affect the overall stress/strain distribution. The effect of e^* on B_{FE} is shown in Fig. 6.12(a). For $\alpha = 0$, B_{FE} decreases slightly with increase in e^*, but for $\alpha = 0.387$, B_{FE} increases slightly with increasing e^*. The effect of e^* on β_{FE} is shown in Fig. 6.12(b). Generally, β_{FE} increases slightly with increasing e^*, except for $\alpha = 0$. As α increases, the effect of e^* becomes slightly more significant. For $\alpha = 0.387$, $\beta_{FE}(R_p^* = 0.5, e^* = 0.02)$ is smaller than $\beta_{FE}(R_p^* = 0.5, e^* = 0.01)$ by 8%. Overall, the effect of fillet radius on cell deformation is not significant. In addition, the fillet radius has generally not been quantified in the micropipette aspiration experiments and its effect on cell deformation has not been assessed experimentally. Therefore, $e^* = 0.06$ will be used for comparing the experimental data with simulation results.

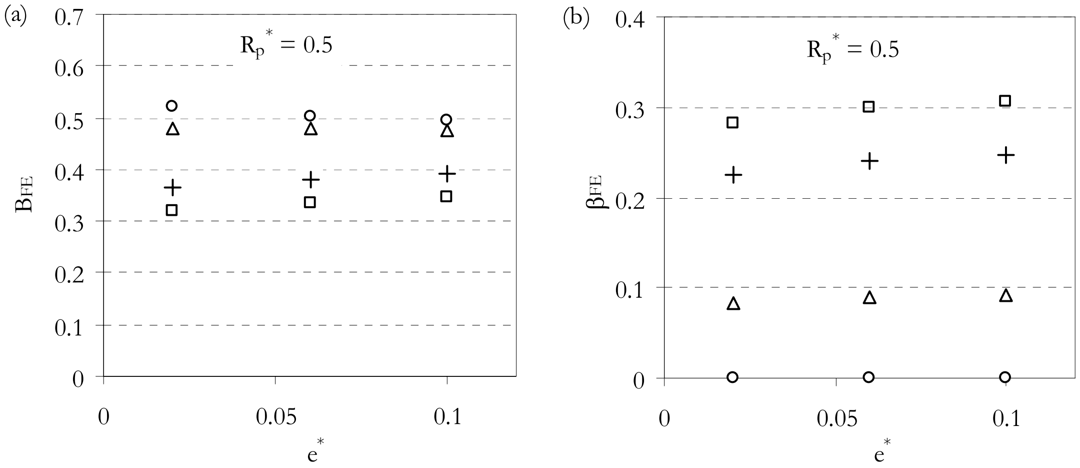

Fig. 6.12. Effect of fillet radius on (a) B_{FE} and (b) β_{FE} for $\alpha = 0$ (○), $\alpha = 0.1$ (△), $\alpha = 0.3$ (+) and $\alpha = 0.387$ (□).

6.4.2.5 Comparison between experiments and simulation

In view of the above, the simulated creep deformation best matches that measured experimentally at $\alpha = 0.387$. Thus, the relaxation modulus of the model cell was chosen to be $G(t) = 100\ t^{-0.387}$ (Pa).

The deformed shapes of the model cell in response to a step pressure of ΔP = 100 Pa were computed by FE-simulation and compared to the observed deformed shapes of a fibroblast in Fig. 6.13. The simulated deformed shapes of the model cell qualitatively matches those observed experimentally.

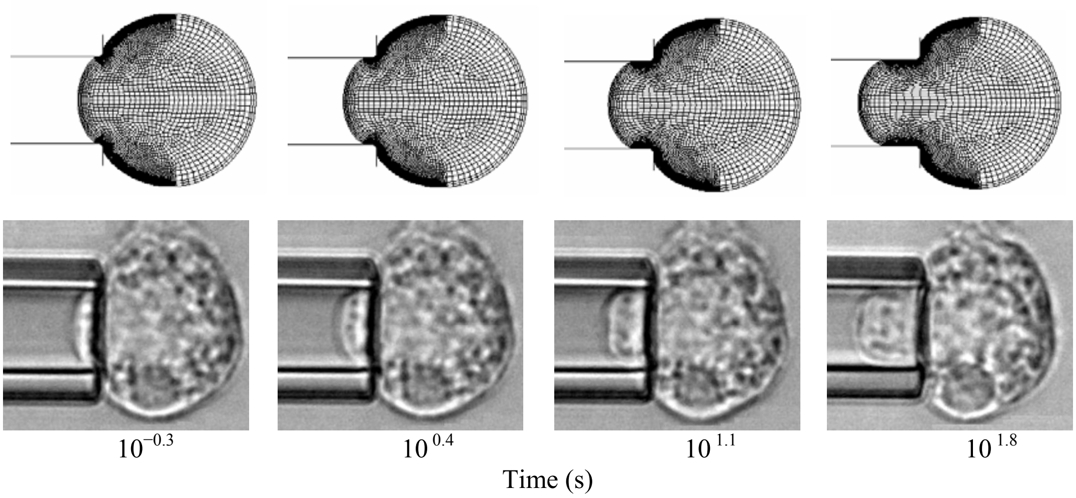

Fig. 6.13. Comparison of deformed cell shapes between simulation and experiments for a creep test at ΔP = 100 Pa. Top row: FE-simulated deformation with $\alpha = 0.387$, $R_p^* = 0.5$, $e^* = 0.06$ at four time points; bottom row: experimentally measured deformation of a fibroblast at the same time points with the pipette diameter being 9 μm ($R_p^* \approx 0.45$).

The simulated creep deformation, as quantified with $L_p(t)/R_p$, is compared with that measured experimentally in Fig. 6.14. The experimental data is from creep tests with $2R_p = 7.4 \sim 10.1$ μm (cf. Section 5.2.1), which corresponds to $R_p^* = 0.4 \sim 0.6$ when scaled with average cell diameter $2R_c = 17.6$ μm. Note that the experimental data (L_p/R_p) in Fig. 6.14(a) was derived from the measured creep function (cf. Fig. 5.2) by multiplying $J(t)$ with $\Phi_P \Delta P/(2\pi)$ (cf. Eq. (6.15)). The experimental data in Fig. 6.14(b) was similarly derived by multiplying the measured A_J (cf. Fig. 5.5(a)) with $\Phi_P \Delta P/(2\pi)$. The experimental data in Fig. 6.14(c) is the same as that presented in Fig. 5.5(b).

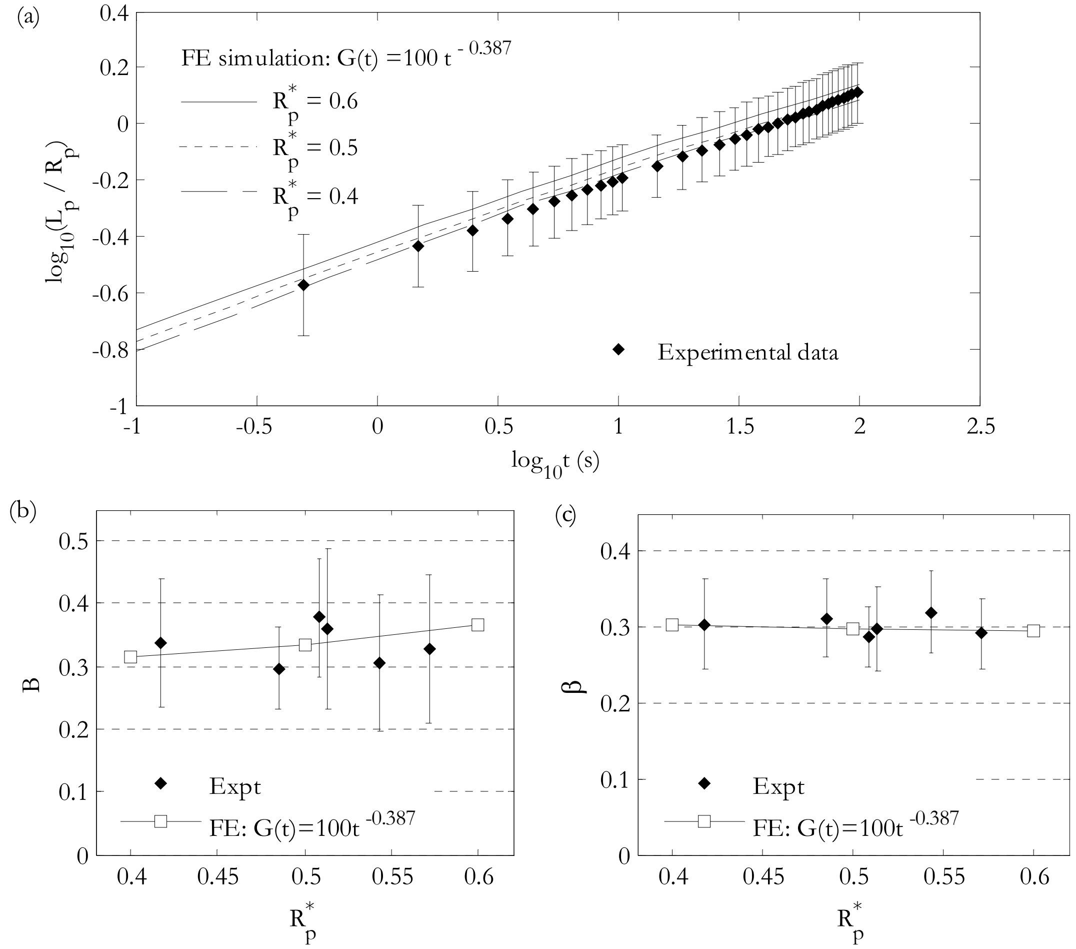

Fig. 6.14. Comparison of (a) creep deformation, (b) the power-law scaling constant, *B*, and (c) the power-law exponent, *β*, between experiments and simulation for creep tests.

Fig. 6.14(a) shows the experimentally-measured creep deformation together with the simulation results with similar pipette sizes. The comparison of B and β between experiments and simulation is shown in Fig. 6.14(b) and (c). Favorable agreement between experiments and simulation can be observed. Although the magnitude of simulated deformation for $R_p^* = 0.6$ is slightly higher than the average deformation obtained experimentally (Fig. 6.14(a)), the difference is within the error range of the experiment. In view of the above, the average relaxation modulus of suspended NIH 3T3 fibroblasts at moderately large deformation can be described by $G(t) = 100\ t^{-0.387}$ (Pa), while the instantaneous elastic behavior is described by neo-Hookean hyperelasticity.

6.4.3 Ramp deformation

The ramp experiments were simulated by increasing the suction pressure from 0 to 100 Pa within a period ranging from 1 s to 240 s. The loading rate $v_{\Delta P}$ thus varied between 5/12 Pa/s and 100 Pa/s. A typical pressure-deformation relationship is shown in Fig. 6.15 for $v_{\Delta P}$ = 10/3 Pa/s (i.e. 1/30 cmH$_2$O/s), $\alpha = 0.3$, $R_p^* = 0.5$ and $e^* = 0.06$. Significant linearity ($R^2 \geq 0.99$) can be observed for the relationship. Similar observations were also made for other values of α and for other pipette geometry. Therefore, the pressure-deformation relationship in FE-simulated ramp tests can be fitted as

$$\frac{L_p}{R_p} = C_{FE}\frac{\Delta P}{G(1)} \tag{6.17}$$

where $G(1)$ = 100 Pa as defined in Eq. (6.6) and C_{FE} is the average slope, as illustrated in Fig. 6.15.

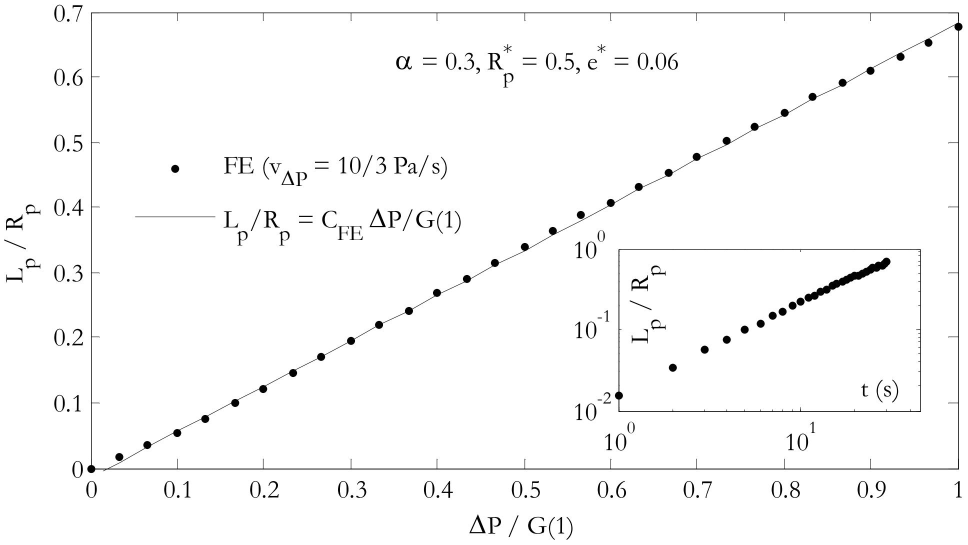

Fig. 6.15. Typical pressure-deformation relationship in a ramp test. The relationship could be fitted with a straight line with the slope C_{FE} = 0.698. The inset shows the increase of deformation with time, which follows a power law with an exponent of 1.126. Data is shown for $v_{\Delta P}$ = 10/3 Pa/s, $\alpha = 0.3$, $R_p^* = 0.5$ and $e^* = 0.06$.

It is noted that the deformation increases with time (or pressure) following a power law (inset of Fig. 6.14). The power-law exponent, 1.126, is much lower than 1.3 (= 1 + α), which is expected theoretically (Eq. (5.5)) (Desprat *et al.* 2005). This underestimation is qualitatively similar to that observed in the simulation of creep tests and may be attributed to similar reasons (cf. Section 6.4.2.3). The pressure-deformation relationship can be fitted closely by a linear equation (Eq. (6.17)) because the power-law exponent (1.126) is close to 1.

C_{FE} is a function of loading rate, α and pipette geometry, that is, C_{FE} = $C_{FE}(v_{\Delta P}, \alpha, R_p^*$ and $e^*)$. The effect of $v_{\Delta P}$, α, R_p^* and e^* on C_{FE} will be examined next.

6.4.3.1 Effect of loading rate and α on C_{FE}

The effect of loading rate on C_{FE} is shown in Fig. 6.16 for different values of α. When $\alpha = 0$ (purely elastic), C_{FE} is independent of loading rate. For a given $\alpha > 0$, the apparent deformability decreases with increasing loading rate according to a power-law function with the exponent $-\beta'_{FE}$, which is the average slope of $\log_{10} C_{FE}$ versus $\log_{10} v_{\Delta P}$ (cf. Fig. 6.16). The rate of decrease, as reflected by β'_{FE}, is faster for higher α. If true for cells, this model suggests that cells are less likely to deform excessively when subjected to a sudden mechanical impact (i.e. high loading rate), but at slow loading rate, e.g. during locomotion or division, the cells will appear very soft, which minimizes energy consumption to remodel their shapes.

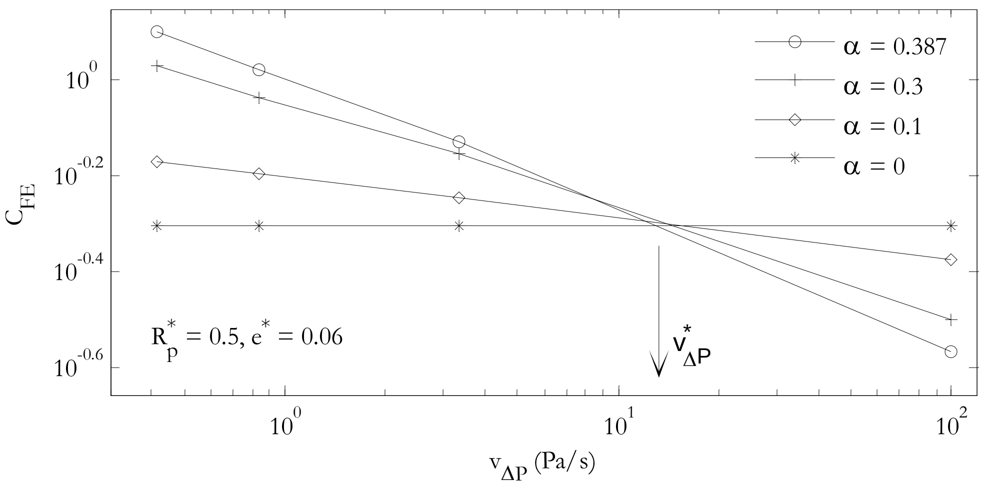

Fig. 6.16. Effect of loading rate on C_{FE} for different α. Data is shown for $R_p^* = 0.5$ and $e^* = 0.06$. $v^*_{\Delta P}$ denotes the approximate loading rate for the crossing point.

Based on the half-space model and elastic-viscoelastic correspondence principle, it can be derived that $C_{FE} \propto v_{\Delta P}^{-\alpha}$ (see Appendix B.7). Thus, β'_{FE} is also a predictor for α. For fixed pipette geometry, the relation between C_{FE}, loading rate, and β'_{FE} can be approximately described by (cf. Fig. 6.16)

$$C_{FE} = C_{FE}^{\alpha=0} \left(\frac{v_{\Delta P}}{v^*_{\Delta P}} \right)^{-\beta'_{FE}} \tag{6.18}$$

where $v^*_{\Delta P}$ is the loading rate for which C_{FE} is independent of β'_{FE}, and $C_{FE}^{\alpha=0}$ is as defined in Section 6.4.1. Similar to the observation for β_{FE} (cf. Fig. 6.11(b) and Fig. 6.12(b)), the dependence of β'_{FE} on pipette geometry is negligible and can be empirically described by $\beta'_{FE} = 0.64\alpha^{0.88}$, which is slightly smaller than β_{FE} (Eq. (6.16)) given the same value of α. $v^*_{\Delta P}$, which is mainly influenced by pipette geometry, equals 10 ~ 14 Pa/s for $R_p^* = 0.5$ and $e^* = 0.06$.

The effect of α on C_{FE} is shown in Fig. 6.17 for fixed pipette geometry (note that the data here is the same as that presented in Fig. 6.16). At low loading rate, e.g. 5/6 Pa/s, higher α led to larger C_{FE}. However, as the loading rate increases beyond a certain threshold, the trend is reversed (cf. the series "$v_{\Delta P}$ = 100 (Pa/s)" in Fig. 6.17). The threshold loading rate for which C_{FE} is not sensitive to α is $v^*_{\Delta P}$ = 10 ~ 14 Pa/s for this pipette geometry (cf. Fig. 6.16).

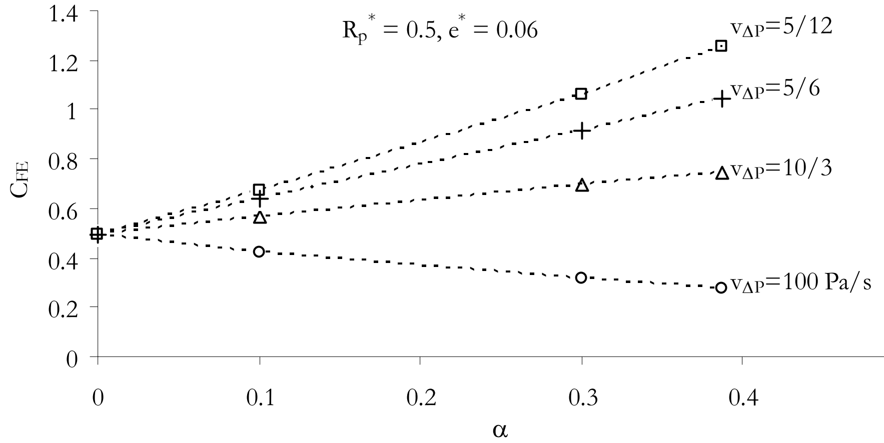

Fig. 6.17. Effect of α on C_{FE}, as modulated by the loading rate.

6.4.3.2 Effect of pipette geometry on C_{FE}

The effect of pipette radius is shown in Fig. 6.18(a), for different α values. The fillet radius was fixed at e^* = 0.06 and the loading rate was $v_{\Delta P}$ = 10/3 Pa/s. Generally, the apparent deformability increases with increasing R_p^* for a fixed α value. But the effect of R_p^* was found less significant with larger α, similar to the observation with simulated creep deformation (cf. Section 6.4.2.4). The difference between $C_{FE}(\alpha = 0.387, R_p^* = 0.4, e^* = 0.06)$ and $C_{FE}(\alpha = 0.387, R_p^* = 0.6, e^* = 0.06)$ is only 8%, which is relatively consistent with experimental observation that the apparent deformability is insensitive to pipette size for moderately large pipettes (cf. Fig. 4.3(b)).

The effect of fillet radius on the apparent deformability is shown in Fig. 6.18(b), for different α values. The pipette radius was fixed at $R_p^* = 0.5$ and the loading rate was $v_{\Delta P} = 10/3$ Pa/s. For $\alpha = 0$, larger e^* (thus smoother fillet) leads to slightly lower deformation. However, as α increases, the trend is reversed. For $\alpha = 0.387$, sharper fillet led to smaller deformation. The difference between $C_{FE}(\alpha = 0.387, R_p^* = 0.5, e^* = 0.02)$ and $C_{FE}(\alpha = 0.387, R_p^* = 0.5, e^* = 0.1)$ is 16%.

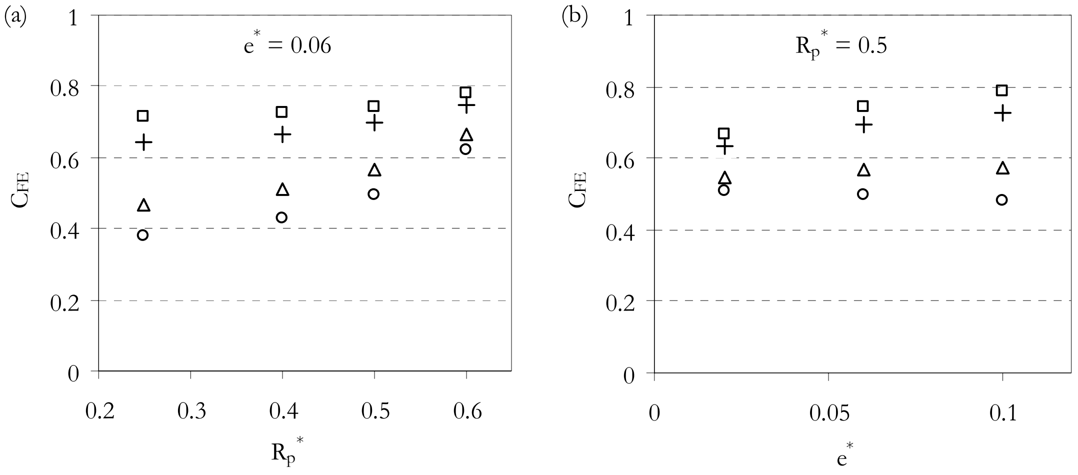

Fig. 6.18. Effect of (a) pipette radius and (b) fillet radius on C_{FE} for $\alpha = 0$ (○), $\alpha = 0.1$ (Δ), $\alpha = 0.3$ (+) and $\alpha = 0.387$ (□) at the loading rate: $v_{\Delta P} = 10/3$ Pa/s.

Although the effect of pipette geometry on C_{FE} is reported only for $v_{\Delta P} = 10/3$ Pa/s, qualitatively similar observations were also made for other loading rates.

6.4.3.3 Comparison between experiments and simulation

In Section 6.4.2.5, the model cell with $G(t) = 100\, t^{-0.387}$ (Pa) was found to satisfactorily represent the average creep behavior of suspended NIH 3T3 fibroblasts. Here, the same model is used to predict the ramp deformation. The simulated deformed shapes of the model cell are compared to those observed experimentally at the same loading rate ($v_{\Delta P} = 10/3$ Pa/s) (Fig. 6.19). The simulated deformed shapes qualitatively resemble those measured experimentally.

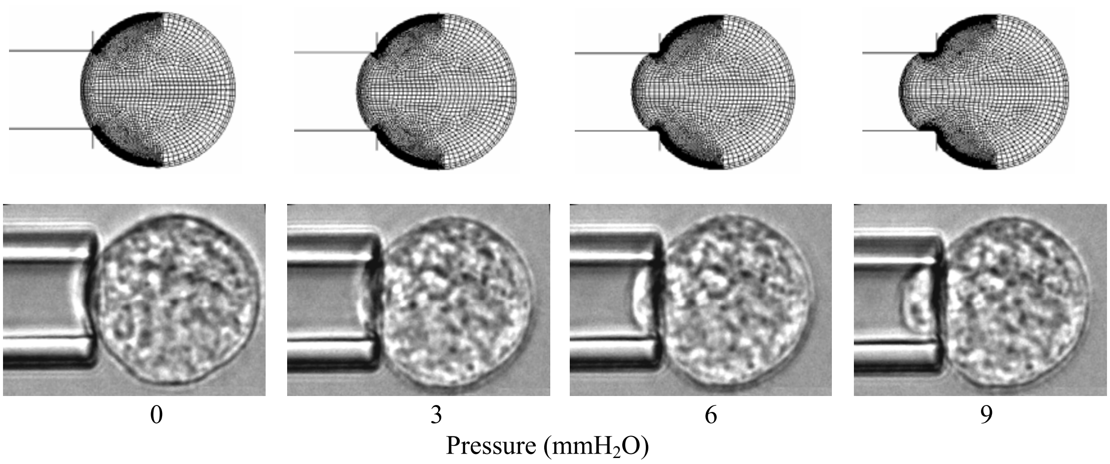

Fig. 6.19. Comparison of deformed cell shapes between simulation and experiments for a ramp test with $v_{\Delta P}$ = 10/3 Pa/s. Top row: FE-simulated deformation with $\alpha = 0.387$, $R_p^* = 0.5$ and $e^* = 0.06$ at four pressure values; bottom row: experimentally measured deformation of a fibroblast at the same pressure values, the pipette diameter being 9.4 μm ($R_p^* \approx 0.45$).

In ramp experiments, the apparent deformability was quantified as S/R_p, S being the average slope of L_p versus ΔP (cf. Fig. 4.2(b)), at two loading rates. Consistent results were obtained using pipettes larger than ~ 7 μm in diameter (cf. Fig. 4.3(b) and Fig. 4.8(b)). On the other hand, the FE-simulated apparent deformability can be computed according to $S/R_p = C_{FE}/G(1)$ (cf. Fig. 6.15). Comparison between experiments and simulation in terms of apparent deformability is shown in Fig. 6.20 for (a) $v_{\Delta P}$ = 10/3 Pa/s and (b) $v_{\Delta P}$ = 5/6 Pa/s. The model prediction is in favorable agreement with experimental results at both loading rates.

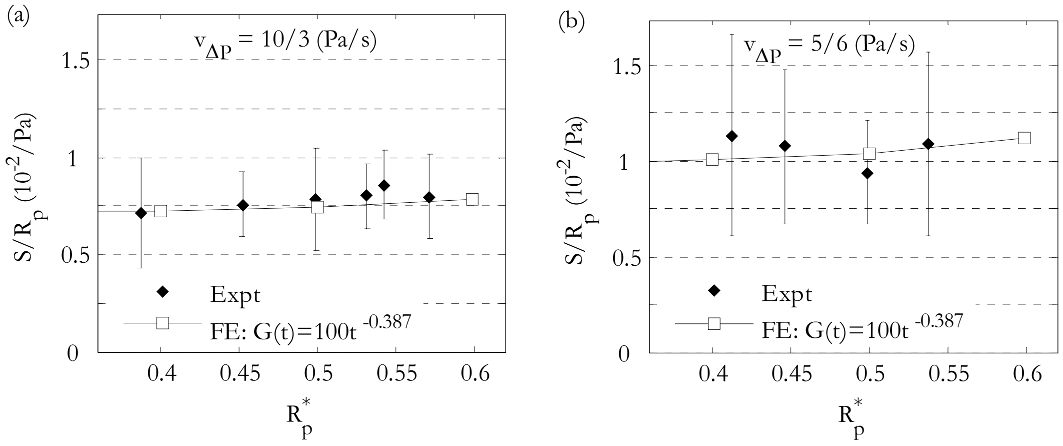

Fig. 6.20. Comparison of apparent deformability between experiments and simulation for ramp tests at two loading rates: (a) 10/3 Pa/s and (b) 5/6 Pa/s.

6.5 Discussion

Here, FE simulation of micropipette aspiration was performed. Implementation of the power-law rheology model in large-deformation FE analysis was achieved by (a) approximating the power-law relaxation modulus with Prony-series expansion and (b) describing the instantaneous elastic behavior with neo-Hookean hyperelasticity. The relaxation modulus of the cells was assumed as G(t) = 100 $t^{-\alpha}$ Pa. The effects of pipette geometry and the power-law exponent (α) on the deformation of cells in micropipette aspiration were systematically assessed. The simulation results are summarized Table 6.2.

Table 6.2. Summary of FE simulation results, in comparison with half-space (H-S) solution. The cell model was $G(t) = 100t^{-\alpha}$ Pa.

Creep deformation at ΔP = 100 Pa	
FE-simulation	Half-space solution
$\frac{L_p(t)}{R_p} = B_{FE}t^{\beta_{FE}}$	$\frac{L_p(t)}{R_p} = B_{H-S}t^{\beta_{H-S}}$
$\beta_{FE}\left(\alpha, R_p^*, e^*\right) \approx 0.70\alpha^{0.89}$ Effect of R_p^* and e^* on β_{FE} is small.	$\beta_{H-S}\left(\alpha\right) = \alpha$
$B_{FE}\left(\alpha, R_p^*, e^*\right) = 0.27 \sim 0.63$ Increase in R_p^* → increase in B_{FE}. Effect of e^* on B_{FE} is α-dependent and small. Increase in α → decrease in B_{FE} and in the influence of R_p^* on B_{FE}.	$B_{H-S}\left(\alpha\right) = \frac{0.334}{\Gamma\left(1-\alpha\right)\Gamma\left(1+\alpha\right)}$ Independent of e^* and R_p^*. Increase in α → decrease in B_{H-S}.
Ramp deformation at varying loading rates	
FE-simulation	Half-space solution
$\frac{L_p}{R_p} \approx C_{FE}\frac{\Delta P}{G\left(1\right)}$	$\frac{L_p}{R_p} \approx C_{H-S}\frac{\Delta P}{G\left(1\right)}$
$C_{FE}\left(v_{\Delta P}, \alpha, R_p^*, e^*\right) \propto v_{\Delta P}^{-\beta'_{FE}}$, $\beta'_{FE}\left(\alpha, R_p^*, e^*\right) \approx 0.64\alpha^{0.88}$ Effect of R_p^* and e^* on β'_{FE} is small.	$C_{H-S}\left(v_{\Delta P}, \alpha\right) \propto v_{\Delta P}^{-\alpha}$
Increase in R_p^* → increase in C_{FE}. Increase in α → decrease in the influence of R_p^* on C_{FE}. Effect of e^* on C_{FE} is α-dependent and small.	C_{H-S} is independent of e^* and R_p^*.

6.5.1 Interpretation of *G*(1) and α using FE simulation results

When the viscoelasticity of the cell is described by power-law rheology, the analytical half-space solution to creep deformation is given by Eq. (6.13). At large deformation, analytical solution is not available for micropipette aspiration. In the FE simulation, it was shown that the simulated creep deformation, as represented by $L_p(t)/R_p$, also follows a power-law function, albeit with different scaling factor and exponent than those predicted by the half-space solution. Thus, following the half-space solution (Eq. (6.13)), a similar empirical formula can be proposed corresponding to the FE simulation results as

$$\frac{L_p(t)}{R_p} = F\left(\alpha, R_p^*, e^*, \Delta P^*\right)\frac{\Delta P}{G(1)}t^{f\left(\alpha, R_p^*, e^*, \Delta P^*\right)} \tag{6.19}$$

where F is the scaling factor for force-deformation relationship, and f is the power-law exponent exhibited by the creep process. Both are functions of α, R_p^*, e^*, and ΔP^* ($\Delta P^* = \Delta P/G(1)$). It is noted that the current study has focused on the effect of α, R_p^* and e^*, whereas the effect of ΔP^*, which may cause slight nonlinearity in force-deformation relationship (cf. Fig. 6.4), remains to be quantified. In the FE simulation, $\Delta P = G(1) = 100$ Pa. Therefore, a comparison between Eq. (6.19) and Eq. (6.14) reveals that $F = B_{FE}$ and $f = \beta_{FE}$. Eq. (6.19) then becomes

$$\frac{L_p(t)}{R_p} = B_{FE}\left(\alpha, R_p^*, e^*\right)\frac{\Delta P}{G(1)}t^{\beta_{FE}\left(\alpha, R_p^*, e^*\right)} \tag{6.20}$$

where $\beta_{FE}(\alpha, R_p^*, e^*)$ and $B_{FE}(\alpha, R_p^*, e^*)$ are quantified in Sections 6.4.2.3 and 6.4.2.4, respectively.

In Chapter 5, the creep deformation of cells in micropipette aspiration was found to follow power-law function when large pipettes were used. Thus, the experimental results obtained with appropriate pipette sizes can generally be expressed in the form of Eq. (6.15). Comparing Eqs. (6.15) and (6.20), and taking Eq. (6.16) into consideration, one reaches at

$$\begin{gathered} \alpha = \left(\beta/0.70\right)^{1.12} \\ G\left(1\right) = \frac{B_{FE}\left(\alpha, R_p^*, e^*\right)}{B}\Delta P \end{gathered} \tag{6.21}$$

where ΔP, β and B are measured experimentally and $B_{FE}(\alpha,\ R_p^*,\ e^* = 0.06)$ is tabulated in Table 6.1. This equation can be used to interpret the rheological properties of cells in creep tests performed using micropipette aspiration. It is noted that the above formula is most accurate when the suction pressure is comparable to the stiffness constant of the cell, as the FE simulation was performed for $\Delta P = G(1)$.

6.5.2 Departure from linear viscoelasticity and correspondence principle

During large deformation of cells in micropipette aspiration, the theory of linear viscoelasticity and the elastic-viscoelastic correspondence principle are no longer accurately applicable, which is manifested as the disparity between the FE simulation and the half-space solution (Table 6.2).

There are two reasons why β_{FE} differs from α. Firstly, at large deformation, the relation between $G(t)$ and $J(t)$ does not accurately obey $\int_0^t G\left(t\right)J\left(t-\tau\right)d\tau = t$ and the power-law exponent for $J(t)$ will be smaller than α, as shown in Section 6.4.2.1. This partially accounts for the difference between β_{FE} and α because large deformation was involved in the simulation of micropipette aspiration. Secondly, the slippage of the cell across the pipette edge leads to stress redistribution, which causes deviation from the elastic-viscoelastic correspondence principle (Flugge 1967). As slippage occurs, a small portion of the cell, which is initially outside of the pipette and subjected to low stress, is moved closer to the pipette edge, where its stress becomes higher. Thus, significant addition of stress will occur at the pipette edge accompanying the slippage. Corresponding to this stress increment, the stiffness of the edge region will approach the instantaneous shear modulus ($G(0)$) and is always higher than the remaining part of the cell. As a consequence of partial stiffening, the creep deformation will be retarded, which leads to lower value of B_{FE} than α. This further explains why β_{FE} is generally smaller than α.

The local stiffening at the pipette edge has another implication. It has been observed that both B_{FE} and C_{FE} will be larger with larger R_p^*. This is mainly due to slippage of the cell across the pipette edge (Zhou *et al.* 2005a). However, as α increases, the effect of pipette size was found to be less significant (cf. Fig. 6.11(a) and Fig. 6.18(a)). This can be explained as follows. The higher α is, the larger the instantaneous stiffness $G(0)$ will be (cf. Table C.1). If $G(0)$ is higher, the stiffening effect associated with slippage will be more significant, which will help to reduce the slippage. Therefore, higher α will lead to smaller slippage, thus attenuating the effect of pipette size on B_{FE} and C_{FE}. This helps to account for the weak dependence of experimentally measured stiffness constant of fibroblasts on pipette size (cf. Fig. 6.14 and Fig. 6.20).

6.5.3 Comparison with others' work on FE simulation of micropipette aspiration using other rheological models

Finite element method has been previously applied to simulate the deformation of cells in micropipette aspiration using other rheological models. Maxwell liquid drop model has been applied within the FE analysis to simulate the micropipette aspiration of leukocytes (Dong *et al.* 1988; Dong *et al.* 1991; Dong and Skalak 1992). It was found that the model could fit the initial small deformation but in order to match the large deformation of the cells, the rheological parameters needed to be adjusted, which suggests that the Maxwell model is not suitable for modeling large deformation of cells (cf. Section 2.2.2.3). Drury and Dembo (1999; 2001) performed FE analysis of micropipette aspiration of leukocytes based on Newtonian liquid drop model. Although being able to qualitatively fit the large deformation of the cells, the model could not account for the initial rapid entry. It has also been found that a single model with a unique set of parameters could not fit all the creep behavior of cells under varying pipette diameter and suction pressure (Drury and Dembo 2001) (cf. Fig. 2.6 and Section 2.2.2.2).

Baaijens *et al.* (2005) performed finite element analysis of micropipette aspiration of chondrocytes based on the standard linear solid (SLS) model. It was shown that the creep deformation of a chondrocyte could be fitted by the model. However, the experimental data was taken every 7.5 s for a total time of 75 s. Note that starting time cannot be accurately 0 s but depends on the time resolution for pressure application and image acquisition. Thus, the time is only accurate from 7.5 to 75 s, which only spans 1 decade on log scale. On the other hand, it has been shown that the SLS model can fit power-law creep function for 1 ~ 2 decades of time on the log-log scale (Desprat *et al.* 2005) (also see Fig. 5.3). Therefore, the observation that the SLS model can fit the creep deformation of cells within a limited time span does not rule out the applicability of the power-law rheology model, which was found to fit the creep deformation of cells for more than 3 decades (Lenormand *et al.* 2004; Desprat *et al.* 2005).

In the current work, a finite element model was proposed based on the power-law rheology. This model, which approximates the power-law relaxation function with Prony-series expansion, is capable of representing the power-law rheology over 6 decades of time. Favorable agreement was achieved between simulation and experiments. A single set of rheological parameters ($G(\mathrm{t}) = 100t^{-0.387}$ Pa) was needed for matching three types of micropipette aspiration experiments on NIH 3T3 fibroblasts, namely creep tests at 100 Pa, ramp tests at 10/3 Pa/s and ramp tests at 5/6 Pa/s, all of which were performed using pipettes ranging from 7 to 10 μm in diameter (cf. Sections 6.4.2.5 and 6.4.3.3). This work thus provides further support to the applicability of the power-law rheology model to cells in the context of micropipette aspiration.

6.5.4 Potential application in studying mechanotransduction

Mechanotransduction is concerned with the transmission and distribution of mechanical signals and the conversion of these signals into biological and chemical responses in the cell (Wang *et al.* 1993; Ingber 1997; Ingber 2003; Orr *et al.* 2006; Vogel and Sheetz 2006). As pointed out by Humphrey (2001), Zhu et al. (2000) and others, the effect of the stress and/or strain may be reflected at the molecular level in the form of changes in macromolecular conformation and/or inter-atomic forces, which may elicit biochemical pathways.

In order to simulate mechanotransduction of a cell, it would be desirable to model all its molecules and their interactions realistically. However, such a molecular model is both beyond the computing capacity available today and probably unnecessary. One proposed strategy towards investigating mechanotransduction is to utilize a multi-scale approach to develop mechanical models that can predict the transduction of forces from cell level, through subcellular level, eventually down to protein scale (Guilak and Mow 2000; Tadmor *et al.* 2000; Phillips *et al.* 2002; Dupuy *et al.* 2005). This three-level hierarchical approach is illustrated in Fig. 6.21 (Lim *et al.* 2006; Vogel and Sheetz 2006). At level 1, a single cell is modeled with a continuum model. In response to a mechanical signal at the cell level, local stresses and strains in subcellular regions can then be calculated using FE simulation (Charras and Horton 2002a; Charras and Horton 2002b; Humphrey 2003; Charras *et al.* 2004). At level 2, the subcellular stress and strain is used to predict, through microstructural models (Onck *et al.* 2005), the local reorganization of cytoskeleton, which plays an important role in mechanotransduction (Wang *et al.* 1993; Maniotis *et al.* 1997; Janmey 1998; Forgacs *et al.* 2004; Geiger *et al.* 2006). At the third level, molecular dynamics simulation (Isralewitz et al. 2001; Gullingsrud and Schulten 2003) can be used to predict changes in protein conformation, such as protein unfolding (Khan and Sheetz 1997) and gating of mechanosensitive ion channels (Sukharev *et al.* 2001; Perozo *et al.* 2002; Martinac 2004; Wiggins and Phillips 2004), which may be directly related to biochemical pathways (Fig. 6.21). This way, prediction of causal relationships between mechanical signal and biological response can be achieved. Comparison between model prediction and experimental observations may lead to better understanding of the mechanisms of mechanotransduction.

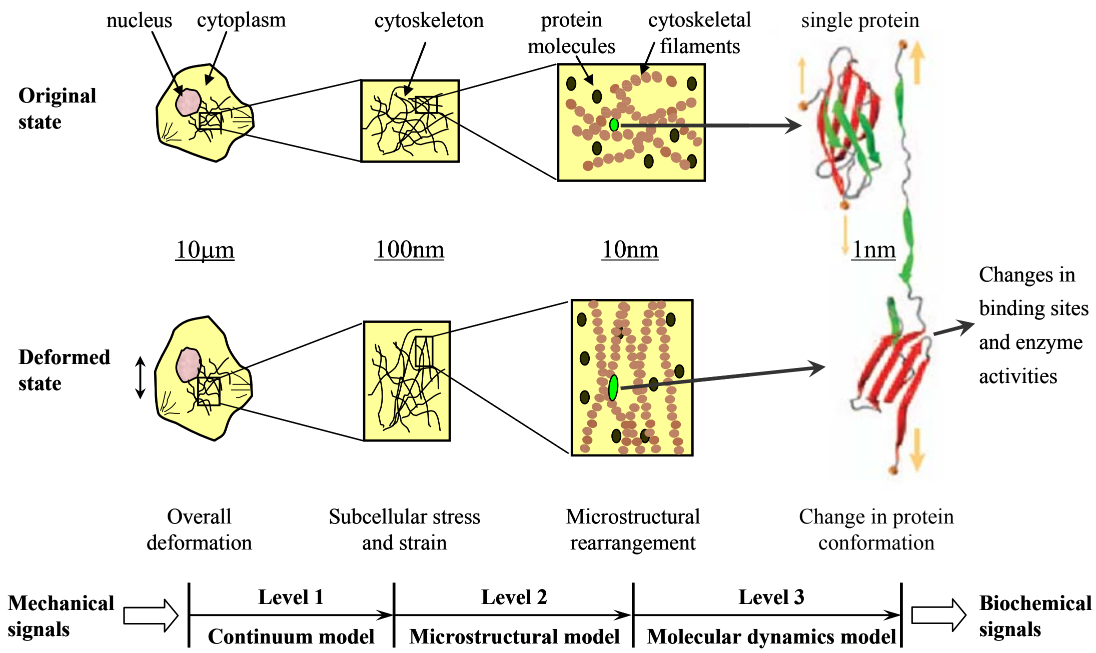
nucleus
cytoplasm
cytoskeleton
protein molecules
cytoskeletal filaments
single protein
Original state
10μm
100nm
10nm
1nm
Changes in binding sites and enzyme activities
Deformed state
Overall deformation
Subcellular stress and strain
Microstructural rearrangement
Change in protein conformation
Mechanical signals
Level 1
Continuum model
Level 2
Microstructural model
Level 3
Molecular dynamics model
Biochemical signals

Fig. 6.21. Three-level hierarchical approach to investigating mechanotransduction of single cells (Lim *et al.* 2006; Vogel and Sheetz 2006).

The widespread experimental evidence ranging from the whole cell, through cytoskeleton and organelles, to the nucleus supported the general applicability of the power-law rheology model in cell mechanics (Fabry *et al.* 2001a; Alcaraz *et al.* 2003; Lenormand *et al.* 2004; Yanai *et al.* 2004; Balland *et al.* 2005; Dahl *et al.* 2005; Desprat *et al.* 2005). The current work not only provided additional support to this model but also proposed an approach for implementing it in finite element analysis. A finite element model for cells based on power-law rheology, which needs to further account for structural heterogeneity and active forces of cells, may be useful in predicting the subcellular distribution of stress and strain (level 1 in Fig. 6.21) and thus contribute to the study of mechanotransduction of single cells (Lim *et al.* 2006; Vogel and Sheetz 2006).

Chapter 7 Conclusions and Future Work

This thesis focused on the rheological properties of cells. One of the main objectives was to test the power-law rheology hypothesis for suspended NIH 3T3 fibroblasts using micropipette aspiration. The other was to build a finite element model of cells based on the power-law rheology and to simulate the micropipette aspiration experiments.

7.1 Conclusions

The major contributions and findings of this thesis can be summarized as follows:

1. Pipette size was found to have a profound effect on cell deformation. The pressure-deformation relationship was measured with ramp tests. Pipettes smaller than ~ 5 μm in diameter exhibited nonlinear and inconsistent pressure-deformation relationship and thus are not suited for probing the bulk rheology of cells. On the other hand, large pipettes (7 ~ 10 μm in diameter) generally produced linear and consistent relationship and are more applicable for measuring the smeared rheology of cells.

2. The power-law rheology model was found to accurately fit the creep functions of suspended fibroblasts, which were measured with creep tests using large pipettes. This provided new support to this model for suspended cells.

3. Effect of cytoskeleton disruption on rheological properties was investigated. Disruption of actin filaments with cytochalasin D (2 μM) caused cells to appear softer but more elastic. In contrast, disruption of microtubules with high dosage of colchicine (1 mM) caused activation and stiffening of cells. The effect of 100 μM colchicine was similar but less pronounced.

4. A finite element model was proposed to simulate the power-law rheology of cells. The initial-boundary-value problem of micropipette aspiration was numerically simulated in the context of power-low rheology. Using consistent rheological properties, this model could predict the experimental observations obtained using both creep and ramp tests for suspended NIH 3T3 fibroblasts.

5. The finite element simulation revealed departure from the prediction of the half-space solution as a result of (i) finite cell radius with respect to pipette radius, (ii) large deformation and (iii) slippage. Pipette geometry and the power-law exponent of relaxation modulus of cells were found to influence the viscoelastic deformation of cells significantly. Approximate formulae were proposed based on simulation results, which allow direct interpretation of rheological properties of cells in micropipette aspiration.

6. In particular, the simulation indicated that the power-law exponent of relaxation modulus of cells is likely to be underestimated by using the elastic-viscoelastic correspondence principle, especially at large deformation. In addition, this exponent influences stress redistribution of cells during

micropipette aspiration and thus, can modulate the effect of pipette size on cell deformation.

7.2 Future work

The work in this thesis points to interesting new directions of cell mechanics which await deeper exploration. Thus, the future work can include the following:

1. The molecular and structural mechanism that underlies the pipette-size effect on cell deformation needs to be understood. In particular, why is blebbing more likely to occur with smaller pipettes than with larger ones under the same suction pressure? Does the mechanical force imposed by the micropipettes locally stimulate the contractile activity of the acto-myosin network (Hagmann *et al.* 1999; Charras *et al.* 2005)? Answering these may help to understand the biological response of cells to mechanical forces.

2. The experimental methodology proposed in the current work may be extended to study the pipette-size effect and to quantify the rheological properties for other cell types. This may not only identify common features but also reveal cell-type specific characteristics associated with the different phenotypes or genotypes.

3. The fundamental physical law that governs cell rheology needs to be further explored. The widespread experimental results on a wide range of cell types supported the power-law rheology model. This suggests that a common mechanism may underlie the physical organization of the protein scaffold of eukaryotic animal cells. An emerging hypothesis is that of a soft glassy

material (Sollich *et al.* 1997; Fabry *et al.* 2001a). Deeper insights into the molecular events involved in cytoskeletal deformation will be needed for further exploration of this hypothesis.

4. Simulation of mechanotransduction of cells is worthy of being pursued. An accurate continuum model for single cells may contribute to the study of mechanotransduction by predicting the subcellular distribution of stress and strain in response to mechanical stimuli. To this end, the heterogeneity of cells in terms of subcellular regions and organelles needs to be further characterized and active force within cells needs to be measured.

5. The experimental methodology and finite element model proposed in this thesis may be used to evaluate the effect of drug treatments or diseases on the rheological properties of cells. This might contribute to better understanding, diagnosis, and treatment of relevant diseases such as cancer, malaria, arthritis and some skin diseases (Nash *et al.* 1989; Ward *et al.* 1991; Fuchs and Cleveland 1998; Trickey *et al.* 2000; Guck *et al.* 2005; Suresh *et al.* 2005).

References

ABAQUS, 2003a. ABAQUS Analysis User's Manual (version 6.4), ABAQUS, Inc., USA.

ABAQUS, 2003b. ABAQUS Theory Manual (version 6.4), ABAQUS, Inc., USA.

Alberts, B., A. Johnson, J. Lewis, M. Raff, K. Roberts, P. Walter, 2002. Molecular biology of the cell (4th Edition). New York, Garland Science Publishing.

Albrecht-Buehler, G., 1987. Role of cortical tension in fibroblast shape and movement. Cell Motil Cytoskeleton 7(1), 54-67.

Alcaraz, J., L. Buscemi, M. Grabulosa, X. Trepat, B. Fabry, R. Farre, D. Navajas, 2003. Microrheology of human lung epithelial cells measured by atomic force microscopy. Biophys J 84(3), 2071-9.

Anderson, D. C., L. J. Wible, B. J. Hughes, C. W. Smith, B. R. Brinkley, 1982. Cytoplasmic microtubules in polymorphonuclear leukocytes: effects of chemotactic stimulation and colchicine. Cell 31(3 Pt 2), 719-29.

Andreu, J. M., S. N. Timasheff, 1982. Tubulin bound to colchicine forms polymers different from microtubules. Proc Natl Acad Sci U S A 79(22), 6753-6.

Baaijens, F. P. T., W. R. Trickey, T. A. Laursen, F. Guilak, 2005. Large Deformation Finite Element Analysis of Micropipette Aspiration to Determine the Mechanical Properties of the Chondrocyte. Annals of Biomedical Engineering 33(4), 492-499.

Bagge, U., R. Skalak, R. Attefors (1977). Granulocyte rheology: experimental studies in an in-vitro microflow system. In Adv. Microcirc. **7:** 29-48.

Balland, M., A. Richert, F. Gallet, 2005. The dissipative contribution of myosin II in the cytoskeleton dynamics of myoblasts. Eur Biophys J 34(3), 255-61.

Band, R. P., A. C. Burton, 1964. Mechanical properties of the red cell membrane. I. Membrane stiffness and intracellular pressure. Biophys J 4, 115.

Bao, G., S. Suresh, 2003. Cell and molecular mechanics of biological materials. Nature Materials 2(11), 715-725.

Bathe, K. J., 1996. Finite Element Procedures (3rd), Pretice-Hall.

Bausch, A. R., W. Moller, E. Sackmann, 1999. Measurement of Local Viscoelasticity and Forces in Living Cells by Magnetic Tweezers. Biophys. J. 76(1), 573-579.

Bausch, A. R., F. Ziemann, A. A. Boulbitch, K. Jacobson, E. Sackmann, 1998. Local Measurements of Viscoelastic Parameters of Adherent Cell Surfaces by Magnetic Bead Microrheometry. Biophys. J. 75(4), 2038-2049.

Beil, M., A. Micoulet, G. von Wichert, S. Paschke, P. Walther, M. B. Omary, P. P. Van Veldhoven, U. Gern, E. Wolff-Hieber, J. Eggermann, J. Waltenberger, G. Adler, J. Spatz, T. Seufferlein, 2003. Sphingosylphosphorylcholine regulates keratin network architecture and visco-elastic properties of human cancer cells. Nat Cell Biol 5(9), 803-11.

Bilodeau, G. G., 1992. Regular Pyramid Punch Problem. Journal of Applied Mechanics 59(3), 519-523.

Bird, R. B., R. C. Armstrong, O. Hassager, 1987. Dynamics of Polymeric Liquids. New York, Wiley.

Boal, D., 2002. Mechanics of the Cell, Cambridge University Press.

Boey, S. K., D. H. Boal, D. E. Discher, 1998. Simulations of the erythrocyte cytoskeleton at large deformation. I. Microscopic models. Biophys. J. 75(3), 1573-1583.

Boudreau, N., M. J. Bissell, 1998. Extracellular matrix signaling: integration of form and function in normal and malignant cells. Current Opinion in Cell Biology 10(5), 640-646.

Burridge, K., T. Kelly, P. Mangeat, 1982. Nonerythrocyte spectrins: actin-membrane attachment proteins occurring in many cell types. J Cell Biol 95(2 Pt 1), 478-86.

Bursac, P., G. Lenormand, B. Fabry, M. Oliver, D. A. Weitz, V. Viasnoff, J. P. Butler, J. J. Fredberg, 2005. Cytoskeletal remodelling and slow dynamics in the living cell. Nat Mater.

Buschmann, M. D., Y. A. Gluzband, A. J. Grodzinsky, E. B. Hunziker, 1995. Mechanical compression modulates matrix biosynthesis in chondrocyte/agarose culture. J Cell Sci 108, 1497-508.

Buxbaum, R. E., T. Dennerll, S. Weiss, S. R. Heidemann, 1987. F-actin and microtubule suspensions as indeterminate fluids. Science 235(4795), 1511-4.

Charras, G. T., M. A. Horton, 2002a. Determination of cellular strains by combined atomic force microscopy and finite element modeling. Biophys J 83(2), 858-79.

Charras, G. T., M. A. Horton, 2002b. Single cell mechanotransduction and its modulation analyzed by atomic force microscope indentation. Biophys J 82(6), 2970-81.

Charras, G. T., B. A. Williams, S. M. Sims, M. A. Horton, 2004. Estimating the sensitivity of mechanosensitive ion channels to membrane strain and tension. Biophys J 87(4), 2870-84.

Charras, G. T., J. C. Yarrow, M. A. Horton, L. Mahadevan, T. J. Mitchison, 2005. Non-equilibration of hydrostatic pressure in blebbing cells. Nature 435(7040), 365-9.

Chen, C. S., M. Mrksich, S. Huang, G. M. Whitesides, D. E. Ingber, 1997. Geometric Control of Cell Life and Death. Science, New Series 276(5317), 1425-1428.

Chien, S., 2003. Molecular and mechanical bases of focal lipid accumulation in arterial wall. Prog Biophys Mol Biol 83(2), 131-51.

Cooke, B. M., N. Mohandas, R. L. Coppell, 2001. The malaria-infected red blood cell: Structural and functional changes. Advances in Parasitology 50, 1-86.

Coughlin, M. F., D. Stamenovic, 2003. A Prestressed Cable Network Model of the Adherent Cell Cytoskeleton. Biophys. J. 84(2), 1328-1336.

Cowin, S. C., 2002. Mechanosensation and fluid transport in living bone. J Musculoskelet Neuronal Interact 2(3), 256-60.

Crick, F. H. C., A. F. W. Hughes, 1950. The physical properties of cytoplasm: a study by means of the magnetic particle method. Part I. Experimental. Experimental Cell Research 1, 37-80.

Cunningham, C., 1995. Actin polymerization and intracellular solvent flow in cell surface blebbing. J. Cell Biol. 129(6), 1589-1599.

Dahl, K. N., A. J. Engler, J. D. Pajerowski, D. E. Discher, 2005. Power-law rheology of isolated nuclei with deformation mapping of nuclear substructures. Biophys J 89(4), 2855-64.

Danowski, B. A., 1989. Fibroblast contractility and actin organization are stimulated by microtubule inhibitors. J Cell Sci 93 (Pt 2), 255-66.

Desprat, N., A. Richert, J. Simeon, A. Asnacios, 2005. Creep Function of a Single Living Cell. Biophys. J. 88(3), 2224-2233.

Dinh, A. T., C. Pangarkar, T. Theofanous, S. Mitragotri, 2006. Theory of Spatial Patterns of Intracellular Organelles. Biophys J.

Discher, D. E., P. Janmey, Y. L. Wang, 2005. Tissue cells feel and respond to the stiffness of their substrate. Science 310(5751), 1139-43.

Djordjevic, V. D., J. Jaric, B. Fabry, J. J. Fredberg, D. Stamenovic, 2003. Fractional derivatives embody essential features of cell rheological behavior. Ann Biomed Eng 31(6), 692-9.

Dondorp, A. M., E. Pongponratn, N. J. White, 2004. Reduced microcirculatory flow in severe falciparum malaria: pathophysiology and electron-microscopic pathology. Acta Trop 89(3), 309-17.

Dong, C., R. Skalak, 1992. Leukocyte deformability: finite element modeling of large viscoelastic deformation. J Theor Biol 158(2), 173-93.

Dong, C., R. Skalak, K. L. Sung, 1991. Cytoplasmic rheology of passive neutrophils. Biorheology 28(6), 557-67.

Dong, C., R. Skalak, K. L. Sung, G. W. Schmid-Schonbein, S. Chien, 1988. Passive deformation analysis of human leukocytes. J Biomech Eng 110(1), 27-36.

Drury, J. L., M. Dembo, 1999. Hydrodynamics of Micropipette Aspiration. Biophys. J. 76(1), 110-128.

Drury, J. L., M. Dembo, 2001. Aspiration of Human Neutrophils: Effects of Shear Thinning and Cortical Dissipation. Biophys. J. 81(6), 3166-3177.

Dupuy, L. M., E. B. Tadmor, R. E. Miller, R. Phillips, 2005. Finite-temperature quasicontinuum: Molecular dynamics without all the atoms. Physical Review Letters 95(6).

Elson, E. L., 1988. Cellular mechanics as an indicator of cytoskeletal structure and function. Annu Rev Biophys Biophys Chem 17, 397-430.

Enomoto, T., 1996. Microtubule disruption induces the formation of actin stress fibers and focal adhesions in cultured cells: possible involvement of the rho signal cascade. Cell Struct Funct 21(5), 317-26.

Evans, E., B. Kukan, 1984. Passive material behavior of granulocytes based on large deformation and recovery after deformation tests. Blood 64(5), 1028-1035.

Evans, E., A. Yeung, 1989. Apparent viscosity and cortical tension of blood granulocytes determined by micropipet aspiration. Biophys. J. 56(1), 151-160.

Evans, E. A., 1973. New membrane concept applied to the analysis of fluid shear- and micropipette-deformed red blood cells. Biophys J 13(9), 941-54.

Fabry, B., J. J. Fredberg, 2003. Remodeling of the airway smooth muscle cell: are we built of glass? Respir Physiol Neurobiol 137(2-3), 109-24.

Fabry, B., G. N. Maksym, J. P. Butler, M. Glogauer, D. Navajas, J. J. Fredberg, 2001a. Scaling the microrheology of living cells. Phys Rev Lett 87(14), 148102.

Fabry, B., G. N. Maksym, J. P. Butler, M. Glogauer, D. Navajas, N. A. Taback, E. J. Millet, J. J. Fredberg, 2003. Time scale and other invariants of integrative mechanical behavior in living cells. Phys Rev E Stat Nonlin Soft Matter Phys 68(4 Pt 1), 041914.

Fabry, B., G. N. Maksym, S. A. Shore, P. E. Moore, R. A. Panettieri, Jr., J. P. Butler, J. J. Fredberg, 2001b. Selected contribution: time course and heterogeneity of contractile responses in cultured human airway smooth muscle cells. J Appl Physiol 91(2), 986-94.

Fernandez, P., P. A. Pullarkat, A. Ott, 2006. A Master Relation Defines the Nonlinear Viscoelasticity of Single Fibroblasts. Biophys. J. 90(10), 3796-3805.

Ferry, J. D., 1980. Viscoelastic Properties of Polymers, 3rd ed. New York, Wiley.

Findley, W. N., J. S. Lai, K. Onaran, 1976. Creep and relaxation of nonlinear viscoelastic materials, with an introduction to linear viscoelasticity. New York, Dover Publications, Inc.

Flugge, W., 1967. Viscoelasticity. Waltham, Blaisdell Publishing Company.

Forgacs, G., S. H. Yook, P. A. Janmey, H. Jeong, C. G. Burd, 2004. Role of the cytoskeleton in signaling networks. J Cell Sci 117(Pt 13), 2769-75.

Fuchs, E., D. W. Cleveland, 1998. A structural scaffolding of intermediate filaments in health and disease. Science 279(5350), 514-9.

Fung, Y. C., 1965. Foundations of solid mechanics. Englewood Cliffs, N.J., Prentice-Hall Inc.

Fung, Y. C., 1993. Biomechanics: Mechanical Properties of Living Tissues, 2nd Edition. New York, Springer-Verlag.

Gardel, M. L., F. Nakamura, J. H. Hartwig, J. C. Crocker, T. P. Stossel, D. A. Weitz, 2006. Prestressed F-actin networks cross-linked by hinged filamins replicate mechanical properties of cells. Proc Natl Acad Sci U S A 103(6), 1762-7.

Geiger, R. C., W. Taylor, M. R. Glucksberg, D. A. Dean, 2006. Cyclic stretch-induced reorganization of the cytoskeleton and its role in enhanced gene transfer. Gene Ther 13(8), 725-31.

Glenister, F. K., R. L. Coppel, A. F. Cowman, N. Mohandas, B. M. Cooke, 2002. Contribution of parasite proteins to altered mechanical properties of malaria-infected red blood cells. Blood 99(3), 1060-1063.

Guck, J., R. Ananthakrishnan, H. Mahmood, T. J. Moon, C. C. Cunningham, J. Kas, 2001. The optical stretcher: a novel laser tool to micromanipulate cells. Biophys J 81(2), 767-84.

Guck, J., S. Schinkinger, B. Lincoln, F. Wottawah, S. Ebert, M. Romeyke, D. Lenz, H. M. Erickson, R. Ananthakrishnan, D. Mitchell, J. Kas, S. Ulvick, C. Bilby, 2005. Optical deformability as an inherent cell marker for testing malignant transformation and metastatic competence. Biophys J 88(5), 3689-98.

Guilak, F., D. L. Butler, S. A. Goldstein, D. Mooney, Eds. (2003). Functional tissue engineering. New York, Springer.

Guilak, F., W. R. Jones, H. P. Ting-Beall, G. M. Lee, 1999. The deformation behavior and mechanical properties of chondrocytes in articular cartilage. Osteoarthritis and Cartilage 7(1), 59-70.

Guilak, F., V. C. Mow, 2000. The mechanical environment of the chondrocyte: a biphasic finite element model of cell-matrix interactions in articular cartilage. Journal of Biomechanics 33(12), 1663-1673.

Guilak, F., J. R. Tedrow, R. Burgkart, 2000. Viscoelastic Properties of the Cell Nucleus. Biochemical and Biophysical Research Communications 269(3), 781-786.

Gullingsrud, J., K. Schulten, 2003. Gating of MscL Studied by Steered Molecular Dynamics. Biophys. J. 85(4), 2087-2099.

Hagmann, J., M. M. Burger, D. Dagan, 1999. Regulation of plasma membrane blebbing by the cytoskeleton. J Cell Biochem 73(4), 488-99.

Haider, M. A., F. Guilak, 2000. An axisymmetric boundary integral model for incompressible linear viscoelasticity: application to the micropipette aspiration contact problem. J Biomech Eng 122(3), 236-44.

Haider, M. A., F. Guilak, 2002. An axisymmetric boundary integral model for assessing elastic cell properties in the micropipette aspiration contact problem. J Biomech Eng 124(5), 586-95.

Harding, J. W., I. N. Sneddon, 1945. The elastic stresses produced by the indentation of the plane surface of a semi-infinite elastic solid by a rigid punch. Proc. Cambridge Philos. Soc. 41, 16-26.

Henon, S., G. Lenormand, A. Richert, F. Gallet, 1999. A New Determination of the Shear Modulus of the Human Erythrocyte Membrane Using Optical Tweezers. Biophys. J. 76(2), 1145-1151.

Hochmuth, R. M., 2000. Micropipette aspiration of living cells. Journal of Biomechanics 33(1), 15-22.

Hochmuth, R. M., H. P. Ting-Beall, B. B. Beaty, D. Needham, R. Tran-Son-Tay, 1993. Viscosity of passive human neutrophils undergoing small deformations. Biophys. J. 64(5), 1596-1601.

Hoh, J. H., C. A. Schoenenberger, 1994. Surface morphology and mechanical properties of MDCK monolayers by atomic force microscopy. J Cell Sci 107(5), 1105-1114.

Huang, S., D. E. Ingber, 1999. The structural and mechanical complexity of cell-growth control. Nat Cell Biol 1(5), E131-8.

Humphrey, J. D., 2001. Stress, strain, and mechanotransduction in cells. J Biomech Eng 123(6), 638-41.

Humphrey, J. D., 2003. Continuum biomechanics of soft biological tissues. Proceedings of the Royal Society of London Series A - Mathematical Physical and Engineering Sciences 459(2029), 3-46.

Ingber, D. E., 1997. Tensegrity: the architectural basis of cellular mechanotransduction. Annual Review of Physiology 59(1), 575-599.

Ingber, D. E., 2003. Tensegrity II. How structural networks influence cellular information processing networks. J Cell Sci 116(8), 1397-1408.

Isralewitz, B., J. Baudry, J. Gullingsrud, D. Kosztin, K. Schulten, 2001. Steered molecular dynamics investigations of protein function. J Mol Graph Model 19(1), 13-25.

Janmey, P. A., 1998. The cytoskeleton and cell signaling: component localization and mechanical coupling. Physiol Rev 78(3), 763-81.

Janmey, P. A., S. Hvidt, J. Kas, D. Lerche, A. Maggs, E. Sackmann, M. Schliwa, T. P. Stossel, 1994. The mechanical properties of actin gels. Elastic modulus and filament motions. J Biol Chem 269(51), 32503-13.

Jeong, H., B. Tombor, R. Albert, Z. N. Oltvai, A. L. Barabasi, 2000. The large-scale organization of metabolic networks. Nature 407(6804), 651-4.

Jones, W. R., G. M. Lee, S. S. Kelley, F. Guilak, 1999a. Viscoelastic properties of chondrocytes from normal and osteoarthritic human cartilage. 45th Trans. Annu. Meet.--Orthop. Res. Soc. 24, 157.

Jones, W. R., P. H. Ting-Beall, G. M. Lee, S. S. Kelley, R. M. Hochmuth, F. Guilak, 1999b. Alterations in the Young's modulus and volumetric properties of chondrocytes isolated from normal and osteoarthritic human cartilage. Journal of Biomechanics 32(2), 119-127.

Kamm, R. D., 2002. Cellular fluid mechanics. Annual Review of Fluid Mechanics 34(1), 211-232.

Kaul, D. K., M. E. Fabry, 2004. In vivo studies of sickle red blood cells. Microcirculation 11(2), 153-65.

Keller, H. U., A. Naef, A. Zimmermann, 1984. Effects of colchicine, vinblastine and nocodazole on polarity, motility, chemotaxis and cAMP levels of human polymorphonuclear leukocytes. Experimental Cell Research 153(1), 173-185.

Khan, S., M. P. Sheetz, 1997. Force effects on biochemical kinetics. Annu Rev Biochem 66, 785-805.

Kjoller, L., A. Hall, 1999. Signaling to Rho GTPases. Exp Cell Res 253(1), 166-79.

Koay, E. J., A. C. Shieh, K. A. Athanasiou, 2003. Creep indentation of single cells. J Biomech Eng 125(3), 334-41.

Laudadio, R. E., E. J. Millet, B. Fabry, S. S. An, J. P. Butler, J. J. Fredberg, 2005. Rat airway smooth muscle cell during actin modulation: rheology and glassy dynamics. Am J Physiol Cell Physiol 289(6), C1388-95.

Lenormand, G., J. J. Fredberg, 2006. Deformability, dynamics, and remodeling of cytoskeleton of the adherent living cell. Biorheology 43(1), 1-30.

Lenormand, G., E. Millet, B. Fabry, J. Butler, J. Fredberg, 2004. Linearity and time-scale invariance of the creep function in living cells. J. R. Soc. Interface 1, 91-97.

Li, J., M. Dao, C. T. Lim, S. Suresh, 2005. Spectrin-level modeling of the cytoskeleton and optical tweezers stretching of the erythrocyte. Biophys J 88(5), 3707-19.

Lim, C. T., M. Dao, S. Suresh, C. H. Sow, K. T. Chew, 2004. Large deformation of living cells using laser traps. Acta Materialia 52(7), 1837-1845. (Also see Corrigendum at Acta Materialia 0052 (2004) 4065-4066).

Lim, C. T., E. H. Zhou, S. T. Quek, 2006. Mechanical models for living cells - a review. Journal of Biomechanics 39, 195-216.

Lo, C. M., J. Ferrier, 1999. Electrically measuring viscoelastic parameters of adherent cell layers under controlled magnetic forces. Eur Biophys J 28(2), 112-8.

Mahaffy, R. E., S. Park, E. Gerde, J. Kas, C. K. Shih, 2004. Quantitative analysis of the viscoelastic properties of thin regions of fibroblasts using atomic force microscopy. Biophys J 86(3), 1777-93.

Mahaffy, R. E., C. K. Shih, F. C. MacKintosh, J. Kas, 2000. Scanning probe-based frequency-dependent microrheology of polymer gels and biological cells. Phys Rev Lett 85(4), 880-3.

Maksym, G. N., B. Fabry, J. P. Butler, D. Navajas, D. J. Tschumperlin, J. D. Laporte, J. J. Fredberg, 2000. Mechanical properties of cultured human airway smooth muscle cells from 0.05 to 0.4 Hz. J Appl Physiol 89(4), 1619-32.

Maniotis, A. J., C. S. Chen, D. E. Ingber, 1997. Demonstration of mechanical connections between integrins, cytoskeletal filaments, and nucleoplasm that stabilize nuclear structure. PNAS 94(3), 849-854.

Martinac, B., 2004. Mechanosensitive ion channels: molecules of mechanotransduction. J Cell Sci 117(Pt 12), 2449-60.

Mijailovich, S. M., M. Kojic, M. Zivkovic, B. Fabry, J. J. Fredberg, 2002. A finite element model of cell deformation during magnetic bead twisting. J Appl Physiol 93(4), 1429-36.

Miller, L. H., D. I. Baruch, K. Marsh, O. K. Doumbo, 2002. The pathogenic basis of malaria. Nature 415(6872), 673-9.

Mitchison, J. M., M. M. Swann, 1954. The mechanical properties of the cell surface I. The cell elastimeter. J. Exp. Biol. 31(443-460).

Mitchison, T. J., 1995. Evolution of a dynamic cytoskeleton. Philos Trans R Soc Lond B Biol Sci 349(1329), 299-304.

Miyazaki, H., Y. Hasegawa, K. Hayashi, 2000. A newly designed tensile tester for cells and its application to fibroblasts. Journal Of Biomechanics 33(1), 97-104.

Mizutani, T., H. Haga, K. Kawabata, 2004. Cellular stiffness response to external deformation: tensional homeostasis in a single fibroblast. Cell Motil Cytoskeleton 59(4), 242-8.

Mow, V., F. Guilak, R. Tran-Son-Tay, R. Hochmuth, Eds. (1994). Cell Mechanics and Cellular Engineering. New York, Springer-Verlag.

Munevar, S., Y. Wang, M. Dembo, 2001. Traction force microscopy of migrating normal and H-ras transformed 3T3 fibroblasts. Biophys J 80(4), 1744-57.

Nagayama, K., Y. Nagano, M. Sato, T. Matsumoto, 2006. Effect of actin filament distribution on tensile properties of smooth muscle cells obtained from rat thoracic aortas. J Biomech 39(2), 293-301.

Nash, G. B., E. Obrien, E. C. Gordonsmith, J. A. Dormandy, 1989. Abnormalities in the Mechanical-Properties of Red Blood-Cells Caused by Plasmodium-Falciparum. Blood 74(2), 855-861.

Needham, D., R. M. Hochmuth, 1990. Rapid flow of passive neutrophils into a 4 microns pipet and measurement of cytoplasmic viscosity. J Biomech Eng 112(3), 269-76.

Needham, D., R. M. Hochmuth, 1992. A sensitive measure of surface stress in the resting neutrophil. Biophys. J. 61(6), 1664-1670.

NIST/SEMATECH, 2005. e-Handbook of Statistical Methods, http://www.itl.nist.gov/div898/handbook/.

Omelchenko, T., J. M. Vasiliev, I. M. Gelfand, H. H. Feder, E. M. Bonder, 2002. Mechanisms of polarization of the shape of fibroblasts and epitheliocytes: Separation of the roles of microtubules and Rho-dependent actin-myosin contractility. Proc Natl Acad Sci U S A 99(16), 10452-7.

Onck, P. R., T. Koeman, T. van Dillen, E. van der Giessen, 2005. Alternative explanation of stiffening in cross-linked semiflexible networks. Phys Rev Lett 95(17), 178102.

Orr, A. W., B. P. Helmke, B. R. Blackman, M. A. Schwartz, 2006. Mechanisms of mechanotransduction. Dev Cell 10(1), 11-20.

Pangarkar, C., A. T. Dinh, S. Mitragotri, 2005. Dynamics and spatial organization of endosomes in mammalian cells. Phys Rev Lett 95(15), 158101.

Perozo, E., D. M. Cortes, P. Sompornpisut, A. Kloda, B. Martinac, 2002. Open channel structure of MscL and the gating mechanism of mechanosensitive channels. Nature(418), 942 - 948.

Peterman, E. J., F. Gittes, C. F. Schmidt, 2003. Laser-induced heating in optical traps. Biophys J 84(2 Pt 1), 1308-16.

Petersen, N. O., W. B. McConnaughey, E. L. Elson, 1982. Dependence of Locally Measured Cellular Deformability on Position on the Cell, Temperature, and Cytochalasin B. PNAS 79(17), 5327-5331.

Phillips, R., M. Dittrich, K. Schulten, 2002. Quasicontinuum representations of atomic-scale mechanics: From proteins to dislocations. Annual Review of Materials Research 32, 219-233.

Pollack, G. H., 2001. Cells, Gels and the Engines of Life. Seattle, Ebner and Sons Publishers.

Pritz, T., 1996. Analysis of four-parameter fractional derivative model of real solid materials. Journal of Sound and Vibration 195(1), 103-115.

Puig-De-Morales, M., M. Grabulosa, J. Alcaraz, J. Mullol, G. N. Maksym, J. J. Fredberg, D. Navajas, 2001. Measurement of cell microrheology by magnetic twisting cytometry with frequency domain demodulation. J Appl Physiol 91(3), 1152-1159.

Puig-De-Morales, M., E. Millet, B. Fabry, D. Navajas, N. Wang, J. P. Butler, J. J. Fredberg, 2004. Cytoskeletal mechanics in adherent human airway smooth muscle cells: probe specificity and scaling of protein-protein dynamics. Am J Physiol Cell Physiol 287(3), C643-54.

Rentsch, P. S., H. Keller, 2000. Suction pressure can induce uncoupling of the plasma membrane from cortical actin. Eur J Cell Biol 79(12), 975-81.

Richelme, F., A. M. Benoliel, P. Bongrand, 2000. Dynamic study of cell mechanical and structural responses to rapid changes of calcium level. Cell Motil Cytoskeleton 45(2), 93-105.

Rosenbluth, M. J., W. A. Lam, D. A. Fletcher, 2006. Force microscopy of nonadherent cells: a comparison of leukemia cell deformability. Biophys J 90(8), 2994-3003.

Rotsch, C., M. Radmacher, 2000. Drug-induced changes of cytoskeletal structure and mechanics in fibroblasts: an atomic force microscopy study. Biophys J 78(1), 520-35.

Saez, A., A. Buguin, P. Silberzan, B. Ladoux, 2005. Is the mechanical activity of epithelial cells controlled by deformations or forces? Biophys J 89(6), L52-4.

Satcher, R. L., Jr., C. F. Dewey, Jr., 1996. Theoretical estimates of mechanical properties of the endothelial cell cytoskeleton. Biophys J 71(1), 109-18.

Sato, M., M. J. Levesque, R. M. Nerem, 1987a. An application of the micropipette technique to the measurement of the mechanical properties of cultured bovine aortic endothelial cells. J Biomech Eng 109(1), 27-34.

Sato, M., M. J. Levesque, R. M. Nerem, 1987b. Micropipette aspiration of cultured bovine aortic endothelial cells exposed to shear stress. Arteriosclerosis 7(3), 276-86.

Sato, M., N. Ohshima, R. M. Nerem, 1996. Viscoelastic properties of cultured porcine aortic endothelial cells exposed to shear stress. Journal of Biomechanics 29(4), 461-467.

Sato, M., D. P. Theret, L. T. Wheeler, N. Ohshima, R. M. Nerem, 1990. Application of the micropipette technique to the measurement of cultured porcine aortic endothelial cell viscoelastic properties. J Biomech Eng 112(3), 263-8.

Schmid-Schonbein, G. W., T. Kosawada, R. Skalak, S. Chien, 1995. Membrane model of endothelial cells and leukocytes. A proposal for the origin of a cortical stress. J Biomech Eng 117(2), 171-8.

Schmid-Schonbein, G. W., K. L. Sung, H. Tozeren, R. Skalak, S. Chien, 1981. Passive mechanical properties of human leukocytes. Biophys. J. 36(1), 243-256.

Schwartz, M. A., M. H. Ginsberg, 2002. Networks and crosstalk: integrin signalling spreads. Nature Cell Biology 4(4), E65-E68.

Shin, D., K. Athanasiou, 1999. Cytoindentation for obtaining cell biomechanical properties. J Orthop Res 17(6), 880-90.

Smith, B. A., B. Tolloczko, J. G. Martin, P. Grutter, 2005. Probing the viscoelastic behavior of cultured airway smooth muscle cells with atomic force microscopy: stiffening induced by contractile agonist. Biophys J 88(4), 2994-3007.

Sollich, P., 1998. Rheological constitutive equation for a model of soft glassy materials. Physical Review E 58(1), 738-759.

Sollich, P., F. Lequeux, P. Hebraud, M. E. Cates, 1997. Rheology of Soft Glassy Materials. Physical Review Letters 78(10), 2020 - 2023.

Stamenovic, D., M. F. Coughlin, 1999. The role of prestress and architecture of the cytoskeleton and deformability of cytoskeletal filaments in mechanics of adherent cells: a quantitative analysis. J Theor Biol 201(1), 63-74.

Stamenovic, D., J. J. Fredberg, N. Wang, J. P. Butler, D. E. Ingber, 1996. A microstructural approach to cytoskeletal mechanics based on tensegrity. J Theor Biol 181(2), 125-36.

Stamenovic, D., D. E. Ingber, 2002. Models of cytoskeletal mechanics of adherent cells. Biomech Model Mechanobiol 1(1), 95-108.

Stamenovic, D., B. Suki, B. Fabry, N. Wang, J. J. Fredberg, 2004. Rheology of airway smooth muscle cells is associated with cytoskeletal contractile stress. J Appl Physiol 96(5), 1600-5.

Sukharev, S., M. Betanzos, C. S. Chiang, H. R. Guy, 2001. The gating mechanism of the large mechanosensitive channel MscL. Nature(409), 720-724.

Suresh, S., J. Spatz, J. P. Mills, A. Micoulet, M. Dao, C. T. Lim, M. Beil, T. Seufferlein, 2005. Connections between single-cell biomechanics and human disease states: gastrointestinal cancer and malaria. Acta Biomaterialia 1, 15-30.

Tadmor, E. B., R. Phillips, M. Ortiz, 2000. Hierarchical modeling in the mechanics of materials. International Journal of Solids and Structures 37(1-2), 379-389.

Theret, D. P., M. J. Levesque, M. Sato, R. M. Nerem, L. T. Wheeler, 1988. The application of a homogeneous half-space model in the analysis of endothelial cell micropipette measurements. J Biomech Eng 110(3), 190-9.

Thoumine, O., O. Cardoso, J. J. Meister, 1999. Changes in the mechanical properties of fibroblasts during spreading: a micromanipulation study. Eur Biophys J 28(3), 222-34.

Thoumine, O., A. Ott, 1997a. Comparison of the mechanical properties of normal and transformed fibroblasts. Biorheology 34(4-5), 309-26.

Thoumine, O., A. Ott, 1997b. Time scale dependent viscoelastic and contractile regimes in fibroblasts probed by microplate manipulation. J Cell Sci 110(17), 2109-2116.

Tran-Son-Tay, R., T. F. Kirk, 3rd, D. V. Zhelev, R. M. Hochmuth, 1994a. Numerical simulation of the flow of highly viscous drops down a tapered tube. J Biomech Eng 116(2), 172-7.

Tran-Son-Tay, R., D. Needham, A. Yeung, R. M. Hochmuth, 1991. Time-dependent recovery of passive neutrophils after large deformation. Biophys. J. 60(4), 856-866.

Tran-Son-Tay, R., H. P. Ting-Beall, D. V. Zhelev, R. M. Hochmuth (1994b). Viscous behaviour of leukocytes. In Cellular Mechanics and Cellular Engineering. V. C. Mow, F. Guilak, R. Tran-Son-Tay and R. M. Hochmuth, Springer-Verlag**:** 22-32.

Trepat, X., M. Grabulosa, F. Puig, G. N. Maksym, D. Navajas, R. Farre, 2004. Viscoelasticity of human alveolar epithelial cells subjected to stretch. Am J Physiol Lung Cell Mol Physiol 287(5), L1025-34.

Trickey, W. R., G. M. Lee, F. Guilak, 2000. Viscoelastic properties of chondrocytes from normal and osteoarthritic human cartilage. J Orthop Res 18(6), 891-8.

Trickey, W. R., T. P. Vail, F. Guilak, 2004. The role of the cytoskeleton in the viscoelastic properties of human articular chondrocytes. J Orthop Res 22(1), 131-9.

Tsai, M. A., R. S. Frank, R. E. Waugh, 1993. Passive mechanical behavior of human neutrophils: power-law fluid. Biophys. J. 65(5), 2078-2088.

Tsai, M. A., R. E. Waugh, P. C. Keng, 1998. Passive Mechanical Behavior of Human Neutrophils: Effects of Colchicine and Paclitaxel. Biophys. J. 74(6), 3282-3291.

Tseng, Y., T. P. Kole, D. Wirtz, 2002. Micromechanical mapping of live cells by multiple-particle-tracking microrheology. Biophys J 83(6), 3162-76.

Uehata, M., T. Ishizaki, H. Satoh, T. Ono, T. Kawahara, T. Morishita, H. Tamakawa, K. Yamagami, J. Inui, M. Maekawa, S. Narumiya, 1997. Calcium sensitization of smooth muscle mediated by a Rho-associated protein kinase in hypertension. Nature 389(6654), 990-4.

Van Vliet, K. J., G. Bao, S. Suresh, 2003. The biomechanics toolbox: experimental approaches for living cells and biomolecules. Acta Materialia 51(19), 5881-5905.

Vogel, V., M. Sheetz, 2006. Local force and geometry sensing regulate cell functions. Nature Reviews Molecular Cell Biology 7(4), 265-275.

Wakatsuki, T., M. S. Kolodney, G. I. Zahalak, E. L. Elson, 2000. Cell Mechanics Studied by a Reconstituted Model Tissue. Biophys. J. 79(5), 2353-2368.

Wakatsuki, T., B. Schwab, N. C. Thompson, E. L. Elson, 2001. Effects of cytochalasin D and latrunculin B on mechanical properties of cells. J Cell Sci 114(5), 1025-1036.

Wang, N., J. P. Butler, D. E. Ingber, 1993. Mechanotransduction across the cell surface and through the cytoskeleton. Science 260(5111), 1124-7.

Wang, N., I. M. Tolic-Norrelykke, J. Chen, S. M. Mijailovich, J. P. Butler, J. J. Fredberg, D. Stamenovic, 2002. Cell prestress. I. Stiffness and prestress are closely associated in adherent contractile cells. Am J Physiol Cell Physiol 282(3), C606-16.

Ward, K. A., W. I. Li, S. Zimmer, T. Davis, 1991. Viscoelastic properties of transformed cells: role in tumor cell progression and metastasis formation. Biorheology 28(3-4), 301-13.

Wiggins, P., R. Phillips, 2004. Analytic models for mechanotransduction: Gating a mechanosensitive channel. Proceedings of the National Academy of Sciences of the United States of America 101(12), 4071-4076.

Wilhelm, C., F. Gazeau, J. C. Bacri, 2003. Rotational magnetic endosome microrheology: Viscoelastic architecture inside living cells. Physical Review E 67(6).

Wittmann, T., C. M. Waterman-Storer, 2001. Cell motility: can Rho GTPases and microtubules point the way? J Cell Sci 114(Pt 21), 3795-803.

Worthen, G. S., B. Schwab, E. L. Elson, G. P. Downey, 1989. Mechanics of Stimulated Neutrophils: Cell Stiffening Induces Retention in Capillaries. Science, New Series 245, 183-186.

Wottawah, F., S. Schinkinger, B. Lincoln, R. Ananthakrishnan, M. Romeyke, J. Guck, J. Kas, 2005. Optical rheology of biological cells. Phys Rev Lett 94(9), 098103.

Wu, Z. Z., G. Zhang, M. Long, H. B. Wang, G. B. Song, S. X. Cai, 2000. Comparison of the viscoelastic properties of normal hepatocytes and hepatocellular carcinoma cells under cytoskeletal perturbation. Biorheology 37(4), 279-90.

Yamada, S., D. Wirtz, S. C. Kuo, 2000. Mechanics of living cells measured by laser tracking microrheology. Biophys J 78(4), 1736-47.

Yamauchi, K., M. Yang, P. Jiang, N. Yamamoto, M. Xu, Y. Amoh, K. Tsuji, M. Bouvet, H. Tsuchiya, K. Tomita, A. R. Moossa, R. M. Hoffman, 2005. Real-time in vivo dual-color imaging of intracapillary cancer cell and nucleus deformation and migration. Cancer Res 65(10), 4246-52.

Yanai, M., J. P. Butler, T. Suzuki, H. Sasaki, H. Higuchi, 2004. Regional rheological differences in locomoting neutrophils. Am J Physiol Cell Physiol 287(3), C603-11.

Yeung, A., E. Evans, 1989. Cortical shell-liquid core model for passive flow of liquid-like spherical cells into micropipets. Biophys. J. 56(1), 139-149.

Zahalak, G. I., W. B. McConnaughey, E. L. Elson, 1990. Determination of cellular mechanical properties by cell poking, with an application to leukocytes. J Biomech Eng 112(3), 283-94.

Zaner, K. S., T. P. Stossel, 1982. Some perspectives on the viscosity of actin filaments. J. Cell Biol. 93(3), 987-991.

Zhou, E. H., C. T. Lim, S. T. Quek, 2005a. Finite Element Simulation of the Micropipette Aspiration of a Viscoelastic Cell undergoing Large Deformation. Mechanics of Advanced Materials and Structures 12(6), 501-512.

Zhou, E. H., C. T. Lim, K. S. W. Tan, A. Hassanbhai, C. H. Lim, S. T. Quek, 2005b. Quantitative evaluation of capillary obstruction hypothesis in malaria pathology. Biorheology 42(1-2), 66.

Zhou, E. H., C. T. Lim, K. S. W. Tan, S. T. Quek, 2004a. Finite Element Modeling of the Micropipette Aspiration of Malaria-infected Red Blood Cells. Third International Conference on Experimental Mechanics and Third Conference of the Asian Committee on Experimental Mechanics, Singapore. Proceedings of SPIE Volume: 5852.**:** 763-767.

Zhou, E. H., C. T. Lim, K. S. W. Tan, S. T. Quek, A. Lee, B. Liau, 2004b. Investigating the progression of disease state of malaria-infected red blood cells using micropipette aspiration. Proceedings of the 2nd World Congress for Chinese Biomedical Engineers, Beijing, China.

Zhu, C., G. Bao, N. Wang, 2000. Cell Mechanics: Mechanical Response, Cell Adhesion, and Molecular Deformation. Annual Review of Biomedical Engineering 2(1), 189-226.

Appendix A Reported Mechanical Properties of Cells Based on Three Models

Table A.1. Reported mechanical properties for Newtonian liquid drop model. Values are mean ± standard deviation (SD).

Source	**Experiment**	**T_0 (10^{-3} N/m)**	**μ (Pa·s)**	**T_0/μ (10^{-6} m/s)**	**Cell type**
Evans & Young (1989)	micropipette aspiration	0.035	210±100	N.R.	Granulocytes
Needham & Hochmuth (1990)	micropipette aspiration	N.R.	135±54	N.R.	Neutrophils
Needham & Hochmuth (1992)	tapered pipette aspiration	0.024±0.003	N.R.	N.R.	Neutrophils
Tran-Son-Tay et al. (1991)	recovery/relaxation experiment (after large deformation)	(0.024)*	151.7±39.8	0.17	Neutrophils
Hochmuth et al. (1993)	recovery/relaxation experiment (after small deformation)	(0.024)*	~60	0.33	Neutrophils
Tsai et al. (1993)	micropipette aspiration	0.027	~55 at high shear rate to ~500 at low shear rate	N.R.	Neutrophils
Tran-Son-Tay & Ting-Beall (1994b)	recovery/relaxation experiment (after large deformation)	0.035	N.R.	0.13~0.26	Lymphocytes
Tran-Son-Tay et al. (1994a), Bagge et al. (1977)	tapered pipette aspiration	(0.024)*	140~240	N.R.	Granulocytes
Thoumine et al. (1999)	micropipette aspiration	~0.3	2~4 · 10^4	N.R.	Chick embryo fibroblasts

Table A.2. Reported mechanical properties for homogeneous standard linear solid model. Values are mean ± SD. [+]

Source	**Experiment**	**k_1 (Pa)**	**k_2 (Pa)**	**μ (Pa·s)**	**Cell types**
Schmid-Schonbein et al. (1981)	micropipette aspiration	13.75±5.95	36.85±17.3	6.5±2.7	Neutrophils
Sato et al. (1990)	micropipette aspiration	38±11.5	105±70	4.15±2 · 10^3	Endothelial cells (T[#])
		46±10	95±75	3.6±1.35 · 10^3	Endothelial cells (M[#])
		5.5±1.5	22±20	0.65±0.55 · 10^2	Endothelial cells (CB[#])
		14±2.5	32.5±22	1.15±0.3 · 10^3	Endothelial cells (Colchicine)
Sato et al. (1996)	micropipette aspiration	~22.5	~37.5	~1.7 · 10^3	Endothelial cells
Thoumine and Ott (1997b)	microplate traction	320±130[*]	170±126.6[*]	~4.335 · 10^3[*]	Fibroblasts
Jones et al. (1999a)	micropipette aspiration	125±55	85±45	1.45±0.85 · 10^3	Normal chondrocytes
		175±130	165±195	3.95±6.85 · 10^3	OA[#] chondrocytes
Guilak et al. (2000)	micropipette aspiration	~375	~375	~2.5 · 10^3	Chondrocyte nuclei
Lo and Ferrier (1999)	ECIS[#] with magnetic bead	73.3±33.3[*]	336.7±243[*]	3.3±1.3 · 10^3[*]	Rat osteosarcoma cells
Koay et al. (2003)	cytoindentation	360±180	2300±1480	1.12±0.69 · 10^3	Bovine Chondrocytes

[+] All the parameters reported here are half the values reported in the original works unless otherwise specified (see Eq. (2.14) and the discussion that follows for explanation).

* The parameters reported in the original work are extensional moduli and have been scaled by a factor of 1/3 in order for them to be comparable to those from other works.

[#] ECIS: Electrical cell-substrate impedance sensing; T: trypsin-detached cells; M: mechanically detached cells; CB: cytochalasin B treated cells; OA: chondrocytes isolated from osteoarthritic cartilage.

Table A.3. Reported mechanical properties for power-law rheology (PLR) model. Values are reported as mean ± SD or geometric mean together with geometric SD.

Source	Experiment	α	$A_G = G_0\omega_0^{-\alpha}$ (Pa)	μ (Pa·s)	Cell types
Fabry et al. (2003)	Optical MTC (oscillatory)	0.195	190 †	0.32 †	F9#
		0.302	38 †	0.44	F9 (2μM CD#)
		0.204 ± 0.06	1308 $SD_g = 2.1$ ‡	0.68	HASM#
		0.166	2485 †	0.91	HASM (100μM Hist#)
		0.277	382 †	0.74	HASM (1mM DBcAMP#)
		0.329	159 †	0.40	HASM (2μM CD)
		0.173	1756 †	0.44 †	HBE#
		0.319	231 †	0.37	HBE (2μM CD)
		0.200	1914 †	1.32 †	Macrophages
		0.338	412 †	2.05	Macrophages (2μM CD)
		0.186	753 †	0.43 †	Neutrophils
		0.157	1224 †	0.56	Neutrophils (10nM FMLP)
		0.252	249 †	0.58	Neutrophils (2μM CD)
Puig-De-Morales et al. (2001)	Magnetic MTC (oscillatory)	0.27	160 †	N.R.	BEAS-2B HBE#
Alcaraz et al. (2003)	AFM (oscillatory)	0.22	458	1.68	A549#
		0.20	496	2.69	BEAS-2B HBE#
Yanai et al. (2004)	Optical tweezer (creep)	0.5	7	N.R.	Neutrophils+
		~0.5	~4.3	N.R.	Neutrophils+ (2μM CD)
		~0.5	~2.5	N.R.	Neutrophils+ (10 μM noco#)
Stamenovic et al. (2004)	Optical MTC (oscillatory)	0.158	3822 †	1.76	HASM
		0.121	7309 †	2.55	HASM (10μM Hist)
		0.194	2034 †	1.46	HASM (0.1μM iso#)
		0.208	1592 †	1.55	HASM (10μM iso)
Trepat et al. (2004)	Optical MTC (oscillatory)	0.198	5454 †	19	A549
		0.173	8845 †	19	A549 (12.5% stretch)
Puig-De-Morales et al. (2004)	Optical MTC (oscillatory)	0.181	2788 †	0.5984	HASM
		0.158	5440 †	0.646	HASM (100μM Hist)
		0.238	748 †	0.442	HASM (2μM CD)

Lenormand et al. (2004)	Optical MTC (creep)	0.209	2738 †	N.R.	HASM (control)
		0.180	3697 †	N.R.	HASM (100μM Hist)
		0.219	1479 †	N.R.	HASM (1mM DBcAMP)
		0.223	1101 †	N.R.	HASM (2μM CD)
Laudadio et al. (2005)	Optical MTC (oscillatory)	0.2	309 †	0.26	RASM$^{\#}$
		0.2	341 †	0.30	RASM (control)
		0.27	74 †	0.24	RASM (LA$^{\#}$)
		0.21	176 †	0.26	RASM (CD)
		0.19	366 †	0.28	RASM (Phallacidin)
		0.21	275 †	0.25	RASM (PO$^{\#}$)
		0.2	519 †	0.51	RASM (Jas$^{\#}$)
		0.22	288 †	0.42	RASM (Gen$^{\#}$)
		0.18	595 †	0.48	RASM (5-HT$^{\#}$)
		0.26	114 †	0.34	RASM (DBcAMP)
		0.22	195 †	0.32	RASM (ML-7$^{\#}$)
Smith et al. (2005)	AFM (oscillatory)	0.12±0.02$^{\times}$	743 †±496$^{\times}$	5.1±1.6$^{\times}$	RASM
		0.055±0.017$^{\times}$	2158†±1325$^{\times}$	21±6.6$^{\times}$	RASM (5H-T)
		0.16±0.02$^{\times}$	266 †±119$^{\times}$	7.2±1.3$^{\times}$	RASM (CD)
		0.12±0.01$^{\times}$	805 †±416$^{\times}$	5.1±0.9$^{\times}$	RASM (Wort$^{\#}$)
		0.069±0.004$^{\times}$	1814 †±338$^{\times}$	5.1±0.9$^{\times}$	RASM (Wort + 5-HT)
		0.158±0.02$^{\times}$	322 †±283$^{\times}$	4.1±1.3$^{\times}$	RASM (ML-7)
		0.101±0.01$^{\times}$	733 †±529$^{\times}$	4.4±1.6$^{\times}$	RASM (ML-7 + 5-HT)
Balland et al. (2005)	Optical tweezer (oscillatory)	0.20 ± 0.09$^{\times}$	63.1 $^{\$}$	N.R.	Myoblasts
		0.07 ± 0.08$^{\times}$	16.8 $^{\$}$	N.R.	Myoblasts (75μM blebb$^{\#}$)
Desprat et al. (2005)	Microplates (creep)	0.24 ± 0.08	152.2 $^{\$}$ $SD_g = 2.27$ ‡	N.R.	Myoblasts
Dahl et al. (2005)	Micropipette aspiration (creep)	0.32 ± 0.07	1907 ± 717$^{\&}$	N.R.	Nuclei of TC7 cells
		0.21 ± 0.05	300 ± 87 $^{\&}$	N.R.	TC7 Nuclei (swollen)
	AFM (ramp)	0.20 ± 0.02	933 ± 33 $^{\&}$	N.R.	TC7 Nuclei
This study	Micropipette aspiration (creep)	0.30 ± 0.05	116.6 $SD_g = 1.36$ ‡	N.R.	NIH 3T3$^{\#}$
		0.296 ± 0.03	114.8 $SD_g = 1.50$ ‡	N.R.	NIH 3T3 (0.1% DMSO)
		0.26 ± 0.05	55.9 $SD_g = 1.27$ ‡	N.R.	NIH 3T3 (2μM CD)
		0.23 ± 0.10	144.3 $SD_g = 2.01$ ‡	N.R.	NIH 3T3 (100μM col$^{\#}$)
		0.175 ± 0.13	186.2 $SD_g = 2.18$ ‡	N.R.	NIH 3T3 (1mM col)

[†] These parameters were originally reported as apparent moduli, namely specific torque divided by bead rotation or bead translation. Assuming that the elastic finite element solution (Mijailovich et al. 2002) is also valid for other adherent cells besides human airway smooth muscle cells and using embedding that is equivalent to 10% of bead diameter, the complex moduli can be derived using Eq. (2.19).

[#] Abbreviations: F9 − mouse embryonic carcinoma cells (F9); HASM − human airway smooth muscle cells; RASM − rat airway smooth muscle cells; HBE − human bronchial epithelial cells; BEAS-2B HBE − Human bronchial (BEAS-2B) epithelial cells; A549 − Human alveolar (A549) epithelial cells; NIH 3T3 − NIH 3T3 fibroblasts. Hist − histamine; FMLP − N-formyl-methionyl-leucylphenylalanine; DBcAMP − N^6,2′-O-dibutyryladenosine 3′,5′-cyclic monophosphate; CD − cytochalasin D; col − colchicine; noco − nocodazole; iso − isoproterenol; blebb − blebbistatin; PO − phalloidin oleate; jas − jasplakinolide; gen − genistein; ML7 − 1-(5-iodonaphthalene-1-sulfonyl)-1H-hexahydro-1,4-diazepine; 5-HT − serotonin.

[‡] SD_g is the geometric standard deviation.

[$] These parameters were originally reported as extensional storage moduli at 1Hz. They are first scaled by a factor of 1/3 to convert to shear moduli, G'(1 Hz). Then A_G is computed as $A_G = G'(1\ \mathrm{Hz}) \Big/ \left[(2\pi)^\alpha \cos(\pi\alpha/2)\right]$ (note $G'(\omega) = A_G \omega^\alpha \cos(\pi\alpha/2)$, cf. Eq. (B.12)).

[&] These parameters were originally reported as extensional storage moduli. They are scaled by a factor of 1/3 to convert to shear moduli.

[×] The standard deviation was calculated by multiplying the standard error with the square root of cell number.

[+] Probed by trapping and moving intracellular organelles.

Appendix B Linear Viscoelasticity

B.1 Linear viscoelasticity based on fractional derivatives

The differential equation for classical linear viscoelasticity usually contains time derivatives of integer order (Flugge 1967)

$$\tau_{ij}(t)+\sum_{k=1}^{n}b_k\frac{d^k\tau_{ij}(t)}{dt^k}=a_0\gamma_{ij}(t)+\sum_{k=1}^{m}a_k\frac{d^k\gamma_{ij}(t)}{dt^k} \tag{B.1}$$

where a_0, a_k and b_k (k = 1, 2, …, n) are material parameters, and $\tau_{\mathrm{ij}}(t)$ and $\gamma_{\mathrm{ij}}(t)$ are time dependent stress and strain components. However, the classical model was often found inadequate for describing the mechanical behavior of real materials (Pritz 1996). A more general model was then proposed based on fractional derivative, which can be expressed as (Pritz 1996)

$$\tau_{ij}(t)+\sum_{k=1}^{n}b_kD^{\beta_k}\left[\tau_{ij}(t)\right]=a_0\gamma_{ij}(t)+\sum_{k=1}^{m}a_kD^{\alpha_k}\left[\gamma_{ij}(t)\right] \tag{B.2}$$

where a_0, a_k, b_k, α_k and β_k are material parameters (α_k and β_k must be nonnegative real numbers), m and n are nonnegative integers ($m = n$ or $m = n + 1$, due to thermodynamic constraints) and $D^{\alpha}[\cdot]$ is the αth order fractional differentiation operator defined as follows

$$D^{\alpha}\left[f(t)\right]=\frac{1}{\Gamma(1-\alpha)}\frac{d}{dt}\int_0^t\frac{f(s)}{(t-s)^{\alpha}}ds. \tag{B.3}$$

When α_k and β_k assume positive fractions ($0 \le \alpha_k \le 1$ and $0 \le \beta_k \le 1$), Eq. (B.2) represents the fractional derivative models (Pritz 1996). On the other hand, when α_k and β_k are non-negative integers, $D^{\alpha}[\cdot]$ reduces to the conventional integer derivative and Eq. (B.2) reduces to the linear differential equation for spring-dashpot models. It is noted that all the viscoelastic models presented in Chapter 2, with the exception of the shear thinning liquid drop model, can be derived from Eq. (B.2) through certain simplifying assumptions.

B.2 Derivation of the complex modulus

Through Fourier transform, Eq. (B.2) can be transformed into the frequency domain (Findley et al. 1976), which leads to

$$F\left[\tau_{ij}\left(t\right)\right]=G^{*}F\left[\gamma_{ij}\left(t\right)\right] \tag{B.4}$$

where G^{*} is the complex modulus given by (Pritz 1996)

$$G^{*}\left(\omega\right)=G'+iG''=\frac{a_0+\sum_{k=1}^{m}a_k\left(i\omega\right)^{\alpha_k}}{1+\sum_{k=1}^{n}b_k\left(i\omega\right)^{\beta_k}} \tag{B.5}$$

with G' being the storage modulus and G'' the loss modulus.

In order to examine the applicability of the spring-dashpot models in the frequency domain, the complex modulus of the SLS-D model can be derived. The differential equation for SLS-D model is

$$\boldsymbol{\tau}+\left[\frac{\mu_0}{k_1}+\frac{\mu\left(k_1+k_2\right)}{k_1k_2}\right]\dot{\boldsymbol{\tau}}+\frac{\mu_0\mu}{k_1k_2}\ddot{\boldsymbol{\tau}}=\mu_0\dot{\boldsymbol{\gamma}}+\frac{\mu_0\mu\left(k_1+k_2\right)}{k_1k_2}\ddot{\boldsymbol{\gamma}}\,. \tag{B.6}$$

Thus the complex modulus for SLS-D model can be derived from Eqs. (B.5) and (B.6) as

$$\begin{aligned}G^{*}=&\frac{\mu_0^2\omega^2\left[k_1k_2^2+\mu^2\omega^2\left(k_1+k_2\right)\right]}{\mu_0^2\omega^2\left(k_2^2+\mu^2\omega^2\right)+k_1^2k_2^2+\mu^2\omega^2\left(k_1^2+k_2^2\right)+2\mu k_2\omega^2\left(\mu_0k_2+\mu k_1\right)}\\&+i\frac{\mu_0\omega\left[k_1^2k_2^2+\mu^2\omega^2\left(k_1+k_2\right)^2+\mu_0\mu k_2^2\omega^2\right]}{\mu_0^2\omega^2\left(k_2^2+\mu^2\omega^2\right)+k_1^2k_2^2+\mu^2\omega^2\left(k_1^2+k_2^2\right)+2\mu k_2\omega^2\left(\mu_0k_2+\mu k_1\right)}\end{aligned} \tag{B.7}$$

which was plotted in Fig. 2.11 in an attempt to fit the oscillatory MTC data. Similarly, the complex modulus for SLS model can be derived from Eqs. (B.5) and (2.14) as

$$G^* = \frac{k_1 k_2^2 + \mu^2 \omega^2 \left(k_1 + k_2\right)}{k_2^2 + \mu^2 \omega^2} + i \frac{\mu k_2^2 \omega}{k_2^2 + \mu^2 \omega^2} \tag{B.8}$$

B.3 Derivation of power-law rheology model from the fractional derivative viscoelasticity

For deriving the PLR model, Djordjevic et al. (2003) introduces the assumptions that $n = 1$, $m = 2$, $b_1 = 0$, $\beta_1 = 0$, $\alpha_2 = 1$, leaving open four material parameters a_0, a_1, $a_2$and α_1.

$$\tau_{ij} = a_0 \gamma_{ij} + a_1 D^{\alpha_1}\left[\gamma_{ij}\right] + a_2 D^1 \left[\gamma_{ij}\right] \tag{B.9}$$

Fitting this model to the experimental data reported by Fabry et al. (2001a), it was found that $a_0 = 0$. Further, if one denotes α_1 as α, a_2 as μ and a_1 as G_0 / ω_0^α, substituting into Eq. (B.5) results in the following complex modulus

$$G^*\left(\omega\right) = G' + iG'' = G_0 \left(\frac{i\omega}{\omega_0}\right)^\alpha + i\omega\mu \tag{B.10}$$

where α is the exponent of the power law ($0 \leq \alpha \leq 1$) (note that $i^\alpha = \cos\frac{\pi\alpha}{2} + i \sin\frac{\pi\alpha}{2}$), μ is the Newtonian viscous term, ω is the angular frequency and G_0 and ω_0 are scaling factors for stiffness and frequency, respectively (note that $G' = G_0 \cos\left(\pi\alpha / 2\right) \approx G_0$ when $\omega = \omega_0$ and $\alpha \to 0$). This formula is slightly different from that originally proposed by Fabry et al. (2001a).

$$G^*(\omega) = G_0\left(\frac{i\omega}{\omega_0}\right)^{\alpha}\Gamma(1-\alpha) + i\omega\mu \tag{B.11}$$

by a factor of $\Gamma(1-\alpha)$. In the limit of α approaching 0, the structural damping coefficient η will approach 0 and the loss tangent G''/G' will reach the minimum (for the same ω) for both formulae, corresponding to a predominantly elastic solid behavior. Because $\Gamma(1-\alpha)$ is approximately unity when α is small (e.g. less than 0.3), the two formulae are essentially the same for small α. On the other extreme where α approaches 1, both η and the loss tangent will approaches infinity, indicating that the material will behave like Newtonian viscous fluid. In this case, Eq. (B.10) will predict a finite loss modulus of $G'' = G_0/\omega_0 + \omega\mu$. In contrast Eq. (B.11) will predict an infinite loss modulus, which is unlikely to happen in real situation. Therefore, although both formulae can capture the essential feature of the dynamic material behavior of cells and fit the experimental data, Eq. (B.10) is preferred.

B.4 Power-law rheology model and the correlation between complex modulus, creep function and relaxation modulus

Unless at extremely short time or high frequency, the Newtonian term $i\omega\mu$ in the PLR model can often be neglected without affecting the accuracy of other parameters (Lenormand et al. 2004). In addition, this term usually could hardly be quantified with creep experiments (Lenormand et al. 2004; Yanai et al. 2004; Dahl et al. 2005; Desprat et al. 2005). Therefore, a simplified PLR model has been widely used as

$$G^*(\omega) = G_0\left(\frac{i\omega}{\omega_0}\right)^{\alpha} = A_G(i\omega)^{\alpha} = A_G\omega^{\alpha}\left(\cos\frac{\pi\alpha}{2} + i\sin\frac{\pi\alpha}{2}\right) \tag{B.12}$$

where ω is in rad/s (cf. Eq. (2.22)).

In the time domain, the relaxation modulus of the power-law rheology model (Eq. (B.10)) can be obtained by substituting the unit step strain function $\gamma(\mathrm{t}) = H(t)$ into Eq. (B.9) as follows

$$G(t) = \frac{G_0}{\Gamma(1-\alpha)}(\omega_0 t)^{-\alpha} H(t) + \mu\delta(t) \tag{B.13}$$

where $\delta(\cdot)$ is the Dirac delta function. Neglecting the Newtonian term $\mu\delta(\mathrm{t})$ and introducing $t_0 = 1/\omega_0$ results in

$$G(t) = \frac{G_0}{\Gamma(1-\alpha)}\left(\frac{t}{t_0}\right)^{-\alpha} H(t) = \frac{A_G}{\Gamma(1-\alpha)} t^{-\alpha} H(t). \tag{B.14}$$

where t is in seconds (cf. Eq. (2.24)).

The creep compliance $J(t)$ is related to the relaxation modulus through (Ferry 1980)

$$\int_0^t G(t) J(t-\tau)\, d\tau = t \tag{B.15}$$

from which it can be derived that

$$J(t) = \mathrm{L}^{-1}\left[\frac{1}{s^2\,\mathrm{L}\left[G(t)\right]}\right] \tag{B.16}$$

where L[·] and L^{-1}[·] represent the Laplace transform and inverse Laplace transform respectively. Thus, the creep compliance of the power-law rheology model can be reached as

$$J(t) = A_J t^{\alpha} = \frac{1}{A_G \Gamma(1+\alpha)} t^{\alpha} \tag{B.17}$$

where A_J is the compliance constant, related to A_G through

$$A_G = \frac{1}{A_J \Gamma(1+\alpha)}. \tag{B.18}$$

The theoretical framework of the power-law rheology is summarized in Fig. B.1.

$$\begin{tikzcd}
 & G^*\left(\omega\right)=A_G\left(i\omega\right)^\alpha \arrow[ddl, leftrightarrow] \arrow[ddr, leftrightarrow] & \\
 & \tau_{ij}=A_G D^\alpha\left[\gamma_{ij}\right] & \\
J\left(t\right)=\dfrac{1}{A_G\Gamma\left(1+\alpha\right)}t^\alpha \arrow[rr, leftrightarrow] & & G\left(t\right)=\dfrac{A_G}{\Gamma\left(1-\alpha\right)}t^{-\alpha}
\end{tikzcd}$$

Fig. B.1. The correlation between complex modulus, creep function and relaxation modulus for the power-law rheology model. Knowing one of the three will allow prediction of the other two.

B.5 Elastic-viscoelastic correspondence principle

For the solution of an initial-boundary-value problem which involves linear viscoelastic deformation, the governing equations (including stress-strain relations, strain-deformation relations, conservation of momentum, and boundary conditions) can be transformed into the Laplace domain (Flugge 1967). The resulting equations will have the same form as the corresponding elastic problem. Therefore, if the elastic solution is known, the corresponding viscoelastic solution in the Laplace domain can be derived by replacing the elastic constants and the load with their Laplace-transform counterparts, i.e. G by $s\bar{G}\left(s\right)$ and P by $\bar{P}\left(s\right)$, respectively. The time domain solution can be derived by inverse Laplace transform.

For example, the elastic half-space solution to micropipette aspiration (Theret et al. 1988) is

$$\frac{L_p}{R_P}=\frac{\Phi_P\Delta P}{2\pi G} \tag{B.19}$$

Now one wants to solve the creep deformation of a viscoelastic half-space model. The relaxation modulus is $G(t)$ and the suction pressure is $P(t) = \Delta P\ H(t)$. The corresponding solution in the Laplace domain will be

$$\frac{\bar{L}_p(s)}{R_P} = \frac{\Phi_P}{2\pi}\frac{\bar{P}(s)}{s\bar{G}(s)} \tag{B.20}$$

where the superposed bars indicate Laplace transform. However, because $\bar{P}(s) = \Delta P/s$ and $\bar{J}(s)\bar{G}(s) = s^{-2}$ (Flugge 1967), it can be derived that

$$\frac{\bar{L}_p(s)}{R_P} = \frac{\Phi_P \Delta P}{2\pi}\bar{J}(s) \tag{B.21}$$

Thus, the viscoelastic solution in time domain can be reached by inverse Laplace transform as

$$\frac{L_p(t)}{R_P} = \frac{\Phi_P \Delta P}{2\pi}J(t). \tag{B.22}$$

B.6 Derivation of ramp-test response in micropipette aspiration from power-law creep function

In the ramp tests, the apparent deformability S/R_p was measured at two loading rates by applying linear curve fitting to the pressure-deformation relationship (cf. Chapter 4). In the creep tests, the power-law creep function (Eq. (5.2)) was found to accurately account for the creep deformation of cells (cf. Chapter 5). In order to evaluate the consistency between the creep-test results and the ramp-test results, the rate-dependent apparent deformability can be derived from the creep function measured with creep tests and compared with the experimental results of ramp tests.

Based on the half-space model, the representative stress and strain in micropipette aspiration can be defined as

$$\begin{aligned} \underset{\sim}{\varepsilon} &= L_p / R_p \\ \underset{\sim}{\sigma} &= \Phi_P \Delta P / (2\pi) \end{aligned} . \tag{B.23}$$

Thus, the creep deformation in micropipette aspiration (Eq. (5.1)) can be expressed by $\underset{\sim}{\varepsilon}(t) = \underset{\sim}{\sigma} J(t)$. Using the Boltzmann superposition principle, the evolution of the representative strain in response to certain loading history can be written as

$$\underset{\sim}{\varepsilon}(t) = \int_{-\infty}^{t} J(t - t') \dot{\underset{\sim}{\sigma}}(t') dt' \tag{B.24}$$

In a ramp test, the loading history is

$$\Delta P(t) = v_{\Delta P} t, \ t \geq 0 \tag{B.25}$$

where $v_{\Delta P}$ is the increasing rate of the pressure. Substitution of Eqs. (5.2), (B.23) and (B.25) into Eq. (B.24) results in

$$\frac{L_p(t)}{R_p} = \frac{\Phi_P v_{\Delta P}}{2\pi(1+\alpha)} A_J t^{1+\alpha} = \frac{\Phi_P \Delta P(t)}{2\pi(1+\alpha)} A_J t^{\alpha}, \ t \geq 0 \tag{B.26}$$

which will be used to predict the apparent deformability from the measured creep function of cells (Section 5.3.2).

B.7 Power-law dependence of apparent deformability on loading rate in ramp tests

In both ramp experiments and the corresponding finite element simulation, the pressure increases from $\Delta P(0) = 0$ to $\Delta P(t) = \Delta P_0$ at a certain loading rate $v_{\Delta P}$. The apparent deformability (C) in a ramp test is defined as the average slope of

$L_p(t)/R_p$ versus $\Delta P(t)/G$ (cf. Eq. (6.17)). In practice, C is generally computed from discrete data points as

$$C = \frac{\sum_{i=1}^{n}\left(x_i - \bar{x}\right)\left(y_i - \bar{y}\right)}{\sum_{i=1}^{n}\left(x_i - \bar{x}\right)^2} \tag{B.27}$$

where $x_i = \Delta P(t_i)/G$ and $y_i = L_p(t_i)/R_p$ ($i = 1, 2, \ldots, n$); $\bar{x}$ and $\bar{y}$ are the means of x_i and y_i, respectively. $\Delta P_i = \Delta P(t_i)$ is the pressure value of the ith data point which corresponds to time, $t_i = \Delta P_i / v_{\Delta P}$ (cf. Eq. (B.25)). In order to study the effect of loading rate on apparent deformability, ΔP_0 and ΔP_i are usually kept constant, and material properties (A_J, G and α) and pipette geometry are also fixed. Thus, x_i and $\bar{x}$ will be constant. On the other hand, y_i can be derived from Eq. (B.26) as

$$y_i = \frac{L_p(t_i)}{R_p} = \left[\frac{\Phi_P \Delta P_i}{2\pi(1+\alpha)} A_J\right] t_i^{\alpha} = \left[\frac{\Phi_P \left(\Delta P_i\right)^{1+\alpha}}{2\pi(1+\alpha)} A_J\right] v_{\Delta P}{}^{-\alpha} \tag{B.28}$$

which is proportional to $v_{\Delta P}{}^{-\alpha}$. Subsequently, $\bar{y}$ is also proportional to $v_{\Delta P}{}^{-\alpha}$. Therefore, in view of Eq. (B.27), we have

$$C \propto v_{\Delta P}{}^{-\alpha}. \tag{B.29}$$

which implies that the power-law exponent α can also be measured with ramp tests using different loading rates, as shown by Dahl *et al.* (2005).

Appendix C Prony Series Approximation of Power-law Rheology

Table C.1. Prony-series coefficients for fitting power-law rheology model: $G(t) = 100t^{-\alpha}$ Pa .

α	0	0.1	0.2	0.3	0.4	0.5	0.387
$G(0)$ (Pa)	100	213	450	944	1970	4100	1790
λ_1 (10^{-3} s)	–	3.34	3.13	2.93	2.74	2.56	2.77
λ_2 (10^{-2} s)	–	5.61	5.25	4.91	4.60	4.31	4.64
λ_3 (10^{-1} s)	–	9.09	8.43	7.84	7.29	6.78	7.36
λ_4 (10 s)	–	1.54	1.43	1.34	1.25	1.18	1.26
λ_5 (10^{2} s)	–	2.87	2.58	2.34	2.14	1.97	2.17
g_1	–	0.245	0.429	0.567	0.671	0.750	0.659
g_2	–	0.185	0.245	0.246	0.222	0.188	0.226
g_3	–	0.139	0.140	0.106	0.0722	0.0463	0.0762
g_4	–	0.106	0.0801	0.0459	0.0235	0.0114	0.0258
g_5	–	0.0926	0.0513	0.0216	0.00825	0.00297	0.00938

Appendix D Curriculum Vitae

ZHOU Enhua

PhD Candidate in Department of Civil Engineering and
Nano Biomechanics Lab, Department of Bioengineering
National University of Singapore, 1 Engineering Drive 2, Singapore 117576
Email: g0202123@nus.edu.sg

Education

2002~2006	PhD candidate, National University of Singapore, Singapore. Thesis title: Experimental and numerical studies on the viscoelastic behavior of living cells. Advisors: Dr. QUEK Ser Tong and Dr. LIM Chwee Teck.
1999~2002	M.Eng., Wuhan University, P.R. China. Majored in Engineering Mechanics.
1995~1999	B.Eng., Wuhan University of Hydraulic and Electric Engineering (WUHEE), P.R. China. Majored in Hydroelectric Structural Engineering.

Major Research Interests

Cell mechanics, including

- rheological properties of fibroblasts,
- mechanics of malaria-infected red blood cells, and
- soft glassy rheology of cytoskeleton.

Academic Honors

2002~2006	NUS Research Scholarship
1999	Honorable Mention in Mathematical Contest in Modeling (USA)
1998	WUHEE Paragon of Excellent Student Leader Scholarship
1998	Chen Maozhong Foundation Scholarship
1997	Chinese Hydraulic Engineering Society Excellent Student scholarship
1996~1998	WUHEE First-Class Academic Scholarship

English Proficiency

12/2000	GRE General Test: 2260 (V 690 Q 800 A 770)
05/2001	TOEFL: 627 TWE: 4.0

Teaching Experience

Graduate teaching assistant in the Department of Civil Engineering, NUS

Semester I, 2003/2004	Linear Finite Element Analysis
Semester II, 2003/2004	Linear Finite Element Analysis
Semester II, 2003/2004	Structural Stability & Dynamics
Semester I, 2004/2005	Linear Finite Element Analysis

Publications

Peer-reviewed journal articles

1. **Zhou, E.H.**, C.T. Lim, and S.T. Quek, Micropipette aspiration of fibroblasts - creep tests and power-law behavior. (In Preparation), 2006.
2. **Zhou, E.H.**, C.T. Lim, and S.T. Quek, Micropipette aspiration of fibroblasts - ramp tests and effects of pipette size. (In Preparation), 2006.
3. **Zhou, E.H.**, C.T. Lim, and S.T. Quek, Finite element simulation of micropipette aspiration based on power-law rheology. (In Preparation), 2006.
4. Lim, C.T., **E.H. Zhou**, and S.T. Quek, Mechanical models for living cells - a review. Journal of Biomechanics. vol. 39: pp. 195-216, 2006.
5. Lim, C.T., **E.H. Zhou**, A. Li, S.R.K. Vedula, and H.X. Fu, Experimental techniques for single cell and single molecule biomechanics. Materials Science and Engineering: C. vol. 26 (8): pp. 1278-1288, 2006.
6. **Zhou, E.H.**, C.T. Lim, and S.T. Quek, Finite element simulation of the micropipette aspiration of a living cell undergoing large viscoelastic deformation. Mechanics of Advanced Materials and Structures. vol. 12 (6): pp. 501-512, 2005.
7. **Zhou, E.H.**, Y.W. Zhu, and T. Wang, Transitional-zone method in hexahedral finite element meshing in geotechnical engineering. Wuhan University Journal (Engineering Edition). vol. 35 (3): pp. 24-29, 2002.
8. Wang, T., **E.H. Zhou**, H.C. Zhu, H.B. Zhao, Q.Q. Ke, and Y. Wang, Deformation analysis of middle pier in Three Gorges permanent shiplock. Rock and Soil Mechanics. vol. 23 (06): pp. 683-686, 2002.

International conference papers

1. **Zhou, E.H.**, C.T. Lim, S.M. Ng, and S.T. Quek. Viscoelastic finite element analysis of micropipette aspiration with application to fibroblasts. in Proceedings of the 3rd International Conference on Materials for Advanced Technologies. Singapore.2005.
2. **Zhou, E.H.**, C.T. Lim, K.S.W. Tan, A. Hassanbhai, C.H. Lim, and S.T. Quek, Quantitative evaluation of capillary obstruction hypothesis in malaria pathology. Biorheology. vol. 42 (1-2): pp. 66, 2005.

3. Hassanbhai, A., **E.H. Zhou**, C.T. Lim, S. Suresh, and K.S.W. Tan. The Effect of Pentoxifylline on the Deformability of Normal and Malaria-Infected Red Blood Cells. in Keystone Symposia: Drugs Against Protozoan Parasites: Target Selection, Structural Biology and Medicinal Chemistry (X6). Copper Mountain, Colorado.2005.
4. **Zhou, E.H.**, C.T. Lim, K.S.W. Tan, and S.T. Quek. Finite Element Modeling of the Micropipette Aspiration of Malaria-infected Red Blood Cells. in Third International Conference on Experimental Mechanics and Third Conference of the Asian Committee on Experimental Mechanics. Singapore.2004.
5. **Zhou, E.H.**, C.T. Lim, K.S.W. Tan, S.T. Quek, A. Lee, and B. Liau. Investigating the progression of disease state of malaria-infected red blood cells using micropipette aspiration. in Proceedings of the 2nd World Congress for Chinese Biomedical Engineers. Beijing, China.2004.